

# RESONANCE PHENOMENA IN A SCALAR DELAY DIFFERENTIAL EQUATION WITH TWO STATE-DEPENDENT DELAYS

R.C. CALLEJA\*, A.R. HUMPHRIES†, AND B. KRAUSKOPF‡

March 8, 2022

**Abstract.** We study a scalar DDE with two delayed feedback terms that depend linearly on the state. The associated constant-delay DDE, obtained by freezing the state dependence, is linear and without recurrent dynamics. With state dependent delay terms, on the other hand, the DDE shows very complicated dynamics. To investigate this, we perform a bifurcation analysis of the system and present its bifurcation diagram in the plane of the two feedback strengths. It is organized by Hopf-Hopf bifurcation points that give rise to curves of torus bifurcation and associated two-frequency dynamics in the form of invariant tori and resonance tongues. We numerically determine the type of the Hopf-Hopf bifurcation points by computing the normal form on the center manifold; this requires the expansion of the functional defining the state-dependent DDE in a power series whose terms up to order three only contain constant delays. We implemented this expansion and the computation of the normal form coefficients in Matlab using symbolic differentiation, and the resulting code `HHnfDDE` is supplied as a supplement to this article. Numerical continuation of the torus bifurcation curves confirms the correctness of our normal form calculations. Moreover, it enables us to compute the curves of torus bifurcations more globally, and to find associated curves of saddle-node bifurcations of periodic orbits that bound the resonance tongues. The tori themselves are computed and visualized in a three-dimensional projection, as well as the planar trace of a suitable Poincaré section. In particular, we compute periodic orbits on locked tori and their associated unstable manifolds (when there is a single unstable Floquet multiplier). This allows us to study transitions through resonance tongues and the breakup of a 1:4 locked torus. The work presented here demonstrates that state dependence alone is capable of generating a wealth of dynamical phenomena.

**Key words.** State-dependent delay differential equations, bifurcation analysis, invariant tori, resonance tongues, Hopf-Hopf bifurcation, normal form computation

**AMS subject classifications.** 34K60, 34K18, 37G05, 37M20

**1. Introduction.** Time delays arise naturally in numerous areas of application as an unavoidable phenomenon, for example, in balancing and control [8, 19, 35, 39, 64, 65, 66, 67], machining [36], laser physics [40, 46, 54], agent dynamics [52, 53, 70, 73], neuroscience and biology [1, 18, 20, 42, 79], and climate modelling [13, 41, 48]. Important sources of delays are communication times between components of a system, maturation and reaction times, and the processing time of information received. When they are sufficiently large compared to the relevant internal time scales of the system under consideration, then the delays must be incorporated into its mathematical description. This leads to mathematical models in the form of delay differential equations (DDEs). In many situations the relevant delays can be considered to be fixed; examples are the travel time of light between components of a laser system and machining with rotating tools.

There is a well established theory of DDEs with a finite number of constant delays as infinite dimensional dynamical systems; see, for example, [6, 26, 27, 12, 74, 75]. Usually the phase space of the dynamical system is taken to be  $C = C([- \tau, 0], \mathbb{R}^d)$ , the Banach space of continuous functions mapping  $[- \tau, 0]$  to  $\mathbb{R}^d$ , where  $d$  is the number of variables and  $\tau$  is the largest of the delays. The DDE can then be written as a retarded functional differential equation

$$u'(t) = F(u_t), \quad (1.1)$$

\*Depto. Matemáticas y Mecánica, IIMAS, Universidad Nacional Autónoma de México, 01000 México. (calleja@mym.iimas.unam.mx)

†Departments of Mathematics & Statistics, and, Physiology, McGill University, Montreal, Quebec H3A 0B9, Canada (Tony.Humphries@mcgill.ca)

‡Department of Mathematics, University of Auckland, Auckland 1142, New Zealand (b.krauskopf@auckland.ac.nz)

where  $F : C \rightarrow \mathbb{R}^d$  and  $u_t \in C$  for each  $t \geq 0$  is the function

$$u_t(\theta) = u(t + \theta), \quad \theta \in [-\tau, 0]. \quad (1.2)$$

In other words, an initial condition consists of a function over the time interval from the (maximal) delay  $\tau$  ago up to time 0, which (under appropriate mild assumptions) determines the solution for all time  $t > 0$ . In fact, solutions of constant-delay DDEs depend smoothly on their initial conditions, and linearizations at equilibria and periodic solutions have at most finitely many unstable eigen-directions. As a consequence, bifurcation theory for this class of DDEs is analogous to that for ordinary differential equations (ODEs), and one finds the same types of bifurcations. In particular, center manifold and normal form methods allow for the local reduction of the DDE to an ODE describing the dynamics near a bifurcation point of interest. Moreover, advanced numerical tools for simulation and bifurcation analysis of DDEs with constant delays have become available in recent years [4, 5, 7, 17, 47, 72, 77]. These theoretical and numerical tools have been applied very successfully in many application areas, including those mentioned above.

It is very important to realise that treating the delays that arise as constant is a modelling assumption that must be justified. This can be argued successfully, for example, in machining when the tool has nearly infinite stiffness perpendicular to the cutting direction [75], or in laser dynamics where light travels over a fixed distance [40]. On the other hand, in many contexts, including in biological systems and in control problems [9, 10, 11, 21, 36, 38, 68, 82], the delays one encounters are not actually constant. In particular, they may depend on the state in a significant way, that is, change dynamically during the time-evolution of the system.

DDEs with state-dependent delays have been an active area of research in recent years. Many parts of the general theory of DDEs with constant delays have been extended to also cover state-dependent DDEs, where  $\tau$  is now a global bound on the maximal possible delay; see [29] and the discussion in [34]. However, the mathematical theory is considerably more complicated and as yet incomplete. Solutions of state-dependent DDEs do not depend smoothly on initial conditions or parameters unless extra assumptions are made on the initial conditions [28], and this dramatically complicates arguments around key concepts, requiring new theory and proofs for asymptotics, the initial value problem, bifurcations, and invariant manifolds. Indeed, these important elements of the theory have been addressed only recently [29, 32, 49, 59, 60, 71, 80, 81]. Similarly, the numerical bifurcation analysis of state-dependent DDEs is more involved. Recent developments include approaches for the continuation of solutions and bifurcations for state dependent delay equations [34, 72]. The paper [47] has methods for finding invariant manifolds for DDEs with constant delays. Issues that remain outstanding include smoothness of center manifolds and, therefore, also normal form reductions.

In light of the considerable additional difficulty, state-dependent delays are quite often replaced by constant delays — by considering some sort of average or nominal delays — even in modelling situations when this cannot be readily justified. The obvious question is whether and when a state-dependent DDE displays dynamics that is considerably different from that of the associated constant-delay DDE.

In this paper we address this practical question by studying a prototypical DDE with state-dependent delays, rather than an equation arising from a specific application. This example DDE has the important property that it exhibits very complicated dynamics with state dependence, while it reduces to a linear DDE with only trivial dynamics if the delays are made constant. Specifically, we consider here the scalar DDE

$$u'(t) = -\gamma u(t) - \kappa_1 u(\alpha_1(t, u(t))) - \kappa_2 u(\alpha_2(t, u(t))), \quad \text{where } \alpha_i(t, u(t)) = t - a_i - c_i u(t). \quad (1.3)$$

The two delay terms, with feedback strengths  $\kappa_1, \kappa_2 \geq 0$ , are given by the linear functions  $\alpha_i(t, u(t))$ , where  $a_i$  and  $c_i$  are strictly positive. In the absence of the delay terms, that is, for  $\kappa_1 = \kappa_2 = 0$ ,

(1.3) is a linear scalar equation whose solutions decay exponentially to the origin with rate  $\gamma > 0$ . For  $\kappa_1, \kappa_2 \neq 0$ , on the other hand, the delay terms are present and constitute a feedback. When  $c_1 = c_2 = 0$  the DDE (1.3) is linear with two fixed delays  $a_1$  and  $a_2$ , while for  $c_1, c_2 \neq 0$  the delay terms are linearly state dependent.

A singularly perturbed version of (1.3) is studied in [33, 43, 61]. In [43] solutions are considered near the singular Hopf bifurcations, while [33] constructs large amplitude singular solutions and studies the singular limit of the fold bifurcations. Equation (1.3) is a generalisation of the corresponding single delay DDE which can be obtained from (1.3) by setting  $\kappa_2 = 0$ . The single delay DDE was first introduced in a singularly perturbed form as an example problem by Mallet-Paret and Nussbaum in [60] and considered extensively in [62] as part of a series of papers [56, 57, 58, 60, 61, 62] studying singularly perturbed solutions of state-dependent DDEs.

We consider (1.3) with all parameters non-negative and without loss of generality assume that  $a_2 > a_1$ . We also assume

$$\gamma > \kappa_2. \quad (1.4)$$

It is shown in [34] that if (1.4) holds and

$$\phi(t) \in \left(-\frac{a_1}{c}, \frac{a_1}{\gamma c}(\kappa_1 + \kappa_2)\right), \quad \forall t \in \left[-a_2 - \frac{a_1}{\gamma}(\kappa_1 + \kappa_2), 0\right] \quad (1.5)$$

then equation (1.3) is well posed and all solutions of the initial value problem composed of solving (1.3) for  $t \geq 0$  with the initial function

$$u(t) = \phi(t), \quad t \leq 0 \quad (1.6)$$

satisfy

$$u(t) \in \left(-\frac{a_1}{c}, \frac{a_1}{\gamma c}(\kappa_1 + \kappa_2)\right), \quad \forall t > 0. \quad (1.7)$$

This bound on the solution also implies a bound on the delays with (1.3) and (1.7) implying that

$$\alpha_i(t, u(t)) \in \left(t - a_i - \frac{a_1}{\gamma}(\kappa_1 + \kappa_2), t\right) \subset \left(t - a_2 - \frac{a_1}{\gamma}(\kappa_1 + \kappa_2), t\right), \quad \forall t \geq 0 \quad (1.8)$$

and, in particular, the state-dependent delays can never become advanced when  $\gamma > \kappa_2$ . It is also shown in [34] that there exists  $\xi \in [0, a_2 + \frac{a_1}{\gamma}(\kappa_1 + \kappa_2)]$  such that  $\alpha_i(t, u(t))$  is a strictly monotonic increasing function of  $t$  for  $t > \xi$ .

Notice that the DDE (1.3) is of the form (1.1) with  $d = 1$  if we let

$$F(\phi) = -\gamma\phi(0) - \kappa_1\phi(-a_1 - c\phi(0)) - \kappa_2\phi(-a_2 - c\phi(0)). \quad (1.9)$$

We take  $\tau = a_2 + \frac{a_1}{\gamma}(\kappa_1 + \kappa_2)$ , which by (1.8) ensures that  $\alpha_i(t, u(t)) \in [t - \tau, t]$  for  $t \geq 0$  and the function  $u_t$  includes all the information necessary to evaluate  $u'(t)$ . Moreover, provided the initial function  $\phi$  is Lipschitz it follows from standard DDE theory [14] that the initial value problem has a unique solution satisfying (1.7).

For  $c_1 = c_2 = 0$  general theory [6, 26, 27] states that, depending on the values of  $\gamma$ ,  $\kappa_1$  and  $\kappa_2$ , all trajectories of (1.3) decay to the origin or grow exponentially in time. In other words, the dynamics of the system without state dependence in the delay terms is indeed trivial. On the other hand, it was shown in [34] that state dependence of the delay terms changes the dynamics completely, since the function  $F$  in (1.9) is nonlinear. Therefore, the state dependency of the delays for  $c_1, c_2 \neq 0$  is responsible for nonlinearity in the system. The two delay terms introduce two

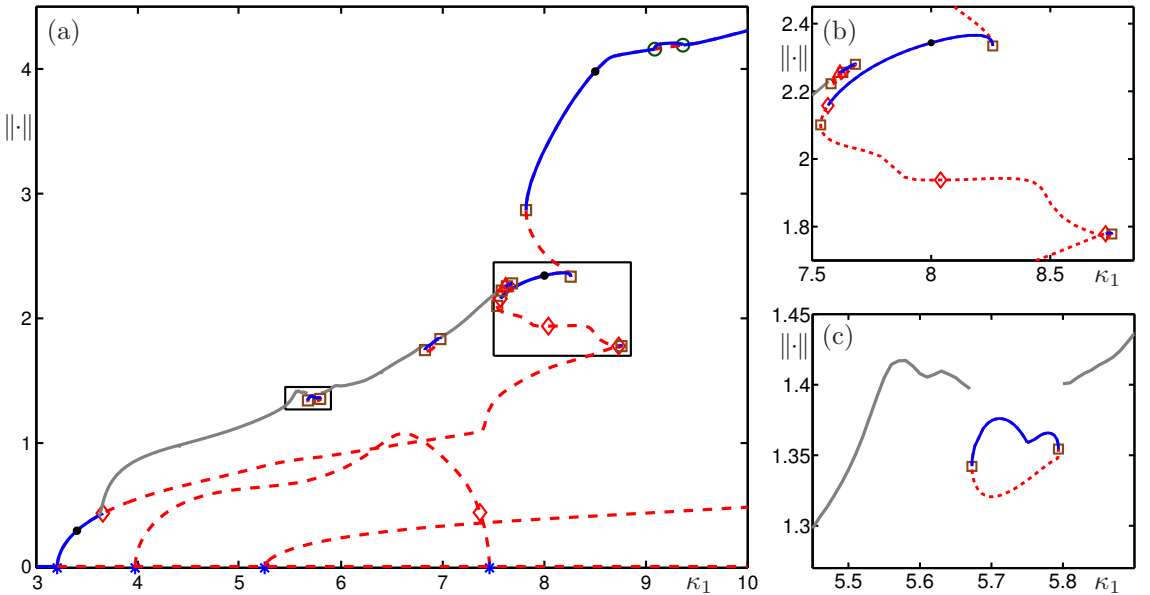


FIG. 1. One-parameter bifurcation diagram in  $\kappa_1$  of (1.3), showing the norm  $\|u(t)\| = \max u(t) - \min u(t)$  of periodic orbits bifurcating from Hopf bifurcations of the trivial solution (a). Stable orbits are shown as solid blue curves and unstable ones as dashed red curves; indicated are points of Hopf bifurcation (stars), saddle-node of limit cycle bifurcation (squares), period-doubling bifurcations (circles), and torus bifurcation (diamonds). Also shown is a grey curve of tori that bifurcate from the principal branch of periodic orbits at  $\kappa_1 \approx 3.6557$ . Panels (b) and (c) are two enlargements near the stable part of the principal branch and near an isola of periodic orbits associated with 1:4 phase locking. The black dots correspond to the stable periodic orbits shown in Fig. 2. Here  $\kappa_2 = 3.0$  and, throughout,  $\gamma = 4.75$ ,  $a_1 = 1.3$ ,  $a_2 = 6.0$  and  $c_1 = c_2 = 1.0$ . Reproduced with permission from [34]. Copyright 2012 American Institute of Mathematical Sciences.

oscillatory degrees of freedom into the system, which may then interact nonlinearly. As a result, the dynamics of the DDE (1.3) is no longer linear; rather it is, colloquially speaking, potentially at least as complicated as that of two coupled nonlinear oscillators with dissipation. Indeed, the interest in (1.3) arises from the fact that it is effectively the simplest example one can consider of a DDE with several state-dependent delays. In particular, any non-trivial dynamics that one finds must be due to the state dependence.

Throughout this paper we will take

$$\gamma = 4.75, \quad a_1 = 1.3, \quad a_2 = 6, \quad c_1 = c_2 = 1, \quad (1.10)$$

and vary the values of  $(\kappa_1, \kappa_2)$  with  $\kappa_2 \in (0, 4.75)$  to satisfy (1.4). The parameter set (1.10) was first identified as producing interesting dynamics for (1.3) in [34]. There, one-parameter bifurcation diagrams for (1.3) were produced for this parameter set with fixed values of  $\kappa_2$ . In [34], it was also noticed that the bifurcation diagram is topologically very different for other choices of parameters.

Fig. 1 illustrates the results obtained in [34] with  $\kappa_2 = 3$  and the other parameters given by (1.10), where the dynamics of (1.3) was explored by means of finding the Hopf bifurcations of the zero solution and continuing the branches of bifurcating periodic orbits. As panel (a) shows, the zero solution loses stability in a first Hopf bifurcation at  $\kappa_1 \approx 3.2061$  where a branch of stable periodic solutions emerges. These lose stability in a torus (or Neimark-Sacker) bifurcation at  $\kappa_1 \approx 3.6557$ . The branch of (unstable) saddle periodic solutions regains stability in the interval  $\kappa_1 \in [7.5665, 8.2585]$  after two saddle-node (or fold) bifurcations and several further torus bifurcations; see the enlargement in Fig. 1(b). A further two saddle-node bifurcations lead to a hysteresis loop of the branch



and the periodic solution is stable again for  $\kappa_1 > 7.82$ , except for  $\kappa_1 \in [9.0857, 9.3624]$  where a pair of period-doubling bifurcations lead to a short interval of stable period-doubled solutions. Also shown in Fig. 1(a) are branches of bifurcating stable tori, which are represented by the maximum of the norm along a numerically computed trajectory of sufficient length. As is expected from general theory one finds locked dynamics on the torus when  $\kappa_1$  passes through resonance tongues. The associated periodic orbits on the torus can be continued and Fig. 1(c) shows the isola of periodic solutions corresponding to 1:4 phase locking. Notice that there are further Hopf bifurcation points and bifurcating branches of periodic solutions in Fig. 1(a), but none of them are stable.

Figure 2 shows examples of stable periodic solutions from the three main ranges of stability discussed above, for values of  $\kappa_1$  as indicated by the black dots in Fig. 1(a). Shown in Fig. 2 are the time series of  $u(t)$  over one period and the orbit in projection onto  $(u(t), u(t - a_1)u(t - a_2))$ -space of the respective periodic solution. The periodic solution in row (a) of Fig. 2 is almost perfectly sinusoidal, as is expected immediately after a Hopf bifurcation. The periodic solution in row (b), on the other hand, features two local maxima and is close to a saw-tooth shape. Similarly, the periodic solution in Fig. 2(c) is very close to a simple saw-tooth, with a single linear rise and then a sharp drop in  $u(t)$ . Sawtooth periodic solutions and some of their bifurcations are considered in [33], where a singularly perturbed version of (1.3) is studied.

The results from [34], summarized in Figs. 1 and 2, clearly show that (1.3) features highly nontrivial dynamics due to the state dependence. On the other hand, a more detailed bifurcation analysis of the system has not been performed. The only two-parameter continuation performed in [34] is limited to that of the curves of Hopf bifurcations in the  $(\kappa_1, \kappa_2)$ -plane. It identified Hopf-Hopf (or double Hopf) bifurcations, but neither they nor the curves of torus bifurcations emerging from them were investigated in that work. Moreover, the bifurcating tori were not studied in detail in [34]; in particular, stable tori themselves were not computed when phase locked.

To highlight the full extent of the dynamics generated by the state dependence, in this work we present a bifurcation study of (1.3) that goes well beyond that in [34]. Our focus is on two-frequency dynamics and associated resonance phenomena; our main objects of study are the bifurcation diagram in the  $(\kappa_1, \kappa_2)$ -plane and the associated dynamics in phase space. The starting point of our investigation is the arrangement of the Hopf bifurcation curves of (1.3) shown in Fig. 3.

A Hopf bifurcation occurs when a complex conjugate pair of characteristic values crosses the imaginary axis in the linearized system. State-dependent DDEs are linearized around equilibria by first freezing the state-dependent delays at their steady-state values. This technique has long been applied heuristically, but more recently has been established rigorously by Györi and Hartung [24, 25] for a class of problems including (1.3). Hence, we obtain

$$u'(t) = -\gamma u(t) - \kappa_1 u(t - a_1) - \kappa_2 u(t - a_2) \quad (1.11)$$

as the linearization of (1.3) about the trivial steady state  $u \equiv 0$ . The characteristic equation for (1.11) is given by

$$0 = \lambda + \gamma + \kappa_1 e^{-a_1 \lambda} + \kappa_2 e^{-a_2 \lambda}, \quad (1.12)$$

and so at a Hopf bifurcation we have  $\lambda = \pm i\omega$  with

$$0 = i\omega + \gamma + \kappa_1 e^{-ia_1 \omega} + \kappa_2 e^{-ia_2 \omega}. \quad (1.13)$$

The three curves  $H_1$ ,  $H_2$  and  $H_3$  in Fig. 3 emerge from  $\kappa_2 = 0$  and are functions of  $\kappa_2$ . These three Hopf bifurcation curves are intersected by the curve  $H_u$ , which exists only above  $\kappa_2 \approx 2.627$  and is a function of  $\kappa_1$ . The three intersection points  $HH_1$ ,  $HH_2$  and  $HH_3$  are codimension-two points of Hopf-Hopf bifurcation. From (1.13) it follows that there are in fact infinitely many Hopf bifurcation curves of (1.3) as  $\kappa_1 \rightarrow \infty$  and, consequently, other Hopf-Hopf points; however, these

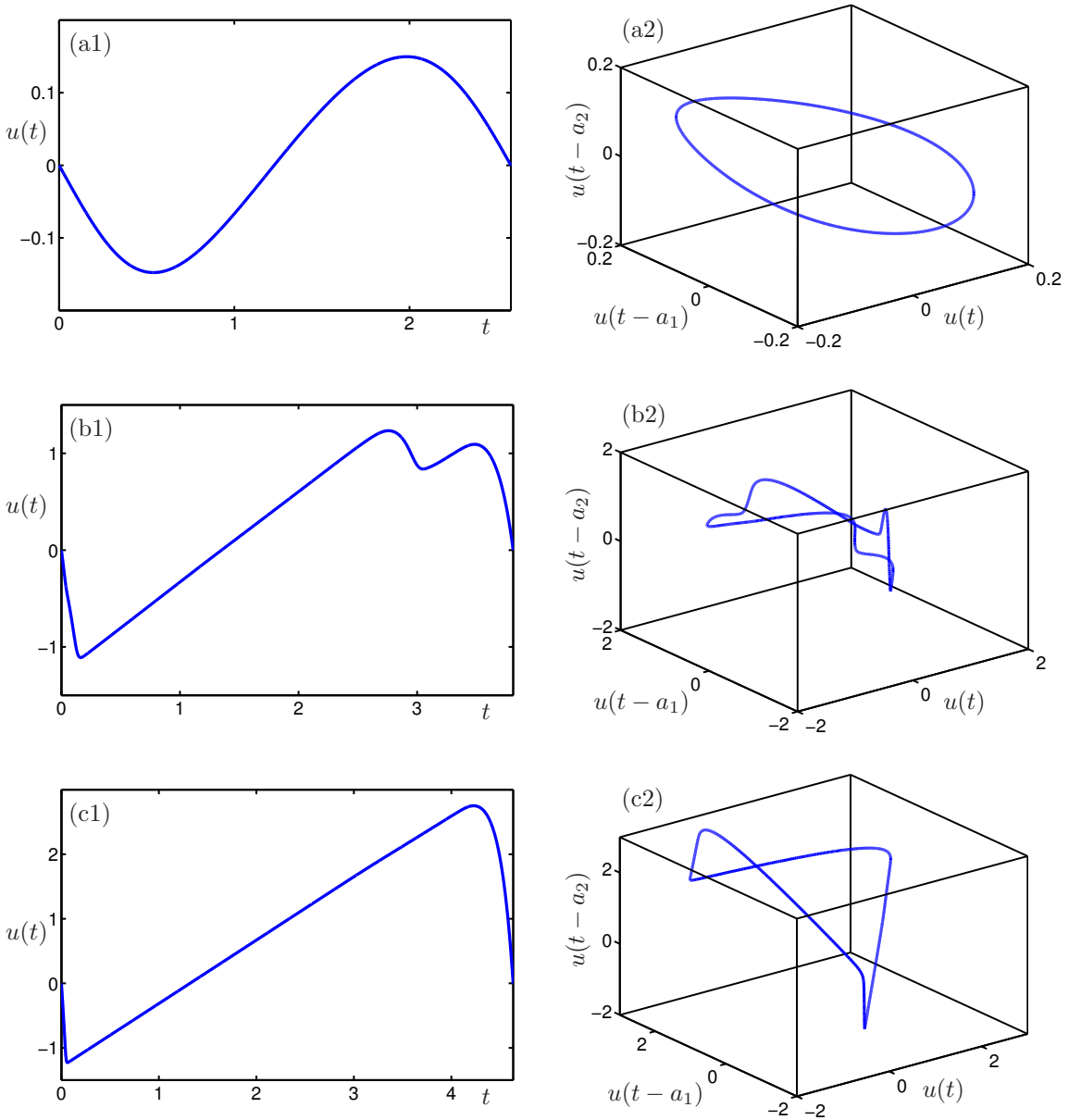


FIG. 2. Three stable periodic orbits from the principal branch in Fig. 1, shown as a time series over one period (left column) and in projection into  $(u(t), u(t - a_1), u(t - a_2))$ -space (right column); here  $\kappa_1 = 3.4$  in row (a),  $\kappa_1 = 8.0$  in row (b), and  $\kappa_1 = 8.5$  in row (c).

are not shown in Fig. 3 because we concentrate here on the  $\kappa_1$ -range of  $[0, 14]$ . Note that we only show the  $(\kappa_1, \kappa_2)$ -plane for  $\kappa_2 \leq \gamma = 4.75$ , because this is the  $\kappa_2$ -range for which we know that the state-dependent DDE is well posed.

The numerical computation of Hopf bifurcations in state-dependent DDEs has been implemented in the DDE-BIFTOOL software package [17, 72], and this capability actually predates their rigorous proof. Eichmann [16] was the first to establish a rigorous Hopf bifurcation theorem

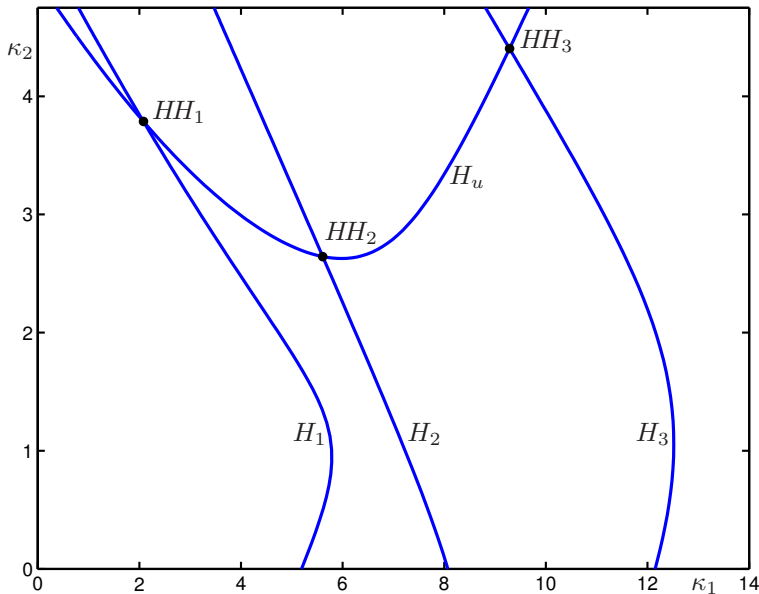


FIG. 3. Curves of Hopf bifurcation in the  $(\kappa_1, \kappa_2)$ -plane of (1.3); the upper Hopf bifurcation curve  $H_u$  intersects the Hopf bifurcation curves  $H_j$  for  $j = 1, 2, 3$  at Hopf-Hopf bifurcation points  $HH_j$ .

for state-dependent DDEs, but results have only appeared in the published literature much more recently [32, 71]. We perform here a calculation of the four-dimensional normal form ODE on the center manifold of the Hopf-Hopf points  $HH_1$ ,  $HH_2$  and  $HH_3$ . As far as we are aware, this is the first such calculation to determine the type of Hopf-Hopf bifurcations in a state-dependent DDE. The Hopf-Hopf normal form ODE with the multitude of cases that can arise in the unfolding is presented in detail in [51]. In constant-delay equations it has already been studied, see for instance [3]; the normal form procedure is also elaborated in [23] and has been implemented recently [78] as part of DDE-BIFTOOL [72] for constant delays only. Our approach is to derive a constant-delay DDE from the state-dependent DDE (1.3) by expanding the state dependence to sufficient order in (many) constant delays. The Hopf-Hopf normal form ODE can then be computed from this constant-delay DDE with established methods, and specifically we implemented the approach from [23]. In this way, we are able to determine the type of the Hopf-Hopf bifurcation and show that a pair of torus bifurcation curves emerges from each of the points  $HH_1$ ,  $HH_2$  and  $HH_3$ . The reduction to the constant-delay DDE and the corresponding resulting normal form coefficients are presented in Sec. 2, where we also compare our results with those obtained from the DDE-BIFTOOL implementation. Further details of the normal form calculations can be found in Appendix A. Our Matlab code `HHnfDDE`, which implements the constant-delay expansion and computes the normal form coefficients for the Hopf-Hopf bifurcation, is available as a supplement to this paper.

The dynamics on the bifurcating tori may be quasi-periodic or locked, and this is organised by resonance tongues that are bounded by curves of saddle-node (or fold) bifurcations of periodic orbits. We proceed in Sec. 3 by computing and presenting bifurcating stable quasiperiodic and phase-locked tori. The Matlab [63] state-dependent DDE solver `ddesd` is used to find trajectories on stable invariant tori. In this way, we find quasiperiodic (or high-period) tori. To obtain locked tori, we find and continue the locked periodic solutions with the software package DDE-BIFTOOL [17, 72]. The unstable manifolds of the saddle periodic orbits on the torus are then represented as two-dimensional surfaces obtained by numerical integration of trajectories in these manifolds.

Since (1.3) is a scalar DDE, but its phase-space is infinite dimensional, we consider finite-dimensional projections of the infinite-dimensional phase space. Moreover, we also show the tori in suitable projections of the Poincaré map defined by  $u(t)$  passing through 0. This allows us to reveal the inherently low-dimensional character of these invariant tori and associated bifurcations.

We then perform in Sec. 3.1 a bifurcation study of the emergence of tori and associated resonance phenomena. Specifically, we compute and illustrate in the  $(\kappa_1, \kappa_2)$ -plane the curves of torus bifurcation emerging from the Hopf-Hopf bifurcation point  $HH_1$  and the associated structure of resonance tongues. We also consider in detail the properties and bifurcations of the invariant tori inside and near the regions of strong 1:3 and 1:4 resonances. More specifically, in Sec. 3.2 we show how the 1:4 locked torus loses normal hyperbolicity and then breaks up in a complicated sequence of bifurcations as  $\kappa_1$  is changed. Finally, in Sec. 4 we present the overall bifurcation diagram in the  $(\kappa_1, \kappa_2)$ -plane, provide some conclusions and point out directions for future research.

**2. Normal form at Hopf-Hopf bifurcation.** Here we derive the normal form of the Hopf-Hopf bifurcations of (1.3). For constant-delay DDEs a center manifold reduction [3, 23] transforms the DDE into an ODE on the center manifold, and the normal form of the Hopf-Hopf bifurcation for ODEs is well known and can be found in [51]. For state-dependent DDEs, the existence of a  $C^1$  center-unstable manifold has been proved by several authors (for instance, see [69, 50, 76]), with verifiable regularity conditions that equation (1.3) satisfies, when the spectrum of (1.11) has eigenvalues  $\lambda$  satisfying that  $\text{Re}(\lambda) \geq 0$ . However, the existence of a  $C^3$  regular center-unstable manifold, as required for the Hopf-Hopf bifurcation analysis, has not been rigorously established in the state-dependent case. Nor has the normal form of the Hopf-Hopf bifurcation for a state-dependent DDE previously been elaborated.

Noting that linearization of (1.3) reduces it to the constant-delay DDE (1.11), our approach is instead to obtain a series expansion of the right-hand side of (1.3) in which the low-order terms only involve constant delays. In particular, the state dependency will only appear in the higher-order remainder term. The derivation of the terms up to order three of the normal form DDE with constant delays near the Hopf-Hopf bifurcation is exact. We then, as is usual in the field, disregard the remainder term and consider only this truncated expansion. We conjecture that the truncated constant-delay DDE fully describes all of the dynamics near the Hopf-Hopf bifurcation in the state-dependent DDE. We then proceed by applying the established center manifold reduction of [3, 23] to obtain an ODE on the center manifold. The flow restricted to the center manifold satisfies an ODE in four-dimensional space, which can be reduced to a normal form to determine the type of Hopf-Hopf bifurcation that occurs. The virtue of this method is that we study a four-dimensional ODE as opposed to an infinite dimensional semi-flow. Of course, this construction only works close to the point of the Hopf-Hopf bifurcation in parameter space, where the center manifold persists since the rest of the eigenvalues are at a positive distance from the imaginary axis; the center manifold should be a normally hyperbolic invariant manifold in the infinite-dimensional phase space.

Since the state dependency of the delays is the only source of nonlinearity in the DDE (1.3), the correct treatment of these state-dependent delays is essential to our results. Specifically, our strategy is as follows. We Taylor expand the state-dependent terms  $u(t - a_i - cu(t))$  in time about their constant-delay reductions  $u(t - a_i)$ . This removes the state dependency from the equations, but at the cost of introducing derivatives of  $u(t - a_i)$  in higher-order terms. Not wanting to deal with neutral DDEs, we remove the derivatives  $\frac{d^k}{dt^k} u(t - a_i)$  by differentiating (1.3)  $k - 1$  times and evaluating them at  $t - a_i$ . This introduces additional delays into the DDE, and also reintroduces the state dependency of the delays, but only in the quadratic and higher-order terms. The quadratic state-dependent delays are removed by the same process of Taylor expansion and substitution. We can repeat this process as many times as desired to obtain a DDE with only constant delays in

the terms up to  $k$ -th order for any  $k$ . Normal form theory for Hopf-Hopf bifurcation requires the expansion up to order three, which is why we stop at this order. By using the integral form of the remainder in Taylor's theorem, it is possible to obtain an explicit expression for the higher-order terms. In the current work, we conjecture, but do not prove, that the remainder term can indeed be disregarded. This allows us to apply the techniques of [3, 23] to the lower-order constant-delay part of our expanded DDE to determine the normal form equations, as well as the Hopf-Hopf unfolding bifurcation types.

There is a long and often inglorious history of Taylor expanding in DDEs to alter or eliminate the delay terms. It is obviously invalid to expand  $u(t-a)$  about  $u(t)$  when  $|u(t-a) - u(t)|$  is large, which will be the typical case when  $a$  is not small. But related to the phenomenon of delay induced instability, even when  $u$  is close to steady-state so that  $|u(t-a) - u(t)| \ll 1$ , expanding  $u(t-a)$  about  $u(t)$  can change the stability of the steady state; see [15] for examples. In the current work, we expand terms of the form  $u(t-a-cu(t))$  about  $u(t-a)$  close to steady state. Hence, not only is the difference in the  $u$ -values small, that is  $|u(t-a-cu(t)) - u(t-a)| \ll 1$ , but crucially the difference in the time values is also small, that is,  $|(t-a-cu(t)) - (t-a)| = |cu(t)| \ll 1$ .

Having found the normal form of the Hopf-Hopf bifurcation of (2.14) we compare the resulting bifurcations predicted by the normal form calculation with the numerically determined bifurcation curves for the full state-dependent DDE (1.3). Close to the Hopf-Hopf points we find very good agreement, which gives us confidence in the results obtained by both approaches. In particular, these results constitute strong numerical evidence that the resulting normal form for the expanded constant-delay DDE (2.14) is indeed that for the state-dependent DDE (1.3). While proving this conjecture is beyond the scope of this paper, we remark that such a proof, and indeed the expansions that we perform, require at least  $C^3$  regularity of (the solutions in) the manifold. To our knowledge, the best regularity result for the center manifolds in state-dependent DDEs establishes just  $C^1$  regularity [50], and  $C^r$  regularity with  $r > 1$  has not yet been established for center manifolds of state-dependent DDEs. Nevertheless, the expansions we perform here do not seem to present any obstruction to obtaining the formal expressions for small amplitudes of the function  $u$ . In fact, one notices that knowing the  $C^1$ -smoothness of the local center-unstable manifold justifies that the solutions can be continued for negative times. Since in our case we are close to the steady state  $u(t) = 0$ , the delays are bounded and the solutions must be  $C^k$  smooth in time. Indeed, having  $C^k$ -regular solutions could lead to obtaining  $C^k$  smooth time-1 maps, and these are perhaps the basis to construct a  $C^k$ -smooth center manifold. This possible route to  $C^k$  regularity is already proposed in [29]. We also mention that results for invariant tori of state dependent DDEs have been derived recently in spaces of smooth and analytic functions; see [30, 31].

We elaborate our steps as follows. In Sec. 2.1, we present the details of the expansion of the state-dependent DDE to obtain a DDE with only constant delays up to order three. In Sec. 2.2 we describe aspects of the projection onto the center manifold for this constant-delay DDE, and present the derivation of the normal form coefficients. The algebraic details of these calculations are contained in Appendix A. In Sec. 2.3 we use the normal form obtained to determine the type of the Hopf-Hopf bifurcation for the three Hopf-Hopf bifurcations seen in Fig. 3.

**2.1. Expansion of the nonlinearity.** In this section, we perform the expansion of the state dependent delay equation (1.3) and obtain a constant-delay equation with many delays and a remainder term which is small for solutions in the center or unstable manifolds.

To describe the expansion of the nonlinearity in (1.3) it is convenient to define the difference operator  $L$  that generates the linear terms on the right hand side of equation (1.11) as

$$Lu(t) \equiv -\gamma u(t) - \kappa_1 u(t-a_1) - \kappa_2 u(t-a_2). \quad (2.1)$$

The difference operator  $L$  can be applied recursively, and it will be useful below to note that

$$\begin{aligned} L^2 u(t - a_i) &= -\gamma Lu(t - a_i) - \sum_{j=1}^2 \kappa_j Lu(t - a_i - a_j) \\ &= \gamma^2 u(t - a_i) + 2\gamma \sum_{j=1}^2 \kappa_j Lu(t - a_i - a_j) + \sum_{j,m=1}^2 \kappa_j \kappa_m u(t - a_i - a_j - a_m). \end{aligned} \quad (2.2)$$

**THEOREM 2.1.** *For functions  $u$  in the center or unstable manifold of the steady state  $u(t) = 0$ , the state dependent delay equation (1.3) can be written as a constant-delay equation up to fourth order as*

$$\begin{aligned} u'(t) &= Lu(t) + \sum_{i=1}^2 \kappa_i cu(t) Lu(t - a_i) + \sum_{i,j=1}^2 \kappa_i \kappa_j c^2 u(t) u(t - a_i) Lu(t - a_i - a_j) \\ &\quad - \frac{1}{2} (cu(t))^2 \sum_{i=1}^2 \kappa_i L^2 u(t - a_i) + \mathcal{R}(t), \end{aligned} \quad (2.3)$$

with  $\mathcal{R}(t) = \mathcal{O}(\|u\|_5^4)$  where  $\|u\|_5 = \sup_{\theta \in [-5a_2, 0]} |u(\theta)|$ .

*Proof.* Recall from (1.8) that delays are globally bounded by  $\tau = a_2 + a_1(\kappa_1 + \kappa_2)/\gamma$  for the state-dependent DDE (1.3). Since  $a_2 > a_1$  for  $|u| < \delta$  we obtain the stronger bound that  $t - \alpha_j(t, u(t)) \leq a_2 + c\delta$ . Now consider  $u$  in the center or unstable manifold so that solutions can be extended in the past. Using (2.1) we can rewrite equation (1.11) as  $u'(t) = Lu(t)$  and equation (1.3) as

$$u'(t) = Lu(t) - \sum_{i=1}^2 \kappa_i [u(t - a_i - cu(t)) - u(t - a_i)]. \quad (2.4)$$

As already noted, the only nonlinearities in (1.3) arise from the state dependency of the delays, and we must handle these terms carefully to obtain a correct expansion for the normal form. Close to steady state and close to Hopf bifurcation, the state-dependent part of the delay term,  $-cu(t)$ , will be close to zero. Therefore, close to the bifurcation the term  $t - a_i - cu(t)$  represents a small displacement from the constant delay  $t - a_i$ . Since we assume  $a_i > 0$  the perturbation will not be singular.

We write Taylor's theorem as

$$\begin{aligned} u^{(p)}(w - \tau - cu(w)) &= u^{(p)}(w - \tau) + \int_0^1 u^{(p+1)}(w - \tau - cu(w) s_1) ds_1 (-cu(w)) \\ &= u^{(p)}(w - \tau) + u^{(p+1)}(w - \tau) (-cu(w)) \\ &\quad + \int_0^1 \int_0^{s_1} u^{(p+2)}(w - \tau - cu(w) s_1 s_2) ds_2 (-cu(w) s_1) ds_1 (-cu(w)) \\ &= \sum_{j=0}^k \frac{1}{j!} u^{(p+j)}(w - \tau) (-cu(w))^j \\ &\quad + \left( \int_0^1 \int_0^{s_1} \cdots \int_0^{s_{k-1}} u^{(p+j+1)}(w - \tau - cu(w) s_1 s_2 \cdots s_k) \right. \\ &\quad \left. \cdot [s_1(s_1 s_2) \cdots (s_1 \cdots s_k)] ds_k \cdots ds_1 \right) \cdot (-cu(w))^{j+1}, \end{aligned} \quad (2.5)$$

where we note that on the unstable and center manifolds solutions are  $C^p$ , because they can be extended backwards in time, the delays are bounded, and solutions become more regular as we integrate (1.3) forwards in time. Equation (2.5) gives an estimate of the residue of Taylor's theorem in terms of  $(-cu(w))^{j+1}$  and  $u^{(p+j+1)}$ . Now, we use (2.5) with  $w = t$ ,  $\tau = a_i$ ,  $p = 0$  and  $k = 2$  to obtain

$$\begin{aligned} u'(t) &= Lu(t) - \sum_{i=1}^2 \kappa_i \sum_{j=1}^2 \frac{1}{j!} u^{(j)}(t - a_i) (-cu(t))^j \\ &\quad + \left[ \sum_{i=1}^2 \kappa_i \int_0^1 \int_0^{s_1} \int_0^{s_2} u^{(3)}(t - a_i - cu(t)s_1s_2s_3) s_1^3 s_2^2 s_3 ds_3 ds_2 ds_1 \right] (-cu(t))^3. \end{aligned} \quad (2.6)$$

Note that we choose  $k = 2$  so that the integral remainder term is quartic; more precisely it is  $\mathcal{O}([u(t)]^3 u^{(3)}(t))$ . But with bounded delays it follows from differentiating (1.3) that for  $\delta > 0$  sufficiently small

$$\begin{aligned} |u^{(3)}(t - a_i - c\delta)| &\leq C_2 \sup_{\theta \in [-a_i - a_2 - 2c\delta, 0]} |u''(\theta)| \leq C_3 \sup_{\theta \in [-3a_2 - 3c\delta, 0]} |u'(\theta)| \\ &\leq C_4 \sup_{\theta \in [-4a_2 - 4c\delta, 0]} |u(\theta)| \leq C_4 \|u\|_5. \end{aligned} \quad (2.7)$$

One problem with the expansion (2.6) is that the nonlinear terms include delayed derivative terms in  $u'$ ,  $u''$  and  $u^{(3)}$ . We want to eliminate terms of this form to avoid the possibility of neutrality in our equations. To this end, we consider first the terms of the form  $u'(t - a_i)$  appearing in (2.6). Applying (1.3) gives

$$u'(t - a_i) = -\gamma u(t - a_i) - \sum_{j=1}^2 \kappa_j u(t - a_i - a_j - cu(t - a_i)).$$

To remove the state dependency from the right-hand side, we apply (2.5) with  $w = t - a_i$ ,  $\tau = a_j$ ,  $p = 0$  and  $k = 1$  to obtain

$$\begin{aligned} u'(t - a_i) &= -\gamma u(t - a_i) - \sum_{j=1}^2 \kappa_j u(t - a_i - a_j) + \sum_{j=1}^2 \kappa_j cu'(t - a_i - a_j) u(t - a_i) \\ &\quad + \left[ \sum_{j=1}^2 \kappa_j \int_0^1 \int_0^{s_1} u''(t - a_i - a_j - cu(t - a_i)s_1) s_1 ds_2 ds_1 \right] (-cu(t - a_i))^2. \end{aligned} \quad (2.8)$$

But using (1.3) again and (2.5) with  $w = t - a_i - a_j$ ,  $\tau = a_m$  and  $p = k = 0$  we have

$$\begin{aligned} u'(t - a_i - a_j) &= -\gamma u(t - a_i - a_j) - \sum_{m=1}^2 \kappa_m u(t - a_i - a_j - a_m - cu(t - a_i - a_j)) \\ &= -\gamma u(t - a_i - a_j) - \sum_{m=1}^2 \kappa_m u(t - a_i - a_j - a_m) \\ &\quad + \left[ \sum_{m=1}^2 \kappa_m \int_0^1 u'(t - a_i - a_j - a_m - cu(t - a_i - a_j)s_1) ds_1 \right] (-cu(t - a_i - a_j)). \end{aligned} \quad (2.9)$$



Hence, we can rewrite (2.6) as

$$u'(t) = Lu(t) + N_2u(t) + N_{23}u(t) - \frac{1}{2} \sum_{i=1}^2 \kappa_i u''(t - a_i) (cu(t))^2 + \mathcal{R}_{24}(t), \quad (2.10)$$

where  $N_2u(t)$  contains the quadratic terms in the expansion of nonlinearity, and  $N_{23}u(t)$  contains the cubic terms arising from the substitution of (2.9) and (2.8) into (2.6), with

$$N_2u(t) = \sum_{i=1}^2 \kappa_i cu(t) \left[ -\gamma u(t - a_i) - \sum_{j=1}^2 \kappa_j u(t - a_i - a_j) \right] = \sum_{i=1}^2 \kappa_i cu(t) Lu(t - a_i), \quad (2.11)$$

$$\begin{aligned} N_{23}u(t) &= \sum_{i,j=1}^2 \kappa_i \kappa_j c^2 u(t) u(t - a_i) \left[ -\gamma u(t - a_i - a_j) - \sum_{m=1}^2 \kappa_m u(t - a_i - a_j - a_m) \right] \\ &= \sum_{i,j=1}^2 \kappa_i \kappa_j c^2 u(t) u(t - a_i) Lu(t - a_i - a_j). \end{aligned} \quad (2.12)$$

The expression  $\mathcal{R}_{24}(t)$  contains the fourth-order integral remainder term of the Taylor series stated in (2.6), as well as the additional fourth order integral terms arising from the substitution of (2.8) and (2.9) into (2.6).

It remains to expand the terms  $u''(t - a_i)$  in (2.10). Differentiating (1.3) and then applying (2.5) with  $p = 1$  and  $k = 0$ , gives

$$\begin{aligned} u''(t - a_i) &= -\gamma u'(t - a_i) - (1 - cu'(t - a_i)) \sum_{j=1}^2 \kappa_j u'(t - a_i - a_j - cu(t)) \\ &= -\gamma u'(t - a_i) - (1 - cu'(t - a_i)) \sum_{j=1}^2 \kappa_j \left[ u'(t - a_i - a_j) \right. \\ &\quad \left. + \int_0^1 u'(t - a_i - a_j - cu(t - a_i)s_1) ds_1 (-cu(t - a_i)) \right]. \end{aligned} \quad (2.13)$$

Similar to (2.8) and (2.9), but this time applying (2.5) with  $p = k = 0$ , we can remove the  $u'(t - a_i)$  and  $u'(t - a_i - a_j)$  terms from (2.13). Just considering the linear terms in (2.13) and using (2.2)

we find that

$$\begin{aligned}
& -\gamma u'(t - a_i) - \sum_{j=1}^2 \kappa_j u'(t - a_i - a_j) \\
&= -\gamma \left[ -\gamma u(t - a_i) - \sum_{j=1}^2 \kappa_j u(t - a_i - a_j - cu(t - a_i)) \right] \\
&\quad - \sum_{j=1}^2 \kappa_j \left[ -\gamma u(t - a_i - a_j) - \sum_{m=1}^2 \kappa_m u(t - a_i - a_j - a_m - cu(t - a_i - a_j)) \right] \\
&= -\gamma \left[ -\gamma u(t - a_i) - \sum_{j=1}^2 \kappa_j \left[ u(t - a_i - a_j) \right. \right. \\
&\quad \left. \left. + \int_0^1 u'(t - a_i - a_j - cu(t - a_i)s_1) ds_1 (-cu(t - a_i)) \right] \right] \\
&\quad - \sum_{j=1}^2 \kappa_j \left[ -\gamma u(t - a_i - a_j) - \sum_{m=1}^2 \kappa_m \left[ u(t - a_i - a_j - a_m) \right. \right. \\
&\quad \left. \left. + \int_0^1 u'(t - a_i - a_j - a_m - cu(t - a_i - a_j)s_1) ds_1 (-cu(t - a_i - a_j)) \right] \right] \\
&= L^2 u(t - a_i) + \sum_{j=1}^2 \gamma \kappa_j \int_0^1 u'(t - a_i - a_j - cu(t - a_i)s_1) ds_1 (-cu(t - a_i)) \\
&\quad + \sum_{j,m=1}^2 \kappa_j \kappa_m \int_0^1 u'(t - a_i - a_j - a_m - cu(t - a_i - a_j)s_1) ds_1 (-cu(t - a_i - a_j)).
\end{aligned}$$

Hence, from (2.10) we obtain (2.3), where the remainder term  $\mathcal{R}(t)$  contains all the integral terms derived above. Equation (2.7) can be used to show that the remainder term in (2.6) is  $\mathcal{O}(\|u\|_5^4)$ , and all the remaining integral remainder terms are seen to be  $\mathcal{O}(\|u\|_5^4)$  similarly.  $\square$

Overall, we have transformed the state-dependent DDE (1.3) into DDE (2.3) whose terms up to order three contain only constant delays. The price for doing this is the introduction of additional delay terms. While (1.3) contains two state-dependent delays, and its linearization contains two constant delays, in equation (2.3) the second-order terms features five and the third-order terms nine constant delays. Indeed, it is easy to see that, if we continued the expansion in (2.6) to higher order, then the term  $-(-cu(t)^j) \sum_{i=1}^2 \kappa_i u^{(j)}(t - a_i)$  leads to a  $j^{\text{th}}$ -order term of the form  $-(-cu(t)^j) \sum_{i=1}^2 \kappa_i L^j u(t - a_i)$ . Thus, when  $a_1$  and  $a_2$  are not rationally related, we will obtain  $j(j+3)/2$  delays at  $j^{\text{th}}$ -order, namely all the terms of the form  $u(t - ma_1 - na_2)$  where  $m, n$  are nonnegative integers and  $1 \leq m + n \leq j$ . Recalling that  $a_2 > a_1$  the largest delay appearing at  $j^{\text{th}}$ -order is then  $u(t - ja_2)$ .

If desired the derivatives of  $u$  that appear in  $\mathcal{R}(t)$  can all be removed by using (1.3) and derivatives of that equation, just as we removed such derivatives from the lower-order terms. This would result in state-dependent delays appearing in the  $\mathcal{R}(t)$ . Alternatively the state dependency or distributed delay terms could be moved to higher-order terms by truncating the expansions above at higher order. Importantly, the remainder terms are beyond the orders that we will need for subsequent normal form consideration, and we have the following.

**CONJECTURE 2.2.** *The local dynamics near the steady state  $u(t) = 0$  of the state dependent delay equation (1.3) are determined solely by the constant-delay expansion up to the given order.*

In other words, to study steady-state bifurcations of (1.3) standard normal form calculations for constant-delay DDEs can be applied to the constant-delay expansion truncated to suitable order.

Specifically for the Hopf-Hopf bifurcations of interest, from now on we consider only the constant-delay DDE we derived to third order in (2.3). Not using the difference operator  $L$ , it takes the form

$$\begin{aligned} u'(t) = & \quad (2.14) \\ & -\gamma u(t) - \kappa_1 u(t - a_1) - \kappa_2 u(t - a_2) - \sum_{i=1}^2 \kappa_i c u(t) \left[ \gamma u(t - a_i) + \sum_{j=1}^2 \kappa_j u(t - a_i - a_j) \right] \\ & - \sum_{i,j=1}^2 \kappa_i \kappa_j c^2 u(t) u(t - a_i) \left[ \gamma u(t - a_i - a_j) + \sum_{m=1}^2 \kappa_m u(t - a_i - a_j - a_m) \right] \\ & - \frac{1}{2} (c u(t))^2 \sum_{i=1}^2 \kappa_i \left[ \gamma^2 u(t - a_i) + 2\gamma \sum_{j=1}^2 \kappa_j u(t - a_i - a_j) + \sum_{j,m=1}^2 \kappa_j \kappa_m u(t - a_i - a_j - a_m) \right]. \end{aligned}$$

We remark that this way of writing the constant-delay DDE is convenient for the implementation of the DDE-BIFTOOL normal form computations which require a DDE with constant delays, and in the supplemental material as `sys_cub_rhs` we provide a DDE-BIFTOOL system definition of (2.14). However, our own Hopf-Hopf normal form code `HHnfDDE` works directly from the state-dependent DDE (1.3), and computes (2.14) from (1.3) using symbolic differentiation as the first step for deriving the normal form parameters.

**2.2. Center manifold reduction and resulting normal form.** The next step is to derive the normal form for the constant-delay DDE (2.14). For constant-delay DDEs there are well established techniques for deriving normal forms through center manifold reductions. To the best of our knowledge, the Hopf-Hopf bifurcation for a constant-delay DDE was first elaborated in Bélair and Campbell [3], but here we follow the derivation of Wu and Guo [23]. The main idea in this construction is to study the restriction of the semi-flow of (2.14) to the center manifold at the point of the Hopf-Hopf bifurcation. On the center manifold the flow satisfies an ODE in four-dimensional space. The reduction to normal form for Hopf-Hopf bifurcations of ODEs is well known, and we follow Kuznetsov [51] to determine the type of Hopf-Hopf bifurcation that occurs.

The algebraic steps to determine the normal form are detailed in Appendix A in the supplementary materials, and we implemented our own Matlab code `HHnfDDE` which uses symbolic differentiation to compute the expansion of the state-dependent DDE (1.3) described in Sec. 2.1, and then to evaluate the normal form expressions for the resulting constant delay DDE (2.14). To determine the location of the codimension-two Hopf-Hopf points under consideration, we start from an approximate location and solve for  $(\kappa_1, \kappa_2, \omega_1, \omega_2)$  so that the pair of frequencies  $\omega_1 \neq \omega_2$  both solve (1.13) simultaneously for the same pair of parameter values  $(\kappa_1, \kappa_2)$ . Our auxiliary routine `findHH` uses the Matlab function `fminsearch` to minimise

$$f(\kappa_1, \omega_1, \kappa_2, \omega_2) = \sum_{j=1}^2 \left( \gamma + \kappa_1 \cos(a_1 \omega_j) + \kappa_2 \cos(a_2 \omega_j) \right)^2 + \left( \omega_j - \kappa_1 \sin(a_1 \omega_j) - \kappa_2 \sin(a_2 \omega_j) \right)^2,$$

since this function contains the real and imaginary parts of two copies of (1.13). In this way, we are able to find the Hopf-Hopf point essentially to machine precision (we use tolerances of  $10^{-14}$ ). At the Hopf-Hopf point we then evaluate the derivatives and functions needed to obtain the center manifold coefficients  $g_{l_{srk}}^j$  in Sec. A.3 of the supplemental materials, where we employ symbolic differentiation to avoid numerical errors. Thus, we expect that our normal form parameter calculations should be accurate essentially to machine precision, and certainly to eight or more significant figures.

	Computed Normal Form	DDE-BIFTOOL			
		$H_1$ High	$H_1$ Low	$H_u$ High	$H_u$ Low
$\kappa_1$	2.080920227069894	2.080905301795540		2.080662320398254	
$\kappa_2$	3.786800923405767	3.786811738802836		3.786929718494380	
$\omega_1$	2.487102830659818	2.487103286770640		1.582142631415513	
$\omega_2$	1.582152129599611	1.582151566193548		2.487110459273053	
$\vartheta$	5.291049995477200	5.2909997813	5.2909980111	-0.0222756426	-0.0222756534
$\delta$	-0.022289571330147	-0.0222816360	-0.0222817195	5.2909133110	5.2909132195

TABLE 1

Values of  $\kappa_i$  and  $\omega_i$  at the Hopf-Hopf bifurcation  $HH_1$ , seen in Fig. 3, and the parameters  $\vartheta$  and  $\delta$  that define the scaled truncated amplitude equation (2.15). The values in the first column are computed with our Matlab code `HHnfDDE` applied to (1.3), which implements the procedure described in Appendix A. The other columns are produced with the normal form extension of DDE-BIFTOOL, applied to the constant-delay DDE (2.14) to obtain four different approximations, two on each of the two intersecting branches of Hopf bifurcations, one from a low order approximation finite difference approximation to the derivatives and one using a higher-order approximation. The matlab code to generate all output is supplied in the Supplementary Materials.

Recently, Wage [78] implemented an extension `ddebiftool_nmfm` for DDE-BIFTOOL to compute normal form coefficients at local bifurcations of steady states in constant-delay DDEs. This applies a sun-star calculus based normalisation technique to compute the normal form and center manifold coefficients together, as elaborated for constant-delay DDEs by Janssens [37]. The DDE-BIFTOOL implementation only applies to constant-delay DDEs, and so cannot be applied directly to (1.3). However, we can use DDE-BIFTOOL to compute the normal forms of the Hopf-Hopf points of the expanded constant-delay DDE (2.14). The difference between the DDE-BIFTOOL implementation (sun-star calculus approach to compute normal form and center manifold coefficients together) and our approach (center manifold reduction first, then compute normal form of resulting ODE system) results in intermediate coefficients being scaled differently, but the final normal form coefficients computed by both methods should agree. For the DDE-BIFTOOL computations it is suggested to supply a user-defined routine to compute higher-order derivatives. However, with nine delays in the constant-delay DDE (2.14), determining these derivatives would be a formidable task, and so we use the default DDE-BIFTOOL finite-difference derivative approximations. As an error control this computes the normal form coefficients twice with finite difference approximations of different order. However, in our experience this error estimate is often misleading as the actual errors are usually much larger than the estimate, as we will see in the next section.

**2.3. Hopf-Hopf normal forms.** We perform the normal form analysis for the parameter values given in (1.10), which are the same as used in Fig. 3 and throughout this paper. For these parameter values the locations of the Hopf-Hopf points and the resulting normal form parameters can be found as described in the previous section.

In Table 1 we state the results of five different computations for the first Hopf-Hopf point  $HH_1$ . The normal form parameters  $\vartheta$  and  $\delta$  define coefficients in the scaled truncated amplitude equations

$$\begin{aligned}\xi'_1 &= \xi_1(\mu_1 - \xi_1 - \vartheta\xi_2), \\ \xi'_2 &= \xi_2(\mu_2 - \xi_2 - \delta\xi_1),\end{aligned}\tag{2.15}$$

for  $\xi_j \geq 0$ , which determine the dynamics and bifurcations seen as  $\mu_j = \text{Re}(\lambda_j)$  are varied close to the Hopf-Hopf point where  $\mu_1 = \mu_2 = 0$ . The derivation of (2.15) is given in Appendix A, culminating in equation (A.46).

The first column of Table 1 gives the values computed with our `HHnfDDE` code described in Secs. 2.1-2.2; for comparison the other columns give values computed with DDE-BIFTOOL's nor-

	$HH_1$	$HH_2$	$HH_3$
$\kappa_1$	2.080920227069894	5.608860749294630	9.284862308872761
$\kappa_2$	3.786800923405767	2.643352614515402	4.403906490530705
$\omega_1$	2.487102830659818	6.608351858283422	10.93073224661102
$\omega_2$	1.582152129599611	1.765757669232216	1.952009077103193
$\tilde{g}_{2100}^1 = \frac{1}{2}g_{2100}^1$	$-0.81417665 - 0.00407087i$	$-8.59821703 - 10.3402562i$	$8.25785960 - 81.8392092i$
$\tilde{g}_{1011}^1 = g_{1011}^1$	$-0.72563615 + 0.26699379i$	$-4.14512262 - 0.48508142i$	$-20.2850232 + 11.4745454i$
$\tilde{g}_{1110}^2 = g_{1110}^2$	$-0.45302394 - 0.29997922i$	$1.74982076 - 7.92866388i$	$31.0314747 - 74.3567344i$
$\tilde{g}_{0021}^2 = \frac{1}{2}g_{0021}^2$	$-0.13405924 - 0.29906145i$	$-1.42981504 - 0.22951923i$	$-0.26054578 - 0.38071817i$
$G_{2100}^1(0)$	$-0.69871613 - 0.28257330i$	$-7.50609582 - 4.15081310i$	$-16.8534773 - 28.0243853i$
$G_{1011}^1(0)$	$-0.51573055 - 0.23247968i$	$-5.26325881 + 0.05175630i$	$-21.3834727 + 12.4878724i$
$G_{1110}^2(0)$	$0.01557408 - 0.46117993i$	$5.55956094 - 2.01536072i$	$50.3666025 - 66.5262024i$
$G_{0021}^2(0)$	$-0.09747225 - 0.22785268i$	$-0.65677277 - 0.20185598i$	$-0.20383503 + 0.19032437i$
$p_{11}$	$-0.698716133454477$	$-7.506095827847883$	$-16.853477387548608$
$p_{12}$	$-0.515730558790600$	$-5.263258815778782$	$-21.383472731028913$
$p_{21}$	$0.015574083096158$	$5.559560941739119$	$50.366602528819492$
$p_{22}$	$-0.097472252054214$	$-0.656772770545075$	$-0.2038350368172633$
$\vartheta$	$5.291049995477200$	$8.013820078762780$	$104.90577608695922$
$\delta$	$-0.022289571330147$	$-0.740672790388973$	$-2.9884991311069409$

TABLE 2

The locations and the main normal form and amplitude equation parameters at the three Hopf-Hopf points  $HH_j$  shown in Fig. 3, computed with our Matlab code `HHnfDDE`.

mal form extension. DDE-BIFTOOL finds Hopf-Hopf points by checking along a branch of Hopf bifurcations for where a second pair of characteristic values crosses the imaginary axis. Thus, with DDE-BIFTOOL, it is possible to obtain two different approximations to the same Hopf-Hopf point by searching along each of the two intersecting branches of Hopf points; in Table 1 we give the locations of  $HH_1$  found on the Hopf curves  $H_1$  and  $H_u$  (see Fig. 3). As noted in Sec. 2.2, when computing derivatives via finite-differences, DDE-BIFTOOL provides two different finite-difference approximations to give an indication of the error. The parameters  $\vartheta$  and  $\delta$  computed on  $H_1$  with the two different finite difference approximations agree to a relative error of about  $10^{-6}$ , indicating that the finite-difference approximations are both quite accurate, and similarly on the branch  $H_u$ . However, the agreement is not so good when we compare the answers obtained on the two branches. Firstly, we see that the values of  $\vartheta$  and  $\delta$  are swapped on the two branches, which is correct and natural. DDE-BIFTOOL takes as  $\omega_1$  the value of  $\omega$  for the Hopf bifurcation occurring on the branch one is searching along, and takes as  $\omega_2$  the value of  $\omega$  for the second pair of characteristic values crossing the imaginary axis. Hence, the values of  $\omega_1$  and  $\omega_2$  are swapped when the search is switched from one branch to the other, and this results in the values of  $\vartheta$  and  $\delta$  also being swapped. However, even after swapping, we see that the values of  $\vartheta$  and  $\delta$  calculated by DDE-BIFTOOL only agree to about four significant figures between the two branches. This also indicates the relative accuracy to which the values of  $\kappa_1$ ,  $\kappa_2$ ,  $\omega_1$  and  $\omega_2$  for the Hopf-Hopf point agree on the two branches. So it seems that the accuracy of the DDE-BIFTOOL computed normal forms is limited by the accuracy to which DDE-BIFTOOL computes the location of the Hopf-Hopf points, and not by the accuracy to which it computes the normal forms themselves.

We can also swap the  $\omega_j$  in the computation of the normal forms in our code `HHnfDDE`. Because of the symmetry between the parameters, for the index  $j = 1$  or  $2$  so that  $3 - j$  indicates the other index, swapping the  $\omega$  values  $\omega_j \leftrightarrow \omega_{3-j}$  exchanges  $\vartheta$  and  $\delta$  and the other normal form coefficients (see Appendix A) as follows:

$$g_{lsrk}^j \leftrightarrow g_{rkls}^{3-j}, \quad \tilde{g}_{lsrk}^j \leftrightarrow \tilde{g}_{rkls}^{3-j}, \quad G_{lsrk}^j \leftrightarrow G_{rkls}^{3-j}, \quad p_{ij} \leftrightarrow p_{3-i3-j}.$$

Because we find the Hopf-Hopf point to machine precision and evaluate the derivatives symbolically, when the  $\omega_j$  are exchanged, we find that the respective normal form coefficients are identical to machine precision. In fact, the idea of swapping the  $\omega_j$  and checking the normal form coefficients and parameters turned out to be very useful during the checking and debugging of our code.

Table 2 gives the normal form parameters for the first three Hopf-Hopf points  $HH_j$  seen in Fig. 3, and also some of the more important intermediate coefficients described in Appendix A. Here we report only one set of normal form parameters for each Hopf-Hopf point  $HH_j$  computed with our Matlab code `HHnfDDE`. We always take  $\omega_1 > \omega_2$  and, since the period of the periodic orbit bifurcating from the curve  $H_u$  is always the largest, this corresponds to taking  $\omega_1$  as the frequency of the Hopf bifurcation  $H_j$  for  $j = 1, 2$  or  $3$ , and  $\omega_2$  as the frequency of the Hopf bifurcation  $H_u$ . Our normal form calculations give the following overall result.

**PROPOSITION 2.3.** *At each of the three Hopf-Hopf points  $HH_1$ ,  $HH_2$  and  $HH_3$*

- (i)  $p_{11} < 0$  and  $p_{22} < 0$ , which means that normal form coefficients  $\vartheta$  and  $\delta$  are sufficient to determine the type of the Hopf-Hopf bifurcation that occurs [51];
- (ii) the non-degeneracy conditions (HH.0)-(HH.6) in Appendix A hold; and
- (iii)  $\vartheta > 0 > \delta$ , which corresponds to subcase III of the simple case as described in Sec. 8.6.2 of [51]; see also Appendix A.5.

In the normal form parameters plane of  $(\mu_1, \mu_2) = (\text{Re}(\lambda_1), \text{Re}(\lambda_2))$ , Hopf bifurcations occur along the horizontal  $\mu_1$ -axis with the bifurcating periodic orbit existing in the upper half plane, and along the vertical  $\mu_2$ -axis with the bifurcating periodic orbit existing in the right half plane. Proposition 2.3 implies that there are two curves of torus bifurcations emerging from the origin, which is the codimension-two Hopf-Hopf point: one in the first quadrant and one in the fourth quadrant, with the torus existing in the convex cone between them. On the upper torus bifurcation curve the torus bifurcates from the periodic orbit that exists in the upper half plane, and on the lower torus bifurcation curve it bifurcates from the periodic orbit which exists in the right half plane. The five regions of generic phase portraits are labelled in panel III of Fig. 8.25 in [51] (but notice a typo: 13 should be 12), and the corresponding generic phase portraits are given in Fig. 8.26 of [51].

Figure 4 shows how our normal form calculations manifest themselves near  $HH_1$  and  $HH_2$ . Panels (a1) and (b1) show the local bifurcation diagrams of the original state-dependent DDE (1.3) as computed with DDE-BIFTOOL [72], consisting of the Hopf bifurcation curve  $H_u$  intersecting the Hopf bifurcation curves  $H_1$  and  $H_2$  in  $HH_1$  and  $HH_2$  (as in Fig. 3), as well as the associated torus bifurcation curves  $T_u$ ,  $T_1$  and  $T_2$ . Panels (a2) and (a3) and panels (b2) and (b3) of Fig. 4 show the results of our normal form calculations at  $HH_1$  and  $HH_2$ , respectively. Panels (a3) and (b3) show the positions of the curves of torus bifurcation in the  $(\mu_1, \mu_2)$ -plane of the normal form (2.15). As was discussed,  $T_u$  lies in the first quadrant and the curves  $T_1$  and  $T_2$  each lie in the fourth quadrant. Moreover, the normal form calculations also give the slope of the torus curves in the  $(\mu_1, \mu_2)$ -plane via the actual values of  $\vartheta$  and  $\delta$  and (A.50) and (A.51). In particular,  $T_1$  lies very close to  $H_u$  near  $HH_1$  in panel (a3), while  $T_2$  is well separated from  $H_u$  near  $HH_2$  in panel (b3). Since the Jacobian matrix defined in nondegeneracy condition (HH.6) in Appendix A.5 is invertible at each point  $HH_j$ , we can use the coordinate transformation (A.52) to map the  $(\mu_1, \mu_2)$ -plane back to the  $(\kappa_1, \kappa_2)$ -plane of (1.3). The result is shown in panels (a2) and (b2) of Fig. 4, where all curves are actually straight lines that represent the linear approximations, that is, the slopes, of the respective Hopf and torus bifurcation curves near  $HH_1$  and  $HH_2$ . There is excellent correspondence between the nature, order and slopes of the respective bifurcation curves illustrated in panels (a1) and (a2) and in panels (b1) and (b2), respectively. This fact is clear evidence, over and above the two independent normal form calculations, that Proposition 2.3 is correct and indeed represents the Hopf-Hopf normal form of the full state-dependent DDE (1.3).

Clearly, the bifurcation curves in the local bifurcation diagrams in Fig. 4(a1) and (b1) are

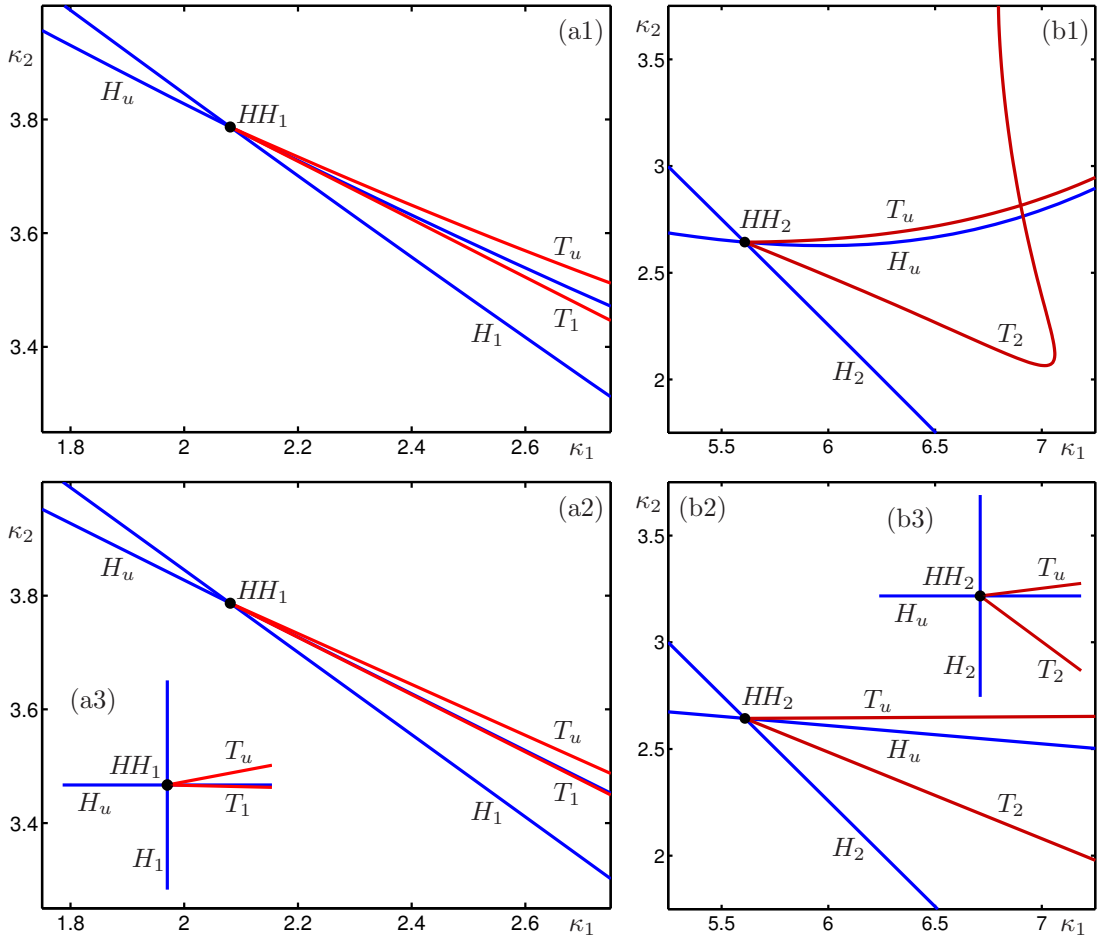


FIG. 4. Comparison in the  $(\kappa_1, \kappa_2)$ -plane near  $HH_1$  and  $HH_2$  between numerically computed torus bifurcation curves for the state-dependent DDE (1.3) in panels (a1) and (b1), and their linear approximations in panels (a2) and (b2) obtained by evaluating the normal form coefficients at the respective Hopf-Hopf point and applying the coordinate transformation (A.52). The inset panels (a3) and (b3) show the  $(\mu_1, \mu_2)$ -plane of the normal form (2.15) before this transformation.

actually nonlinear, and this explains the visible differences with panels (a2) and (b2) further away from  $HH_1$  and  $HH_2$ , respectively. The curvature of these bifurcation curves could be captured by computing higher-order terms in the normal forms, but this is very cumbersome and rarely done. Rather, we will continue these bifurcation curves numerically with DDE-BIFTOOL more globally throughout the  $(\kappa_1, \kappa_2)$ -plane. As we will see in the next section, the full bifurcation diagram is very complicated.

**3. Structure of bifurcating tori.** The existence of Hopf-Hopf bifurcation points that give rise to torus bifurcation curves clearly indicates that (1.3) should feature multi-frequency dynamics and, in particular, quasi-periodic and locked dynamics on invariant tori.

Figure 5 shows two examples of dynamics on an invariant torus, which were obtained by numerical integration of (1.3) and after transients have been allowed to die down. The respective dynamics on the torus are illustrated in the left column in projection onto the  $(u(t), u(t - a_1), u(t - a_2))$ -space. The right column shows points in the  $(u(t - a_1), u(t - a_2))$ -plane whenever  $u(t) = 0$ . In



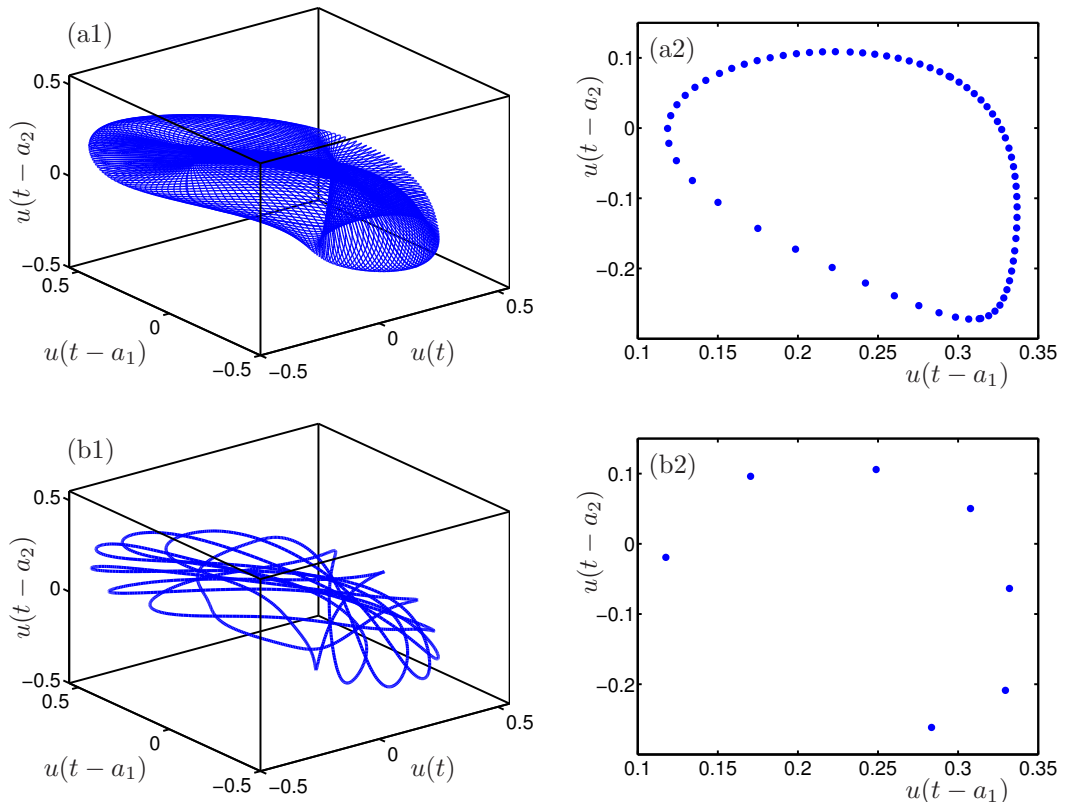


FIG. 5. Quasi-periodic torus for  $\kappa_1 = 4.44$  in row (a) and 3:7 phase-locked periodic orbit for  $\kappa_1 = 4.409556$  in row (b), where  $\kappa_2 = 3.0$ . Panels (a1) and (b1) show projections onto  $(u(t), u(t-a_1), u(t-a_2))$ -space, and panels (a2) and (b2) the trace in the  $(u(t-a_1), u(t-a_2))$ -plane of the Poincaré return map defined by  $u(t) = 0$ .

other words, it shows a two-dimensional projection of the function segments of the Poincaré return map defined by  $u(t) = 0$ . This representation in the  $(u(t-a_1), u(t-a_2))$ -plane has been chosen to give a good impression of the low-dimensional character of the tori we encounter, and we refer to it as the Poincaré trace for short; see below for more details on how to construct a Poincaré map of a DDE. In Fig. 5(a) the dynamics are quasi-periodic (or of very high period) so that the shown single trajectory covers the torus densely; in the Poincaré trace this corresponds to an invariant closed curve, which is filled out denser and denser as a longer trajectory is computed. An example of locked dynamics on the torus is given in row (b) of Fig. 5. More specifically, shown is the attracting periodic orbit on the torus (not shown) in projection onto  $(u(t), u(t-a_1), u(t-a_2))$ -space in panel (b1), and the associated Poincaré trace in the  $(u(t-a_1), u(t-a_2))$ -plane in panel (b2). They show that the locked periodic orbit forms a 3:7 torus knot.

Overall, Fig. 5 illustrates that two-dimensional invariant tori of (1.3) can be represented conveniently in projection onto the three-dimensional  $(u(t), u(t-a_1), u(t-a_2))$ -space and by their Poincaré trace in the  $(u(t-a_1), u(t-a_2))$ -plane. We now discuss the choice of Poincaré map for the state-dependent scalar DDE (1.3) in somewhat more detail. It is easy to see that  $u \equiv 0$  is the unique steady state of (1.3). Equation (1.8) and the positivity of the parameters implies that any orbit that does not cross  $u = 0$  will be eventually monotonic, and also that  $u(t)$  and  $u'(t)$  cannot have the same sign on a time interval longer than  $\tau$ . Hence, since all periodic and quasi-periodic orbits cross  $u = 0$ , it is natural to use this condition for defining the Poincaré map. More specifically,

we define the Poincaré section

$$\Sigma = \{\phi \in C : \phi(0) = 0\}, \quad (3.1)$$

which is a codimension-one subspace of the infinite-dimensional phase space  $C$  of (1.3). Hence,  $\Sigma$  is infinite dimensional itself, and the local Poincaré map  $P_\Sigma$  on  $\Sigma$  is defined as the map that takes a downward transversal crossing of zero ( $\phi(0) = 0$  with  $\phi'(0) < 0$ ) to the next such crossing. The infinite dimensionality of  $\Sigma$  obscures the structure of the low-dimensional invariant sets (namely periodic orbits and tori) we wish to visualize, which is why one considers projections of  $C$  and, hence,  $\Sigma$ .

We consider the projection  $\mathcal{P} : C \rightarrow \mathbb{R}^3$  via

$$\mathcal{P}u_t = (u_t(0), u_t(-a_1), u_t(-a_2)) = (u(t), u(t - a_1), u(t - a_2)) \in \mathbb{R}^3, \quad (3.2)$$

with corresponding projection

$$\mathcal{P}\Sigma = \{(0, u(t - a_1), u(t - a_2))\} \cong \{u(t - a_1), u(t - a_2)\} = \mathbb{R}^2. \quad (3.3)$$

This generalises an idea of Mackey and Glass [55], who were the first to project solutions of DDEs into finite dimensions by plotting values of  $u(t - \tau)$  against  $u(t)$  for a single delay DDE.

For simplicity, we refer to the projected Poincaré section also as  $\Sigma$  and, throughout, we consider the invariant objects of the local Poincaré map  $P_\Sigma$  defined for points with  $u(t) = 0$  and  $u'(t) < 0$  (to ensure that there is a unique intersection set for periodic orbits and tori). As was already mentioned, we refer to the respective intersection set in the  $(u(t - a_1), u(t - a_2))$ -plane as the Poincaré trace of the invariant object.

We remark that, when the DDE has a sufficient number  $d$  of independent variables (at least three), a convenient alternative projection from  $C$  to  $\mathbb{R}^d$  is obtained by projecting the function segment  $u_t \in C$  onto its head-point  $u_t(0) = u(t) \in \mathbb{R}^d$ . See [22, 47] for an example of this construction for a laser system with  $d = 3$ . However, this approach is not useful for visualising the dynamics of (1.3) because  $u_t$  is scalar.

Figure 6 illustrates the different projections and representations with the example of the quasi-periodic torus from Fig. 5(a). Figure 6(a) shows a different view of the torus in  $(u(t), u(t - a_1), u(t - a_2))$ -space together with the Poincaré trace in the local section  $\Sigma$ . This image is very similar to illustrations one finds in the literature of quasi-periodic tori of three-dimensional vector fields; in particular, the torus appears to be smooth and the intersection curve with  $\Sigma$  is a smooth simple closed curve. That we are in fact dealing with a scalar state-dependent DDE with an infinite dimensional phase space is illustrated in panels (b) and (c). Figure 6(b) shows the function segments  $u_t(\theta)$  corresponding to all the points of the Poincaré trace on  $\Sigma$  in the  $u(t - a_1), u(t - a_2)$ -plane in panel (a). That is, the functions segments for the points on the torus with  $u(t) = 0$  (or equivalently  $u_t(0) = 0$ ) and  $u'(t) < 0$ . Note that, because the section  $\Sigma$  is defined by the condition  $u(t) = 0$ , all these function segments are defined over the same fixed time interval  $[-a_2, 0] = [-6, 0]$ , and all end up at the same point  $u(0) = 0$ . Figure 6(c) shows a different representation of the function segments associated with the points of the Poincaré trace, with the function segments  $(u_{t-a_1}(\theta), u_{t-a_2}(\theta))$  illustrating the ‘history tails’ over the time interval  $[-6, 0]$  associated with the trace in (the two-dimensional projection of)  $\Sigma$ . Notice that in this representation the invariant torus appears as a cylinder that is swept out by the function segments in the corresponding orbit under the local Poincaré map  $P_\Sigma$ , with the Poincaré trace seen in the plane for  $\theta = 0$  in Fig. 6(c).

Figure 7 shows an example of a smooth invariant torus with 1:4 phase-locked dynamics on it. In panels (a)–(c) the torus is represented in the same manner as the quasi-periodic torus in Fig. 6. However, in contrast to Fig. 5(b) that only shows the locked stable periodic orbit on the torus, Fig. 7 also shows the unstable locked periodic orbit and its two-dimensional unstable manifold,

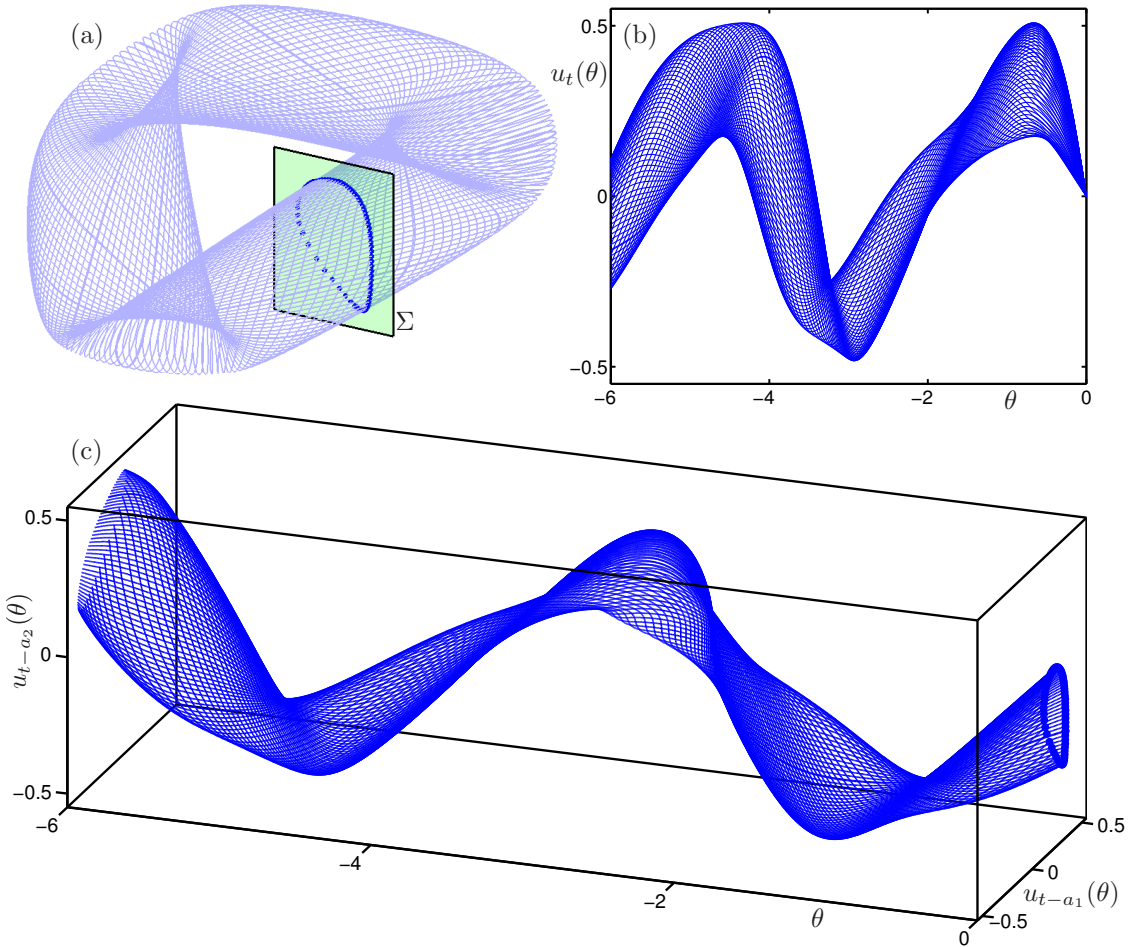


FIG. 6. Illustration of Poincaré section and trace for the quasi-periodic torus for  $\kappa_1 = 4.44$  and  $\kappa_2 = 3.0$  from Fig. 5(a). Panel (a) shows the projection onto  $(u(t), u(t - a_1), u(t - a_2))$ -space of a single solution of (1.3) on the torus (light blue), together with the trace (blue dots) on the (projected) section  $\Sigma$  (green); the corresponding function segments are shown in panel (b) as functions  $u_t$ , and in panel (c) as function segments  $(u_{t-a_1}(\theta), u_{t-a_2}(\theta))$ , over the delay interval  $\theta \in [-6, 0]$ , respectively. In panel (c) the Poincaré trace is seen in the plane for  $\theta = 0$ , which corresponds to  $\Sigma$ .

which together form the locked invariant torus itself. Fig. 7(a1) shows the torus rendered as a surface in  $(u(t), u(t - a_1), u(t - a_2))$ -space with the stable and unstable locked periodic orbits lying on it. Also shown is the section  $\Sigma$  and the Poincaré trace; for clarity, the trace is shown on its own in the  $(u(t - a_1), u(t - a_2))$ -plane in panel (a2). Associated segments  $u_t$  are shown as functions of  $\theta$  in Fig. 7(b), and in terms of  $(u_{t-a_1}(\theta), u_{t-a_2}(\theta))$  in Fig. 7(c).

The torus in Fig. 7 gives rise to a single smooth curve as the trace in the  $(u(t - a_1), u(t - a_2))$ -plane, on which lie four points of a stable period-four orbit and four points of an unstable period-four orbit; see Fig. 7(a2). The stable periodic orbit was found by numerical simulation. It was then used to start a continuation of the periodic orbit in the parameter  $\kappa_1$  which yielded, after a fold

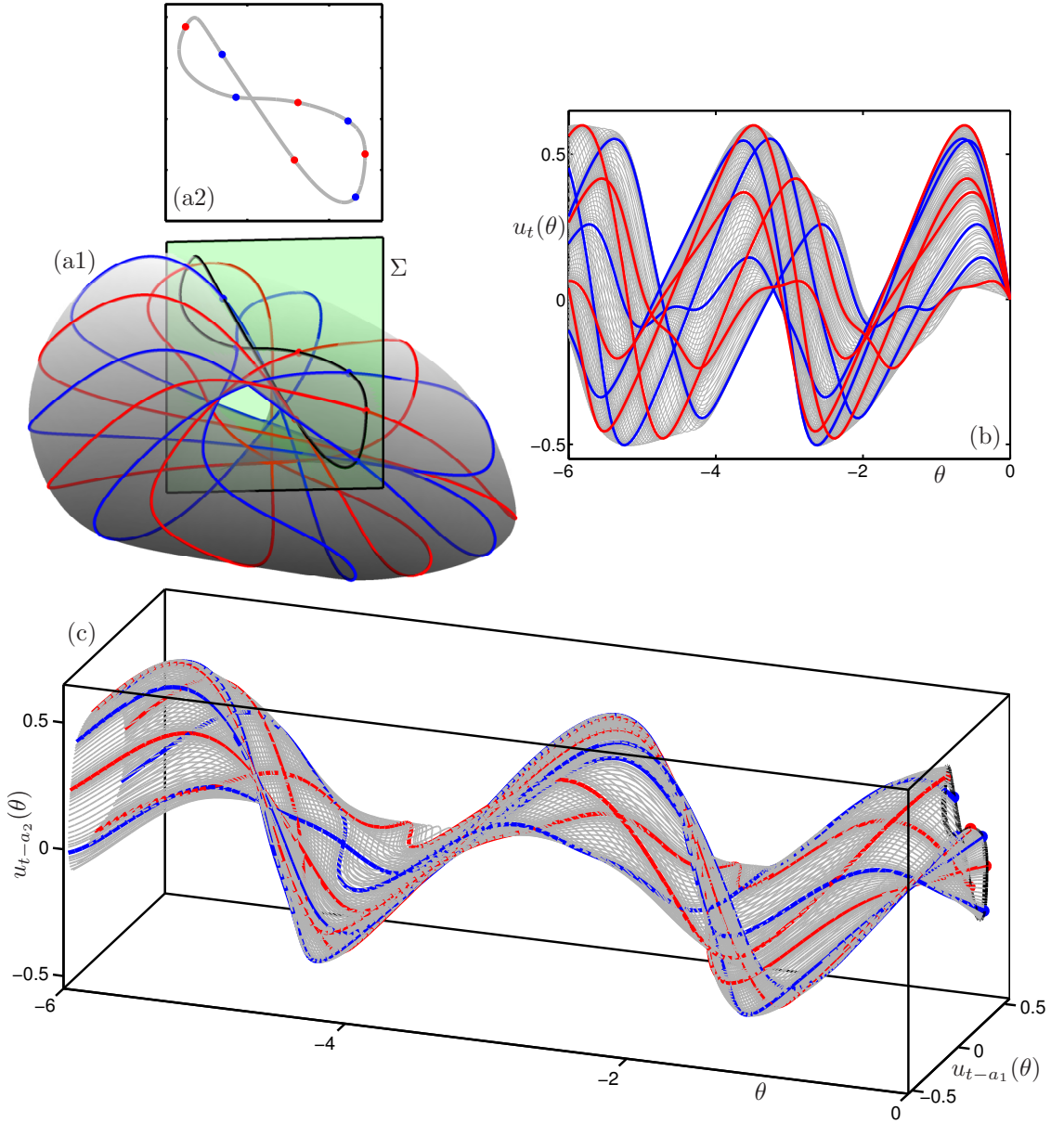


FIG. 7. Illustration of Poincaré section and trace for the 1:4 phase-locked torus for  $\kappa_1 = 5.405$  and  $\kappa_2 = 2.45$ . Panel (a1) shows the projection onto  $(u(t), u(t - a_1), u(t - a_2))$ -space of the relevant invariant objects, namely, of the stable periodic orbit (blue), the saddle periodic orbit (red), its unstable manifold (grey curve), together with the trace on the (projected) section  $\Sigma$  (green). Panel (a2) shows only the trace of these objects in  $\Sigma$ . The corresponding function segments are shown in panel (b) as functions  $u_t$ , and in panel (c) as function segments  $(u_{t-a_1}(\theta), u_{t-a_2}(\theta))$ , over the delay interval  $\theta \in [-6, 0]$ , respectively.

or saddle-node bifurcation of periodic orbits, the unstable periodic orbit. This calculation also confirmed that, as theory predicts, the unstable periodic orbit has exactly one unstable Floquet multiplier. We extracted the unstable eigenfunction associated with the unstable periodic orbit on the torus and used it to define two initial functions in the local unstable manifold of the periodic

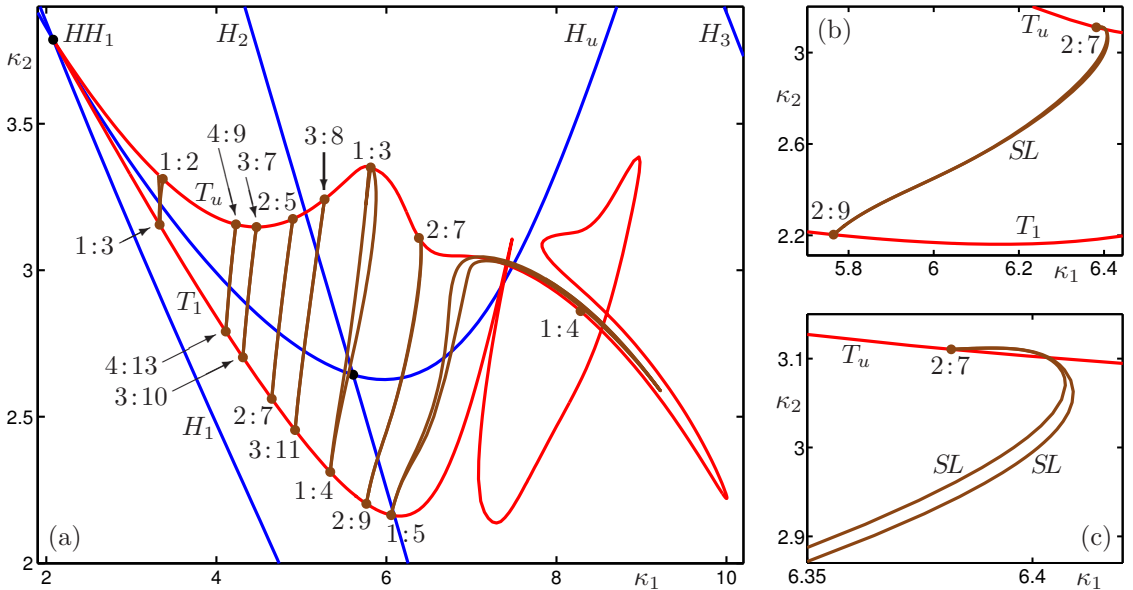


FIG. 8. The torus bifurcation curves  $T_u$  and  $T_l$  emerging from the Hopf-Hopf bifurcation point  $HH_1$  and associated resonance tongues in the  $(\kappa_1, \kappa_2)$ -plane (a). Panels (b) and (c) are successive enlargements of the resonance tongue that connects a  $2:7$  resonance on  $T_u$  with a  $2:9$  resonance on  $T_l$ .

orbit (one on each side of the orbit). Then numerical integration near the periodic point and along the unstable eigenfunction was used to compute trajectories that lie on the unstable manifold; associated orbit segments are shown in Fig. 7(b) and (c). Careful selection and ordering of orbit segments on the unstable manifolds (between intersections with the Poincaré section) allowed us to render the torus as a surface in  $(u(t), u(t - a_1), u(t - a_2))$ -space in Fig. 7(a1), and to draw the corresponding one-dimensional curve in the  $(u(t - a_1), u(t - a_2))$ -plane in Fig. 7(a2).

Again, the representation of locked dynamics on the torus in Fig. 7 is very reminiscent of what one would expect to find in a three-dimensional vector field. Notice, however, that — in contrast to the quasi-periodic torus in Fig. 6 — the invariant curve in the  $(u(t - a_1), u(t - a_2))$ -plane has a point of self-intersection. The torus in  $(u(t), u(t - a_1), u(t - a_2))$ -space also has a curve of self-intersection; see Fig. 7(c). This is due to projection from the infinite-dimensional phase space and a reminder that we are dealing with a DDE and not a low-dimensional dynamical system. While self-intersections may occur, we believe that the chosen Poincaré section  $\Sigma$  defined by  $u(t) = 0$  is the most convenient and natural choice for the study of multi-frequency dynamics in (1.3).

**3.1. Resonance tongues and locked tori.** Continuation of the two torus bifurcation curves that are known to emerge from the Hopf-Hopf point  $HH_1$  in the  $(\kappa_1, \kappa_2)$ -plane shows that the two local curves  $T_u$  and  $T_l$  are actually part of a single curve; it is shown in Fig. 8. Along the two local branches one finds many points of  $p:q$  resonance where the Floquet multiplier is a rational multiple of  $2\pi$ . They can be detected during the continuation of the torus bifurcation curve, and Fig. 8(a) shows such resonances for  $q \leq 13$ . Emerging from each point of  $p:q$  resonance are two curves of fold or saddle-node of periodic orbit bifurcations, which bound a resonance tongue or region where the dynamics on the torus is  $p:q$  locked. In Fig. 8(a) we find that the pair of saddle-node of periodic orbit bifurcation curves emerging from each  $p:q$  resonance point on the upper branch  $T_u$  can be continued to a  $p:(p+q)$  resonance point on the lower branch  $T_l$ . The enlargement in panel (b) shows this for the specific example of the  $2:7$  resonance on  $T_u$  and the  $2:9$  resonance on  $T_l$ ;

the further enlargement in Fig. 8(c) shows the narrow tip of the resonance tongue near the 2 : 7 resonance point.

Such ‘connected resonance tongues’ near a Hopf-Hopf bifurcation point are a curious phenomenon that has not been reported elsewhere to the best of our knowledge. Note that general theory (for ODEs and DDEs with fixed delays) states that the existence of smooth (normally hyperbolic) invariant tori — with locked dynamics in resonance tongues and quasi-periodic dynamics along curves in the  $(\kappa_1, \kappa_2)$ -plane — is guaranteed only locally near the curves  $T_u$  and  $T_1$ . Since, a  $p:q$  torus knot is topologically different from a  $p:(p+q)$  torus knot, the respective locked solutions near  $T_u$  and  $T_1$  cannot lie on one and the same smooth invariant torus. Nevertheless, a locked solution on a torus is simply a periodic orbit, and it may continue to exist even when the underlying torus disappears. When no longer constrained to lie on an invariant torus, a  $p:q$  periodic orbit can be transformed smoothly into a  $p:(p+q)$  periodic orbit, which explains why the saddle-node of periodic orbit bifurcation curves may connect the respective points on  $T_u$  and  $T_1$ . It is important to realise, however, that the regions that the pair of curves bound cannot contain smooth invariant tori throughout; some examples of non-smooth tori will be presented in Sec. 3.2. The questions of how the smooth tori near  $T_u$  and  $T_1$  break up and how the overall phenomenon is organised by the Hopf-Hopf bifurcation certainly merit further study, ideally in the setting of a four-dimensional ODE.

Near the points of resonances on  $T_u$  and  $T_1$  the respective locked dynamics must be expected to take place on a smooth invariant torus; indeed Fig. 7 is an example of such a smooth torus with locked dynamics. Fig. 9(a) shows an enlargement of the resonance tongue that connects a 1 : 3 resonance on  $T_u$  with a 1 : 4 resonance on  $T_1$ , and panel (b) shows the continuation of the corresponding locked periodic orbits for  $\kappa_2 = 3$ . There are three branches of stable and three branches of unstable periodic solution in Fig. 9(b), which meet at saddle-node bifurcations marking the left and right boundaries of this region of locking. Tori beyond the resonance region in panel (b) feature dynamics that is quasi-periodic or of very high period; they were found by parameter sweeping with numerical integration. Fig. 9(c) shows the invariant torus for  $\kappa_1 = 5.79$  (near the right boundary of the locking region) as a surface in  $(u(t), u(t - a_1), u(t - a_2))$ -space, and panel (d) is its trace for the Poincaré map defined by  $u(t) = 0$ . The torus was again found by computing the one-dimensional unstable manifolds of the saddle periodic orbits. As Fig. 9(c) and (d) indicate clearly, this invariant torus is 1 : 3 locked and smooth. The animation `chk.anim9.avi` in the supplemental materials shows the evolution of the Poincaré trace as the parameter  $\kappa_1$  is swept over the range shown in Fig. 9(b).

On the other hand, the saddle-node of periodic orbit bifurcation curves in Fig. 8(a) connect a  $p:q$  resonance point on  $T_u$  to a  $p:(p+q)$  resonance point on  $T_1$ . Hence, the torus inside the respective resonance tongue cannot be smooth throughout, because the knot type on a smooth invariant two-torus is an invariant. While a  $p:q$  periodic orbit can change smoothly into a  $p:(p+q)$  periodic orbit — as Fig. 8 shows — this cannot happen on one and the same smooth two-torus.

Fig. 10(a) shows an enlargement of the resonance tongue that connects a 1 : 4 resonance on  $T_u$  with a 1 : 5 resonance on  $T_1$ . The one-parameter bifurcation diagram for  $\kappa_2 = 3.0$  in Fig. 10(b) shows that one is dealing with 1 : 4 locking: there are four branches each of stable and unstable periodic orbits, which meet in saddle-node bifurcations at the boundary of the resonance tongue; the dynamics beyond the tongue is again quasi-periodic or of very high period. The situation looks exactly as that near the 1 : 3 resonance point in Fig. 9(b). However, as Fig. 10(c) and (d) show, there is no longer a smooth invariant torus. Rather, the one-dimensional unstable manifold of the saddle periodic orbit spirals around the stable periodic orbit; see panel (d). This means that the stable periodic orbit has developed a pair of complex conjugate leading Floquet multipliers, which is one mechanism for the loss of normal hyperbolicity of an invariant torus that is known from ODE theory [2]. Note that the loss of normal hyperbolicity is found numerically by two independent



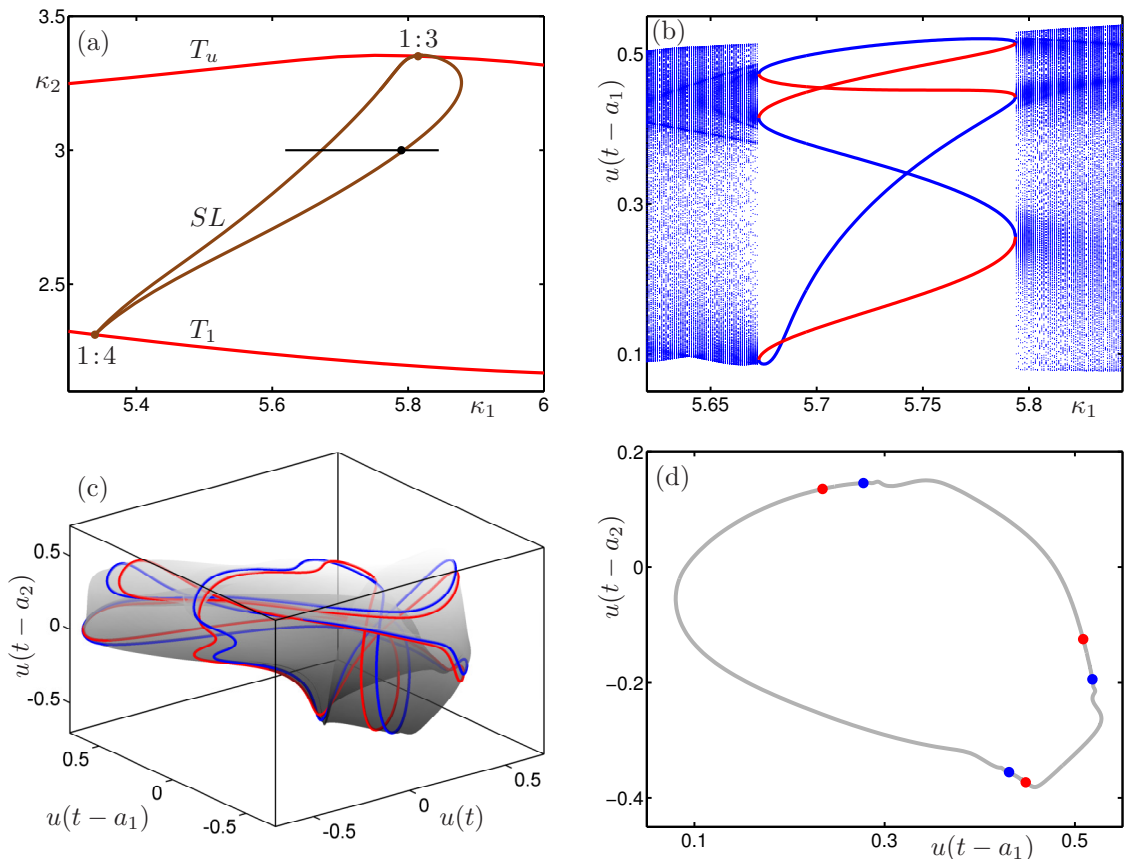


FIG. 9. The resonance tongue that connects a 1:3 resonance on  $T_u$  with a 1:4 resonance on  $T_l$ . Panel (a) shows this resonance tongue in the  $(\kappa_1, \kappa_2)$ -plane. Panel (b) is a one-parameter bifurcation diagram in  $\kappa_1$  for fixed  $\kappa_2 = 3.0$ , showing the values of  $u(t - a_1)$  of the Poincaré trace of the stable periodic orbit (blue) and of the saddle periodic orbit (red) inside the resonance tongue, and of other solutions on tori outside the resonance tongue. Panel (c) shows the 1:3 phase-locked torus (grey) for  $\kappa_1 = 5.79$  with the stable and saddle periodic orbits in projection onto  $(u(t), u(t - a_1), u(t - a_2))$ -space, and panel (d) is its Poincaré trace in the  $(u(t - a_1), u(t - a_2))$ -plane. The accompanying animation `chk_anim9.avi` shows the corresponding evolution of the Poincaré trace over the  $\kappa_1$ -range in panel (b).

computations. The manifold seen to spiral in panel (d) was computed by using the initial value problem solver `ddesd` and its event detection to compute a trajectory in the unstable manifold of the periodic orbit and its intersections with the Poincaré section, revealing the spiralling dynamics. But we also used DDE-BIFTOOL to directly compute the Floquet multipliers of the unstable periodic orbit, confirming that the two dominant multipliers are complex conjugate. The loss of normal hyperbolicity is very clearly seen in the animation `chk_anim10.avi` in the supplemental materials, which shows the evolution of the Poincaré trace in a one-parameter  $\kappa_1$ -sweep across the resonance tongue. Namely, stable periodic points on the Poincaré trace are denoted by stars in the animation when their dominant Floquet multipliers are complex conjugate; this happens across much of this traverse of the resonance tongue, and the unstable manifold of the saddle periodic orbit is then seen to spiral into the stable periodic points on the Poincaré trace.

**3.2. Break-up of 1:4 locked torus.** In the previous section we discussed the local transition for fixed  $\kappa_2 = 3$  through a 1:4 resonance as  $\kappa_1$  changes near  $\kappa_1 = 6.93$ . Notice in Fig. 10(a) that



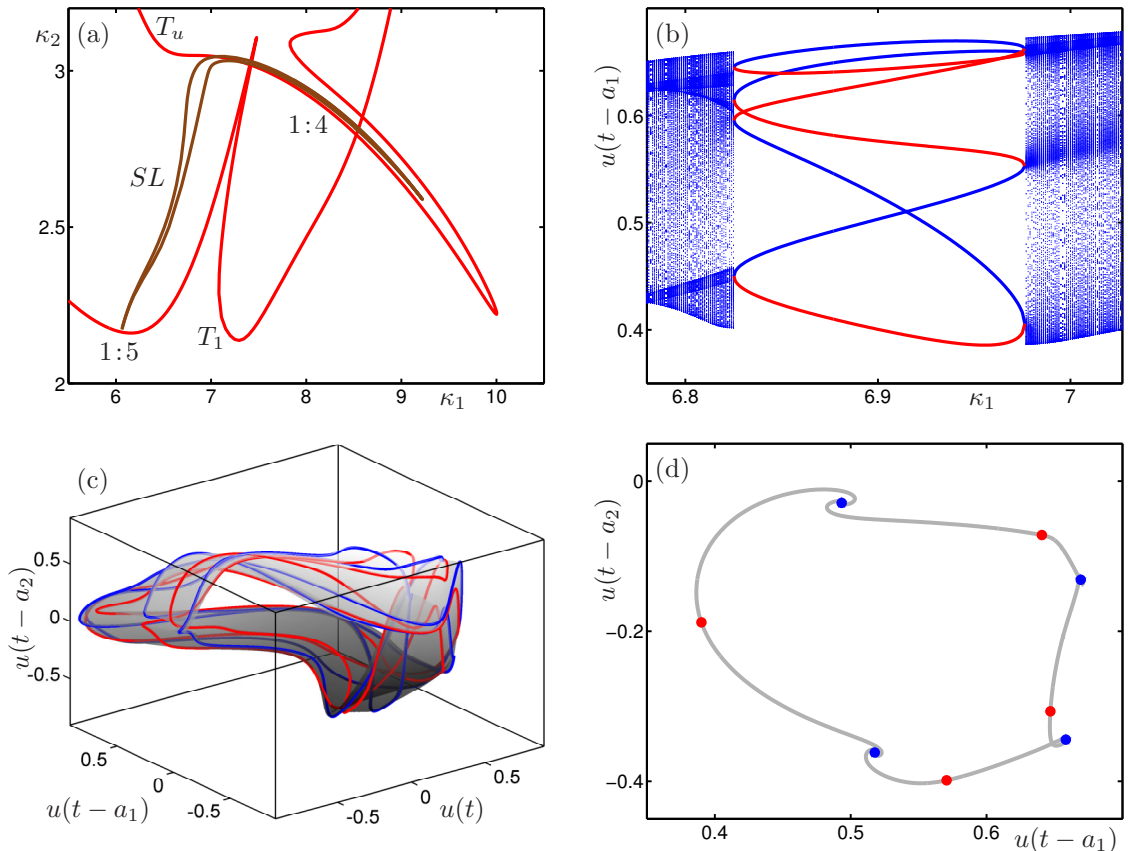


FIG. 10. The resonance tongue that connects a 1:4 resonance on  $T_u$  with a 1:5 resonance on  $T_1$ . Panel (a) shows this resonance tongue in the  $(\kappa_1, \kappa_2)$ -plane. Panel (b) is a one-parameter bifurcation diagram in  $\kappa_1$  for fixed  $\kappa_2 = 3.0$ , showing the values of  $u(t - a_1)$  of the Poincaré trace of the stable periodic orbit (blue) and of the saddle periodic orbit (red) inside the resonance tongue, and of other solutions on tori outside the resonance tongue. Panel (c) shows the 1:4 phase-locked torus-like object (grey) for  $\kappa_1 = 6.93$  with the stable and saddle periodic orbits in projection onto  $(u(t), u(t - a_1), u(t - a_2))$ -space, and panel (d) is its Poincaré trace in the  $(u(t - a_1), u(t - a_2))$ -plane. The accompanying animation `chk_anim10.avi` shows the corresponding evolution of the Poincaré trace over the  $\kappa_1$ -range in panel (b).

the associated resonance tongue in the  $(\kappa_1, \kappa_2)$ -plane has the shape of a horseshoe with maxima of the two bounding saddle-node curves at  $\kappa_1 \approx 7$ . Both of the two maxima occur for  $\kappa_2 > 3$ . Hence, for  $\kappa_2 = 3$  there is a range of  $\kappa_1$ -values outside this resonance tongue before it is entered again at  $\kappa_1 \approx 7.617$  when  $\kappa_1$  is increased further beyond the range shown in Fig. 10(b). As we will show now, the transition through this second part of the 1:4 resonance tongue results in the break-up and disappearance of the torus via a complicated scenario of bifurcations that involves nearly periodic orbits.

The sequence of bifurcations for fixed  $\kappa_2 = 3$  and the associated dynamics are illustrated by two companion figures. Figure 11 shows two one-parameter bifurcation diagrams in  $\kappa_1$ , and Fig. 12 shows the associated sequence of Poincaré traces in the  $u(t - a_1), u(t - a_2)$ -plane; see also the accompanying animation `chk_anim12.avi`, which animates the evolution of the Poincaré traces for  $\kappa_1 \in [7.530, 7.702]$ .

Starting at  $\kappa_1 = 7.5$ , there is an invariant torus with quasiperiodic or high-period solutions

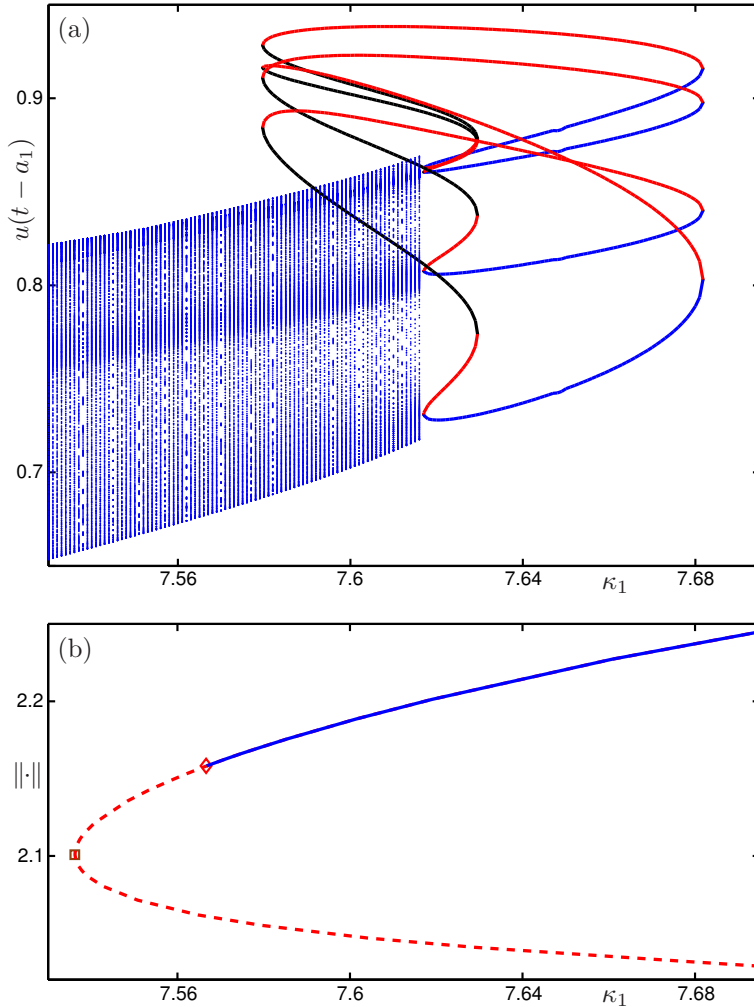


FIG. 11. One-parameter bifurcation diagrams relevant for the transition through the 1:4 resonance. Panel (a) shows the values of  $u(t - a_1)$  of the Poincaré trace of solutions on tori outside the resonance tongue and of period-four periodic orbits that are stable (blue), have one unstable Floquet multiplier (red), or have two unstable Floquet multipliers (black). Panel (b) shows the simultaneously existing pair of principal periodic orbits that are born in a saddle-node bifurcation, and one of which is stable (blue) past the torus bifurcation (diamond).

on it; see Fig. 11(a). As  $\kappa_1$  is increased, the first bifurcation of interest is the creation of two saddle periodic orbits at a saddle-node bifurcation of periodic orbits at  $\kappa_1 \approx 7.5363$ . We refer to them as the principal periodic orbits because their branch can actually be traced back to first Hopf bifurcation  $H_1$ ; see Fig. 1. As is shown in Fig. 11(b), at  $\kappa_1 \approx 7.5664$  one of the two saddle periodic orbits gains stability in a torus bifurcation when the branch of periodic orbits crosses the torus curve  $T_u$ . This torus bifurcation is close to 1 : 4 resonance, with numerically computed Floquet multipliers  $\rho \approx -0.019 \pm 1.000073i$  very close to  $\pm i$ . There is then an interval of  $\kappa_1$ -values for which the stable periodic orbit on the principal branch and the stable quasi-periodic torus co-exist; see Fig. 11(a). The associated invariant closed curve in the  $u(t - a_1), u(t - a_2)$ -plane is shown in Fig. 12(a), together with the two points that represent the stable and saddle principal periodic orbits in the Poincaré trace.

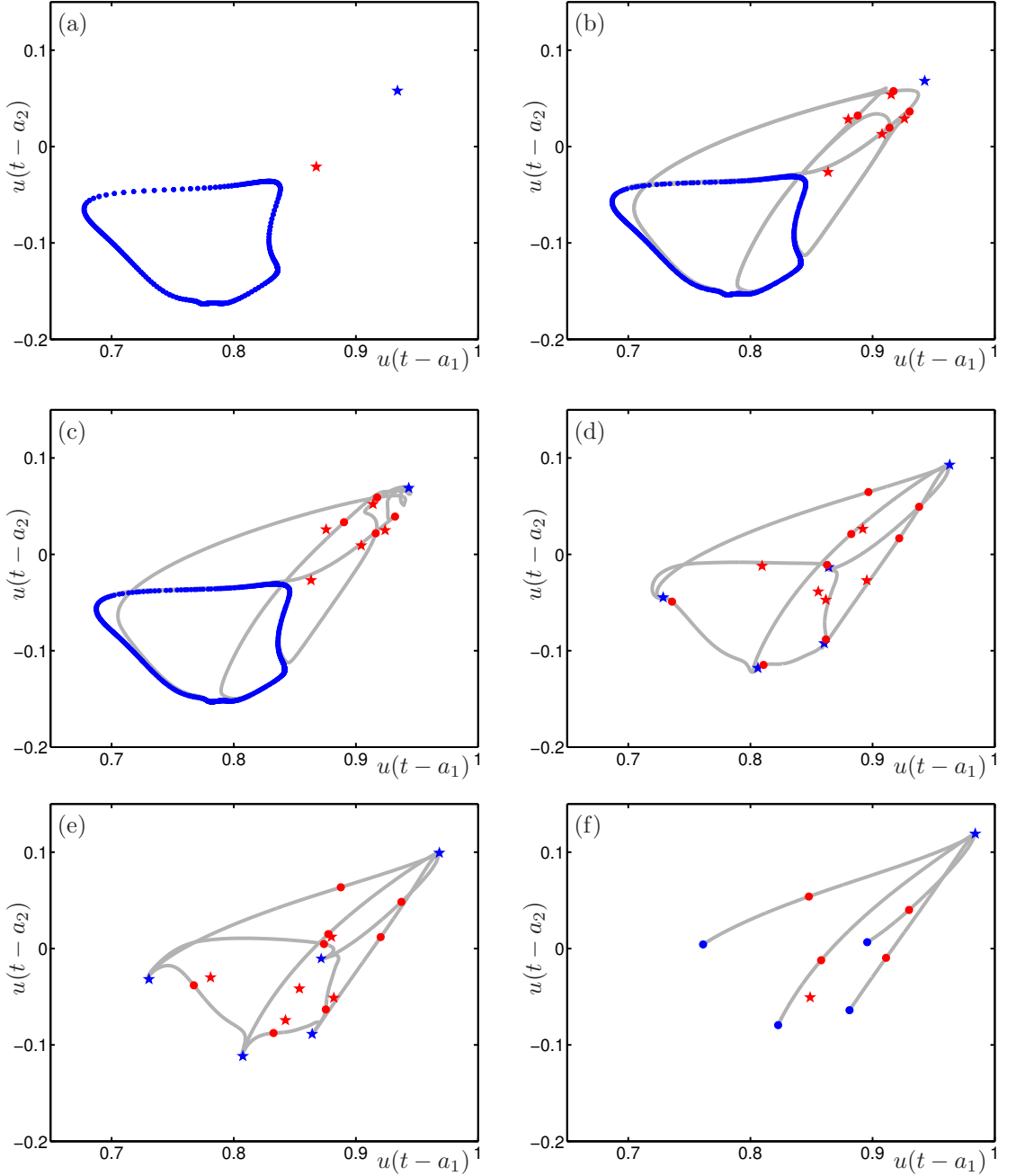


FIG. 12. Sequence of Poincaré traces in the  $(u(t-a_1), u(t-a_2))$ -plane showing the break-up of a torus with 1:4 phase locking. Shown are invariant curves (bold blue dots), stable periodic points (blue stars) and saddle periodic points with two unstable Floquet multipliers (red stars) and with a single unstable Floquet multiplier (red dots); also shown are the traces of the unstable manifolds (grey curves) of the latter saddle points. Here  $\kappa_2 = 3$  and in panels (a)–(f)  $\kappa_1$  takes the values 7.567, 7.58, 7.581, 7.618, 7.629, and 7.666, respectively. See also the accompanying animation *chk\_anim12.avi*.

At  $\kappa_1 \approx 7.5796$  another saddle-node bifurcation of periodic orbits creates a pair of period-four orbits, one of which has exactly one and the other two unstable Floquet multipliers; see Fig. 11(a). In the Poincaré trace in Fig. 12(b), for  $\kappa_1 = 7.58$ , these are represented by two sets of period-four points. Also shown is the one-dimensional trace of the unstable manifold of the saddle periodic orbit with one unstable Floquet multiplier; note that both its branches (on either side of the respective periodic point) converge to the attracting invariant curve. Almost immediately afterwards, for  $7.58 < \kappa_1 < 7.581$ , there is a bifurcation that changes the nature of the unstable manifold of the saddle period-four orbit. As Fig. 12(c) shows, one branch now goes to the attracting principle periodic orbit (blue star), while the other branch still goes to the attracting invariant curve. This means that, on the level of the Poincaré trace, we are dealing with a global bifurcation that is described in the approximating normal form of a 1:4 resonance as a saddle connection of square type [44, 45].

At  $\kappa_1 \approx 7.617$  the 1:4 resonance tongue is re-entered and we find two locked period-four orbits on the torus, one of which is attracting and the other has a single unstable Floquet multiplier. In the trace in Fig. 12(d) they are shown as a further two sets of period-four points. Also shown is the trace of the unstable manifold of the saddle four-periodic orbit on the torus, both branches of which end up at neighboring period-four attracting points to form a smooth invariant curve. Hence, the torus is still normally hyperbolic (that is, smooth) as is expected near the boundary of a resonance tongue. Notice that the respective branch of the unstable manifold of each saddle period-four point off the invariant curve now also goes to the attracting periodic orbit on the torus.

As  $\kappa_1$  is increased further, the torus loses normal hyperbolicity. More specifically, the branches of all unstable manifolds shown in Fig. 12(e) approach the attracting period-four orbit along the same side of its weak stable eigen-direction, so that a cusp is formed along the attracting period-four orbit. Moreover, the period-four orbit with two unstable Floquet multipliers, created at  $\kappa_1 \approx 7.5796$  and not mentioned since, now enters the action. As  $\kappa_1$  increases, this saddle periodic orbit approaches the saddle periodic orbit on the torus, which has a single unstable Floquet multiplier. At  $\kappa_1 \approx 7.6295$ , the two period-four orbits annihilate each other in a further saddle-node bifurcation; see Fig. 11(a). The periodic points and the associated unstable manifold disappears at this value of  $\kappa_1$ . Hence, as Fig. 12(f) illustrates, we are left with the two remaining period-four orbits: the attracting one and other saddle periodic orbit. Notice that the unstable manifold of the latter does not change in this process, meaning that one branch of each period-four point in the trace still ends up at the principal periodic orbit, and the other at the respective attracting period-four point. As  $\kappa_1$  is increased even further, the two period-four orbits approach each other and finally disappear in the last saddle-node bifurcation at  $\kappa_1 \approx 7.6818$  in Fig. 11(a). Hence, we are left with only the stable and saddle principal periodic orbits; see Fig. 11(b).

Overall, the torus loses normal hyperbolicity and then breaks up and disappears completely. In particular, unlike for the cases studied in Sec. 3.1, the torus does not re-emerge on the other side of the 1:4 resonance tongue.

**4. Overall bifurcation diagram and conclusions.** Our study of the scalar state-dependent DDE (1.3) concentrated on the dynamics associated with the presence of codimension-two Hopf-Hopf bifurcation points. We presented a normal form procedure for state-dependent DDEs that, by eliminating the state dependence up to order three, allowed us to determine the type of Hopf-Hopf bifurcation from the resulting DDE with nine constant delays. In this way, we showed that a pair of torus bifurcation curves emerges locally from each of the three Hopf-Hopf bifurcation points in the region of interest of the  $(\kappa_1, \kappa_2)$ -plane of (1.3). Our normal form computations have been confirmed by finding and continuing these torus bifurcation curves numerically with the package DDE-BIFTOOL. What is more, numerical continuation allowed us to follow the torus bifurcation curves beyond the local neighborhoods of the Hopf-Hopf bifurcation points, and to identify the structure of resonance tongues emerging from them. We computed locked periodic

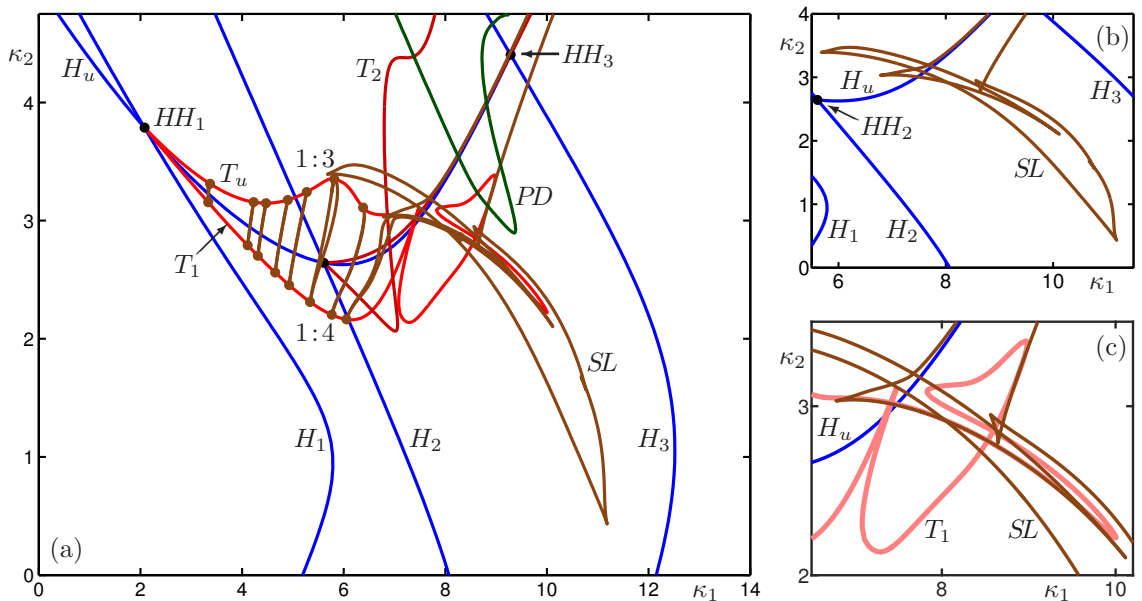


FIG. 13. Overall bifurcation diagram of (1.3) in the  $(\kappa_1, \kappa_2)$ -plane (a), showing curves of Hopf bifurcation (blue) of torus bifurcation (red), of saddle-node of limit cycle bifurcation (brown) and of period-doubling bifurcation (green). Panel (b) is an enlargement near  $HH_2$ , and panel (c) shows details of the saddle-node of limit cycle bifurcation curve  $SL$  that is not connected to a resonance point on a torus.

orbits on the tori and determined the boundaries of resonance tongues by continuing their saddle-node bifurcations. The tori and the dynamics on them was investigated and visualised by suitable projections into three-dimensional space, as well as by their two-dimensional Poincaré traces. In particular, we computed the unstable manifolds of saddle-periodic orbits with a single unstable Floquet multiplier, which allowed us to study in considerable detail how invariant tori break up and disappear, for example near a  $1:4$  resonance.

The starting point of our investigation was the one-parameter bifurcation diagram Fig. 1 from [34]. Specifically, we used it to start continuations of periodic solutions and of bifurcation curves in the  $(\kappa_1, \kappa_2)$ -plane, namely, the curves of Hopf bifurcation in Fig. 3, as well as the curves of torus bifurcation and saddle-node bifurcation that bound certain resonance tongues in Fig. 8(a). Returning to Fig. 1, one can identify two additional bifurcations that we did not consider yet in our study of resonance phenomena: a period-doubling bifurcation and an additional saddle-node bifurcation of limit cycles. Figure 13 shows the overall two-parameter bifurcation diagram of (1.3) in the  $(\kappa_1, \kappa_2)$ -plane with all the above bifurcation curves. Panel (a) shows the relevant region where  $0 \leq \kappa_1 \leq 14$  and  $0 \leq \kappa_2 \leq 4.75$ . In particular, shown are the three pairs of torus bifurcation curves emerging from the Hopf-Hopf bifurcation points  $HH_1$  to  $HH_3$ . Notice that the two torus bifurcation curves emerging from  $HH_3$  stay very close to the Hopf bifurcation curve  $H_u$ ; similarly, the torus bifurcation curve  $T_u$  emerging from  $HH_2$  stays close to  $H_u$ , while the other curve  $T_2$  exits the top of the  $(\kappa_1, \kappa_2)$ -plane. Prominent in panel (a) is the curve  $PD$  of period-doubling bifurcation, which has a minimum near  $(\kappa_1, \kappa_2) \approx (10, 3)$ . As Fig. 1(a) shows, the periodic orbit undergoing the period-doubling bifurcation has a large amplitude.

The other new curve in Fig. 13 is the saddle-node of limit cycle bifurcation curve labelled  $SL$ . It enters and exits the top of the  $(\kappa_1, \kappa_2)$ -plane near and in the direction of the Hopf bifurcation curve  $H_u$ . As panel (b) shows, the curve  $SL$  is very complicated and features eight cusps (two pairs of

which are actually very close to swallowtail bifurcations), resulting in quite a number of regions with different numbers of bifurcating periodic orbits. From Sec. 3.2 it is clear that some periodic orbits emerging from saddle node bifurcations play an important role in the torus break-up mechanism. At the same time, the overall bifurcation diagram in Fig. 13 shows with the example of  $SL$  that there are other saddle node bifurcations that may not immediately be related to the torus bifurcations emerging from  $HH_1$  to  $HH_3$ . However,  $SL$  comes very close to several torus bifurcation curves; see Fig. 13(c). Moreover, it follows closely the horseshoe-shaped resonance region (discussed in Sec. 3.2) that connects the 1:4 resonance on  $T_u$  with the 1:5 resonance in  $T_1$ . We remark that the curve  $SL$  traverses the  $(\kappa_1, \kappa_2)$ -plane several times close to the line  $\kappa_1 + \kappa_2 = \gamma(a_2/a_1 - 2) \approx 12.4$  where the singular fold bifurcation  $L_{00}$  occurs in the  $\varepsilon \rightarrow 0$  singular limit of (1.3); see [33]. Moreover,  $SL$  extends to very low values of  $\kappa_2$ ; in fact, in one-parameter bifurcation diagrams in  $\kappa_1$  for fixed  $\kappa_2$ , it generates the first observed folds in the branch of periodic orbits that bifurcate from the Hopf bifurcation  $H_1$  as  $\kappa_2$  is increased; see [34].

Figure 13 can be seen as a summary and overview of the level of complexity of the dynamics one can find in (1.3). In a sense, the overall bifurcation diagram in the  $(\kappa_1, \kappa_2)$ -plane of the two feedback strengths would not be particularly unusual for a nonlinear DDE. Its surprising aspect is, however, that all phenomena it represents are entirely due to the state dependence. As the state-dependence parameters  $c_1$  and  $c_2$  of the delays are decreased to zero, the bifurcation structure in Fig. 13, including the Hopf-Hopf bifurcation points and induced dynamics on tori, will disappear. Indeed, (1.3) for  $c_1 = c_2 = 0$  is entirely linear and, hence, does not have any nontrivial dynamics. Hence, if one were to replace the state-dependence by constant delays, none of the dynamics we reported would be found. Admittedly, equation (1.3) has been constructed as an extreme case in this regard. Nevertheless, the study presented here should be seen as a health warning: replacing state dependence by a constant-delay approximation may result in the disappearance of the very dynamics one intends to study. This may be the case even when the approximating constant-delay DDE is actually nonlinear itself.

State-dependent DDEs have been suggested as suitable models in a number of applications [10, 36, 38, 68, 82]. We hope that the study presented here may serve as a demonstration of what can be achieved by a combination of analytical and numerical tools when it comes to the bifurcation analysis of a given state-dependent DDE. It is now possible to study models from this class effectively in their own right, and to determine the role the state dependence plays in the observed dynamics. In fact, normal form calculations and numerical continuation tools are able to produce consistent results, such as the type of codimension-two bifurcation or the existence and organisation of resonances on tori, for which, as yet, the respective theory has not yet been developed for state-dependent DDEs. We believe that case studies of specific systems are also a useful way of guiding the further development of theory for state-dependent DDEs. At the same time, numerical methods also continue to be developed further. For example, the curves shown in Fig. 13 were computed with recently implemented routines of DDE-BIFTOOL [72] that allow the continuation in two parameters of codimension-one bifurcation of periodic orbits to determine curves of saddle-node, period-doubling and torus bifurcations. Previously, such curves could only be constructed by detecting the respective bifurcation in one-parameter continuations, which is certainly not a suitable method for finding complicated bifurcation curves such as  $SL$  in Fig. 13(b). In a nutshell, practically all advanced tools for the bifurcation analysis of DDEs are now also available when state dependence is present.

**Acknowledgements.** A.R.H. is grateful to the National Science and Engineering Research Council (NSERC), Canada for funding through the Discovery Grant program, and thanks the University of Auckland for its hospitality and support during two research visits. R.C.C. thanks the Department of Mathematics and Statistics at McGill for their hospitality during his time as a Postdoctoral Fellow and now as an Adjunct Member of the department. He is also grateful to

NSERC and the Centre de Recherches Mathématiques for funding and to the FQRNT for a PBEER award. We thank Jan Sieber for fruitful discussions regarding normal form calculation within DDE-BIFTOOL, Rafael de la Llave and Xiaolong He for helpful comments on quasiperiodic solutions in state-dependent DDEs, and two anonymous referees for their very constructive feedback on the initial version of the manuscript.

## REFERENCES

- [1] W. G. Aiello, H. I. Freedman, and J. Wu. Analysis of a model representing stage-structured population growth with state-dependent time delay. *SIAM J. Appl. Math.*, 52(3):855–869, 1992.
- [2] D. G. Aronson, M. A. Chory, G. R. Hall, and R. P. McGehee. Bifurcations from an invariant circle for two-parameter families of maps of the plane: A computer-assisted study. *Commun. Math. Phys.*, 83(3):303–354, 1982.
- [3] J. Bélair and S. A. Campbell. Stability and bifurcations of equilibria in a multiple-delayed differential equation. *SIAM J. Appl. Math.*, 54(5):1402–1424, 1994.
- [4] A. Bellen and M. Zennaro. *Numerical Methods for Delay Differential Equations*. Numerical Mathematics and Scientific Computation. Oxford Science Publications, New York, 2003.
- [5] A. Bellen, M. Zennaro, S. Maset, and N. Guglielmi. Recent trends in the numerical solution of retarded functional differential equations. *Acta Numer.*, 18:1–110, 2009.
- [6] R. E. Bellman and K. L. Cooke. *Differential-Difference Equations*. Academic Press, New York, 1963.
- [7] D. Breda, O. Diekmann, M. Gyllenberg, F. Scarabel, and R. Vermiglio. Pseudospectral discretization of nonlinear delay equations: new prospects for numerical bifurcation analysis. *SIAM J. Appl. Dyn. Syst.*, 15(1):1–23, 2016.
- [8] G. Brown, C. M. Postlethwaite, and M. Silber. Time-delayed feedback control of unstable periodic orbits near a subcritical Hopf bifurcation. *Physica D*, 240(910):859 – 871, 2011.
- [9] M. Craig, A. R. Humphries, and M. C. Mackey. A mathematical model of granulopoiesis incorporating the negative feedback dynamics and kinetics of G-CSF/neutrophil binding and internalization. *Bull. Math. Biol.*, 78(12):2304–2357, 2016.
- [10] J. De Luca, N. Guglielmi, A. R. Humphries, and A. Politi. Electromagnetic two-body problem: recurrent dynamics in the presence of state-dependent delay. *J. Phys. A*, 43(20):205103, 2010.
- [11] O. Diekmann, M. Gyllenberg, J. A. J. Metz, S. Nakaoka, and A. M. de Roos. Daphnia revisited: local stability and bifurcation theory for physiologically structured population models explained by way of an example. *J. Math. Biol.*, 61(2):277–318, 2010.
- [12] O. Diekmann, S. A. van Gils, S. M. Verduyn Lunel, and H.-O. Walther. *Delay Equations Functional-, Complex-, and Nonlinear Analysis*, volume 110 of *Applied Mathematical Sciences*. Springer-Verlag, 1995.
- [13] H. A. Dijkstra. *Dynamical Oceanography*. Springer-Verlag, 2008.
- [14] R. D. Driver. Existence theory for a delay-differential system. *Contrib. Diff. Eq.*, 1:317–336, 1963.
- [15] R. D. Driver. *Ordinary and Delay Differential Equations*, volume 20 of *Applied Mathematical Sciences*. Springer-Verlag, 1977.
- [16] M. Eichmann. *A local Hopf bifurcation theorem for differential equations with state-dependent delays*. PhD thesis, Universität Gießen, Germany, 2006.
- [17] K. Engelborghs, T. Luzyanina, and D. Roose. Numerical bifurcation analysis of delay differential equations using DDE-BIFTOOL. *ACM Trans. Math. Software*, 28(1):1–21, 2002.
- [18] G. Fan, S. A. Campbell, G. S. Wolkowicz, and H. Zhu. The bifurcation study of 1:2 resonance in a delayed system of two coupled neurons. *J. Dyn. Diff. Equat.*, 25(1):193–216, 2013.
- [19] B. Fiedler, V. Flunkert, M. Georgi, P. Hövel, and E. Schöll. Refuting the odd-number limitation of time-delayed feedback control. *Phys. Rev. Lett.*, 98:114101, 2007.
- [20] J. Foss, A. Longtin, B. Mensour, and J. Milton. Multistability and delayed recurrent loops. *Phys. Rev. Lett.*, 76:708–711, 1996.
- [21] P. Getto and M. Waurick. A differential equation with state-dependent delay from cell population biology. *J. Differential Equations*, 260(7):6176–6200, 2016.
- [22] K. Green, B. Krauskopf, and K. Engelborghs. Bistability and torus break-up in a semiconductor laser with phase-conjugate feedback. *Physica D*, 173(12):114 – 129, 2002.
- [23] S. Guo and J. Wu. *Bifurcation Theory of Functional Differential Equations*, volume 184 of *Applied Mathematical Sciences*. Springer-Verlag, New York, 2013.
- [24] I. Györi and F. Hartung. On the exponential stability of a state-dependent delay equation. *Acta Sci. Math. (Szeged)*, 66:71–84, 2000.
- [25] I. Györi and F. Hartung. Exponential stability of a state-dependent delay system. *Discrete Contin. Dyn. Syst. Ser. A*, 18(4):773–791, 2007.
- [26] J. K. Hale. *Theory of Functional Differential Equations*, volume 3 of *Applied Mathematical Sciences*. Springer-



Verlag, New York, 1977.

- [27] J. K. Hale and S. M. Verduyn Lunel. *Introduction to functional-differential equations*, volume 99 of *Applied Mathematical Sciences*. Springer-Verlag, New York, 1993.
- [28] F. Hartung. Nonlinear variation of constants formula for differential equations with state-dependent delays. *J. Dyn. Diff. Equat.*, 28(3-4):1187–1213, 2016.
- [29] F. Hartung, T. Krisztin, H.-O. Walther, and J. Wu. Functional differential equations with state-dependent delays: theory and applications. In A. Cañada, P. Drábek, and A. Fonda, editors, *Handbook of Differential Equations: Ordinary Differential Equations*, volume 3, pages 435–545. Elsevier - North-Holland, 2006.
- [30] X. He and R. de la Llave. Construction of quasi-periodic solutions of state-dependent delay differential equations by the parameterization method I: finitely differentiable, hyperbolic case. *J. Dyn. Diff. Equat.*, 2016.
- [31] X. He and R. de la Llave. Construction of quasi-periodic solutions of state-dependent delay differential equations by the parameterization method II: Analytic case. *J. Differential Equations*, 261:2068–2108, 2016.
- [32] Q. Hu and J. Wu. Global Hopf bifurcation for differential equations with state-dependent delay. *J. Differential Equations*, 248(12):2801 – 2840, 2010.
- [33] A. R. Humphries, D. A. Bernucci, R. Calleja, N. Homayounfar, and M. Snarski. Periodic solutions of a singularly perturbed delay differential equation with two state-dependent delays. *J. Dyn. Diff. Equat.*, 28(3):1215–1263, 2016.
- [34] A. R. Humphries, O. A. DeMasi, F. M. G. Magpantay, and F. Upham. Dynamics of a delay differential equation with multiple state-dependent delays. *Discrete Contin. Dyn. Syst. Ser. A*, 32(8):2701–2727, 2012.
- [35] T. Insperger, J. Milton, and G. Stépán. Acceleration feedback improves balancing against reflex delay. *J. Roy. Soc. Interface*, 10(79), 2012.
- [36] T. Insperger, G. Stépán, and J. Turi. State-dependent delay in regenerative turning processes. *Nonlinear Dyn.*, 47:275–283, 2007.
- [37] S. G. Janssens. On a normalization technique for codimension two bifurcations of equilibria of delay differential equations. Master’s thesis, Universiteit Utrecht, Holland, 2010.
- [38] R. Jessop and S. A. Campbell. Approximating the stability region of a neural network with a general distribution of delays. *Neural Netw.*, 23(10):1187 – 1201, 2010.
- [39] W. Just, B. Fiedler, M. Georgi, V. Flunkert, P. Hövel, and E. Schöll. Beyond the odd number limitation: A bifurcation analysis of time-delayed feedback control. *Phys. Rev. E*, 76:026210, Aug 2007.
- [40] D. M. Kane and K. A. Shore, editors. *Unlocking Dynamical Diversity: Optical Feedback Effects on Semiconductor Lasers*. Wiley, 2005.
- [41] H. Kaper and H. Engler. *Mathematics and climate*. Society for Industrial and Applied Mathematics, 2013.
- [42] M. Kloosterman, S. A. Campbell, and F. J. Poulin. A closed NPZ model with delayed nutrient recycling. *J. Math. Biol.*, 68(4):815–850, 2014.
- [43] G. Kozyreff and T. Erneux. Singular Hopf bifurcation in a differential equation with large state-dependent delay. *Proc. R. Soc. A*, 470:0596, 2013.
- [44] B. Krauskopf. Bifurcation sequences at 1:4 resonance: an inventory. *Nonlinearity*, 7:1073–1091, 1994.
- [45] B. Krauskopf. The bifurcation set for the 1:4 resonance problem. *Exp. Math.*, 3:107–128, 1994.
- [46] B. Krauskopf and D. D. Lenstra, editors. *Fundamental Issues of Nonlinear Laser Dynamics*, volume 548 of *AIP Conference Proceedings*. Ametican Institute of Physics, 2000.
- [47] B. Krauskopf and K. Green. Computing unstable manifolds of periodic orbits in delay differential equations. *J. Comput. Math.*, 186(1):230 – 249, 2003.
- [48] B. Krauskopf and J. Sieber. Bifurcation analysis of delay-induced resonances of the El-Niño southern oscillation. *Proc. R. Soc. A*, 470(2169), 2014.
- [49] T. Krisztin. A local unstable manifold for differential equations with state-dependent delay. *Discrete Contin. Dyn. Syst. Ser. A*, 9:993–1028, 2003.
- [50] T. Krisztin.  $C^1$ -smoothness of center manifolds for differential equations with state-dependent delay. In X.-Q. Z. Hermann Brunner and X. Zou, editors, *Nonlinear dynamics and evolution equations*, volume 48 of *Fields Inst. Commun.*, pages 213–226. Amer. Math. Soc., Providence, RI, 2006.
- [51] Y. A. Kuznetsov. *Elements of applied bifurcation theory*, volume 112 of *Applied Mathematical Sciences*. Springer-Verlag, New York, third edition, 2004.
- [52] Y. N. Kyrchko, K. B. Blyuss, and E. Schöll. Amplitude and phase dynamics in oscillators with distributed-delay coupling. *Phil. Trans. R. Soc. A*, 371(1999), 2013.
- [53] V. G. LeBlanc. Realizability of the normal form for the triple-zero nilpotency in a class of delayed nonlinear oscillators. *J. Differential Equations*, 254(2):637 – 647, 2013.
- [54] K. Lüdge, editor. *Nonlinear Laser Dynamics. From Quantum Dots to Cryptography*. Wiley-VCH, 2012.
- [55] M. C. Mackey and L. Glass. Oscillation and chaos in physiological control systems. *Science*, 197(4300):287–289, 1977.
- [56] J. Mallet-Paret and R. D. Nussbaum. Boundary layer phenomena for differential-delay equations with state-dependent time lags. I. *Arch. Rational Mech. Anal.*, 120:99–146, 1992.
- [57] J. Mallet-Paret and R. D. Nussbaum. Boundary layer phenomena for differential-delay equations with state-dependent time lags: II. *J. Reine Angew. Math.*, 477:129–197, 1996.

- [58] J. Mallet-Paret and R. D. Nussbaum. Boundary layer phenomena for differential-delay equations with state-dependent time lags: III. *J. Differential Equations*, 189:640–692, 2003.
- [59] J. Mallet-Paret and R. D. Nussbaum. Stability of periodic solutions of state-dependent delay-differential equations. *J. Differential Equations*, 250:4085–4103, 2011.
- [60] J. Mallet-Paret and R. D. Nussbaum. Superstability and rigorous asymptotics in singularly perturbed state-dependent delay-differential equations. *J. Differential Equations*, 250:4037–4084, 2011.
- [61] J. Mallet-Paret and R. D. Nussbaum. Periodic solutions of differential equations with two state-dependent delays. 2017. In preparation.
- [62] J. Mallet-Paret, R. D. Nussbaum, and P. Paraskevopoulos. Periodic solutions for functional differential equations with multiple state-dependent time lags. *Topol. Methods Nonlinear Anal.*, 3:101–162, 1994.
- [63] Mathworks. *MATLAB 2015b*. Mathworks, Natick, Massachusetts, 2015.
- [64] J. Milton, J. L. Townsend, M. A. King, and T. Ohira. Balancing with positive feedback: the case for discontinuous control. *Phil. Trans. R. Soc. A*, 367(1891):1181–1193, 2009.
- [65] C. M. Postlethwaite. Stabilization of long-period periodic orbits using time-delayed feedback control. *SIAM J. Appl. Dyn. Syst.*, 8(1):21–39, 2009.
- [66] A. S. Purewal, C. M. Postlethwaite, and B. Krauskopf. A global bifurcation analysis of the subcritical Hopf normal form subject to Pyragas time-delayed feedback control. *SIAM J. Appl. Dyn. Syst.*, 13(4):1879–1915, 2014.
- [67] K. Pyragas. Continuous control of chaos by self-controlling feedback. *Phys. Lett. A*, 170(6):421 – 428, 1992.
- [68] V. Pyragas and K. Pyragas. Adaptive modification of the delayed feedback control algorithm with a continuously varying time delay. *Phys. Lett. A*, 375(44):3866 – 3871, 2011.
- [69] R. Qesmi and H.-O. Walther. Center-stable manifolds for differential equations with state-dependent delays. *Discrete Contin. Dyn. Syst. Ser. A*, 23(3):1009–1033, 2009.
- [70] E. Schöll, G. Hiller, P. Hövel, and M. A. Dahlem. Time-delayed feedback in neurosystems. *Phil. Trans. R. Soc. A*, 367(1891):1079–1096, 2009.
- [71] J. Sieber. Finding periodic orbits in state-dependent delay differential equations as roots of algebraic equations. *Discrete Contin. Dyn. Syst. Ser. A*, 32(8):2607–2651, 2012.
- [72] J. Sieber, K. Engelborghs, T. Luzyanina, G. Samaey, and D. Roose. *DDE-BIFTOOL Manual - Bifurcation analysis of delay differential equations*, 2015. Eprint arXiv:1406.7144 [math.DS].
- [73] R. Sipahi, F. M. Atay, and S.-I. Niculescu. Stability of traffic flow behavior with distributed delays modeling the memory effects of the drivers. *SIAM J. Appl. Math.*, 68(3):738–759, 2008.
- [74] H. Smith. *An Introduction to Delay Differential Equations with Applications to the Life Sciences*. Texts in Applied Mathematics. Springer, New York, 2011.
- [75] G. Stépán. *Retarded dynamical systems: stability and characteristic functions*. Longman Scientific & Technical, 1989.
- [76] E. Stumpf. On a differential equation with state-dependent delay: a center-unstable manifold connecting an equilibrium and a periodic orbit. *J. Dyn. Diff. Equat.*, 24(2):197–248, 2012.
- [77] R. Szalai and D. Roose. Continuation and bifurcation analysis of delay differential equations. In B. Krauskopf, H. M. Osinga, and J. Galán-Vioque, editors, *Numerical Continuation Methods for Dynamical Systems: Path following and boundary value problems*, pages 359–399. Springer-Verlag, 2007.
- [78] B. Wage. Normal form computations for delay differential equations in DDE-BIFTOOL. Master’s thesis, Universiteit Utrecht, Holland, 2014.
- [79] E. Wall, F. Guichard, and A. R. Humphries. Synchronization in ecological systems by weak dispersal coupling with time delay. *Theor. Ecol.*, 6:405–418, 2013.
- [80] H.-O. Walther. Smoothness properties of semiflows for differential equations with state-dependent delays. *J. Math. Sci.*, 124:5193–5207, 2004.
- [81] H.-O. Walther. Complicated histories close to a homoclinic loop generated by variable delay. *Adv. Differential Equations*, 19:911–946, 2014.
- [82] Y. Yuan and J. Bélair. Threshold dynamics in an SEIRS model with latency and temporary immunity. *J. Math. Biol.*, 69(4):875–904, 2014.

**A. Computation of the Hopf-Hopf Normal Form.** Here we describe in detail the derivation of the normal form of the Hopf-Hopf bifurcation for the truncated constant-delay DDE (2.14) from Sec. 2.1, where we follow the derivation of Wu and Guo [23]. The computational task is to derive the restriction of the semi-flow of (2.14) to the four-dimensional center manifold up to third order, which is an ODE from which the type of Hopf-Hopf bifurcation can be determined [51]. We elaborate these steps as follows. In Sec. A.1 we construct a projection to the center manifold for the constant-delay DDE (2.14), and in Sec. A.2 we study the flow on the center manifold near the Hopf-Hopf bifurcation. We then compute the quadratic and cubic terms of this flow in Sec. A.3, which enables us to determine the normal form and type of Hopf-Hopf bifurcation in Sec. A.4.

**A.1. Center manifold.** To construct the center manifold for the constant delay DDE (2.14) we write it as an RFDE in the form (1.1), that is, as a sum of linear and nonlinear operators as

$$u'(t) = \mathcal{L}u_t + \mathcal{F}(u_t). \quad (\text{A.1})$$

It follows from (1.9) and (1.11) that

$$\mathcal{L}u_t = -\gamma u_t(0) - \kappa_1 u_t(-a_1) - \kappa_2 u_t(-a_2), \quad (\text{A.2})$$

$$\mathcal{F}(u_t) = F(u_t) - \mathcal{L}u_t, \quad (\text{A.3})$$

while, from Sec. 2.1, the nonlinear operator is given by

$$\begin{aligned} \mathcal{F}(u_t) = & \sum_{i=1}^2 \kappa_i (cu_t(0)) Lu_t(-a_i) + \sum_{i,j=1}^2 \kappa_i \kappa_j c^2 u_t(0) u_t(-a_i) Lu_t(-a_i - a_j) \\ & - \frac{1}{2} (cu_t(0))^2 \sum_{i=1}^2 \kappa_i L^2 u_t(-a_i). \end{aligned} \quad (\text{A.4})$$

Here, the difference operator  $L$  defined in (2.1), has been applied to  $u_t$  in the natural way, so

$$\begin{aligned} Lu_t(\theta) &= -\gamma u_t(\theta) - \kappa_1 u_t(\theta - a_1) - \kappa_2 u_t(\theta - a_2) \\ &= -\gamma u(t + \theta) - \kappa_1 u(t + \theta - a_1) - \kappa_2 u(t + \theta - a_2). \end{aligned} \quad (\text{A.5})$$

We start by introducing the appropriate spaces and operators that we will need to perform the reduction to a four-dimensional center manifold at a Hopf-Hopf bifurcation point. Throughout this section we will follow the notation used in Wu and Guo [23] and adapt the corresponding theory to study (A.1) near Hopf-Hopf bifurcations.

As noted in the introduction, it is standard to treat the RFDE (1.1) as an infinite-dimensional dynamical system in the Banach space of continuous functions of an interval into  $\mathbb{R}^d$ . For the scalar DDE (A.1) we have  $d = 1$ , and we equip  $\mathbb{R}$  with the Euclidian norm,  $|\cdot|$ , and, for given  $\tau > 0$ , we define

$$C = C([- \tau, 0], \mathbb{R}), \quad (\text{A.6})$$

the Banach space of continuous mappings, equipped with the supremum norm. For  $\varphi \in C$ , this norm is given by

$$\|\varphi\| = \sup_{\theta \in [-\tau, 0]} |\varphi(\theta)|.$$

In an analogous manner, we define

$$C^1 = C^1([- \tau, 0], \mathbb{R}), \quad (\text{A.7})$$

the space of continuous differentiable mappings with continuous derivative, which is also a Banach space with the corresponding supremum norm

$$\|\varphi\| = \sup_{\theta \in [-\tau, 0]} (|\varphi(\theta)| + |\frac{d}{d\theta}\varphi(\theta)|), \quad \varphi \in C^1.$$

With  $u_t \in C$  defined by (1.2) equation (A.1) defines an RFDE of the form (1.1) provided  $\mathcal{L} : C \rightarrow \mathbb{R}$  and  $\mathcal{F} : C \rightarrow \mathbb{R}$ . The linear operator  $\mathcal{L}$  is defined in (A.2), and it is a continuous operator from  $C$  into  $\mathbb{R}$  whenever  $\tau \geq a_2$  (recalling that  $a_2 > a_1$ ). However, some care needs to be taken with the operator  $\mathcal{F}$ . As noted in Sec. 2.1, the truncation to third order results in constant delays, the largest of which is  $\tau = 3a_2$ . This shows up in (A.4) where  $u(t - 3a_2)$  appears in both the terms  $Lu_t(-2a_2)$  and  $L^2u_t(-a_2)$ . Hence, we require  $\tau \geq 3a_2$  for  $\mathcal{F} : C \rightarrow \mathbb{R}$  and for (A.1) to define an RFDE. This contrasts with the state-dependent DDE (1.3), which in (1.9) we defined as an RFDE with  $\tau = a_2 + \frac{a_1}{\gamma}(\kappa_1 + \kappa_2)$ .

In the following consider (A.1) as an RFDE with  $C$  defined by (A.6) and  $\tau = 3a_2$ . The linearized system associated to (A.1) is

$$u'(t) = \mathcal{L}u_t. \quad (\text{A.8})$$

Since the linear operator  $\mathcal{L} : C \rightarrow \mathbb{R}$ , defined in (A.2), is continuous, then, as shown in [27] by the Riesz representation theorem, there exists a function  $\eta : [-\tau, 0] \rightarrow \mathbb{R}$  of bounded variation such that

$$\mathcal{L}\varphi = \int_{-\tau}^0 d\eta(\theta)\varphi(\theta), \quad \forall \varphi \in C.$$

The function  $\eta$  satisfies that  $\eta(\theta) = 0$  for  $\eta \in (-\tau, -a_2) \cup (-a_2, -a_1) \cup (-a_1, 0)$ ,  $\eta(0) = -\gamma$ ,  $\eta(-a_1) = -\kappa_1$ ,  $\eta(-a_2) = -\kappa_2$ . Therefore,

$$\mathcal{L}\varphi = \int_{-3a_2}^0 d\eta(\theta)\varphi(\theta) = -\gamma\varphi(0) - \kappa_1\varphi(-a_1) - \kappa_2\varphi(-a_2). \quad (\text{A.9})$$

Let  $T(t) : C \rightarrow C$  be the solution operator of the linear system (A.8). Then, as is shown in [27], the infinitesimal generator  $\mathcal{A}$  of the semi-group  $T(t)$  is defined by

$$\mathcal{A}\varphi = \lim_{t \rightarrow 0^+} \frac{T(t)\varphi - \varphi}{t}$$

for  $\varphi \in C$ , which results in

$$\frac{d}{dt}T(t)\varphi = \mathcal{A}T(t)\varphi \quad (\text{A.10})$$

and

$$(\mathcal{A}\varphi)(\theta) = \begin{cases} \frac{d}{d\theta}\varphi, & \text{if } \theta \in [-\tau, 0), \\ -\gamma\varphi(0) - \kappa_1\varphi(-a_1) - \kappa_2\varphi(-a_2), & \text{if } \theta = 0. \end{cases} \quad (\text{A.11})$$

Here the domain of  $\mathcal{A}$  is given by

$$\text{dom}(\mathcal{A}) = \{\varphi : \varphi \in C^1, \varphi'(0) = \mathcal{L}\varphi\}.$$

Following [23], we now enlarge the phase space  $C$  so that (A.1) can be written as an abstract ODE in a Banach space. Let  $BC$  be the set of functions from  $[-\tau, 0]$  to  $\mathbb{R}$  that are uniformly

continuous on  $[-\tau, 0)$  and may have a jump discontinuity at 0. We also introduce the function  $X_0 : [-\tau, 0] \rightarrow \mathbb{R}$  defined by

$$X_0(\theta) = \begin{cases} 1, & \theta = 0, \\ 0, & \theta \in [-\tau, 0). \end{cases}$$

Then every  $\varphi \in BC$  can be expressed as  $\varphi = \phi + X_0\xi$  with  $\phi \in C$  and  $\xi \in \mathbb{R}$ , and thus  $BC$  can be identified with  $C \times \mathbb{R}$ . We equip  $BC$  with the norm  $|\phi + X_0\xi| = \|\phi\| + |\xi|$ , which is then also a Banach space.

The spectrum of the infinitesimal generator  $\mathcal{A}$  consists of the eigenvalues  $\lambda \in \sigma(\mathcal{A})$  that satisfy the characteristic equation

$$0 = \Delta(\lambda) = \lambda - \int_{-\tau}^0 e^{\lambda\theta} d\eta(\theta) = \lambda + \gamma + \kappa_1 e^{-a_1\lambda} + \kappa_2 e^{-a_2\lambda}. \quad (\text{A.12})$$

For any  $\lambda \in \sigma(\mathcal{A})$ , the generalized eigenspace  $\mathcal{M}_\lambda(\mathcal{A})$  is finite-dimensional and, since in our case the eigenvalues will have multiplicity 1, we write  $\mathcal{M}_{\lambda_i}(\mathcal{A}) = \ker(\lambda_i I - \mathcal{A})$  and we have the decomposition

$$C = \ker(\lambda I - \mathcal{A}) \oplus \text{im}(\lambda I - \mathcal{A}).$$

If we have a set of distinct eigenvalues  $\Lambda = \{\lambda_1, \dots, \lambda_d\} \subset \sigma(\mathcal{A})$ , we will use the notation  $\mathcal{M}_\Lambda(\mathcal{A})$  for the generalized eigenspace corresponding to those eigenvalues. Let  $d = \dim \mathcal{M}_\Lambda(\mathcal{A})$ , and  $\varphi_1, \dots, \varphi_d$  be a basis for  $\mathcal{M}_\Lambda(\mathcal{A})$ , and  $\Phi_\Lambda = (\varphi_1, \dots, \varphi_d)$ . Then there exists a  $d \times d$  constant matrix  $B = B_\Lambda$  such that  $\mathcal{A}\Phi_\Lambda = \Phi_\Lambda B$ , and

- i) the only eigenvalues of  $B$  are  $\Lambda = \{\lambda_1, \dots, \lambda_d\}$ ,
- ii)  $\Phi_\Lambda(\theta) = \Phi_\Lambda(0)e^{B\theta}$ ,
- iii)  $T(t)\Phi_\Lambda = \Phi_\Lambda e^{Bt}$ , where  $T(t)$  satisfies (A.10).

We denote by  $C^*$  the dual of  $C$ , so  $C^* = C([0, \tau], \mathbb{R}^*) = C([0, \tau], \mathbb{R})$ , the space of continuous functions from  $[0, \tau]$  to  $\mathbb{R}$  with norm given for a function  $y \in C^*$  by,

$$\|y\| = \sup_{t \in [0, \tau]} |y(t)|.$$

We also introduce a bilinear form associated with  $\mathcal{L}$ , for  $\varphi \in C$  and  $\psi \in C^*$ , as

$$\langle \psi, \varphi \rangle = \bar{\psi}(0)\varphi(0) - \kappa_1 \int_{-a_1}^0 \bar{\psi}(s + a_1)\varphi(s)ds - \kappa_2 \int_{-a_2}^0 \bar{\psi}(s + a_2)\varphi(s)ds. \quad (\text{A.13})$$

Then we can find, at least formally, an adjoint linearized problem,

$$y'(t) = \gamma y(t) + \kappa_1 y(t + a_1) + \kappa_2 y(t + a_2)$$

acting on functions  $y_t \in C^*$ , with the corresponding solution operator  $T^* : C^* \rightarrow C^*$ . We denote the infinitesimal generator of the strongly continuous semi-group  $T^*$  by  $\mathcal{A}^*$ . For  $\psi \in C^*$ ,  $\mathcal{A}^*\psi$  is defined by

$$(\mathcal{A}^*\psi)(\xi) = \begin{cases} -\frac{d}{d\xi}\psi(\xi), & \text{if } \xi \in (0, \tau], \\ \gamma\psi(0) + \kappa_1\psi(-a_1) + \kappa_2\psi(-a_2), & \text{if } \xi = 0. \end{cases} \quad (\text{A.14})$$

The operators  $\mathcal{A}$  and  $\mathcal{A}^*$  as defined by (A.11) and (A.14) are then adjoint with respect to the bilinear form (A.13); that is

$$\langle \psi, \mathcal{A}\varphi \rangle = \langle \mathcal{A}^*\psi, \varphi \rangle, \quad \varphi \in C, \psi \in C^*.$$

**A.2. Hopf-Hopf bifurcation.** We will now use the properties of  $\mathcal{A}$  and  $\mathcal{A}^*$  to construct a basis of eigenfunctions for the center space and the adjoint of the center space at the Hopf-Hopf bifurcation. At a Hopf-Hopf bifurcation, the infinitesimal generator  $\mathcal{A}$  defined by (A.11) has two pairs of simple purely imaginary eigenvalues  $\pm i\omega_1$  and  $\pm i\omega_2$  that do not have a strong resonance; that is,  $k\omega_1 \neq \ell\omega_2$  where  $k$  and  $\ell$  are positive integers with  $k + \ell \leq 5$ .

Following the discussion in Sec. A.1, we know that the generalized center eigenspace  $E^c = \mathcal{M}_{\{\pm i\omega_1, \pm i\omega_2\}}$  is a four-dimensional linear space. We also have two complex conjugate eigenvectors  $q_1, q_2 \in C$  such that

$$\mathcal{A}q_j = i\omega_j q_j, \quad \text{for } j = 1, 2,$$

namely,  $q_j(\theta) = e^{i\omega_j \theta}$ , since clearly  $\frac{dq_j}{d\theta} = i\omega_j q_j$ , while at the Hopf-Hopf point we have

$$\mathcal{A}q_j(0) = -\gamma q_j(0) - \kappa_1 q_j(-a_1) - \kappa_2 q_j(-a_2) = -\gamma - \kappa_1 e^{-i\omega_j a_1} - \kappa_2 e^{-i\omega_j a_2} = i\omega_j q_j(0),$$

as required to satisfy (A.11). We also introduce the adjoint eigenvectors  $p_1, p_2 \in C^*$ , such that

$$\mathcal{A}^* p_j = -i\omega_j p_j, \quad \text{for } j = 1, 2.$$

Then,

$$p_j(s) = D_j e^{i\omega_j s}.$$

We choose the constants  $D_j = 1 / \left( \overline{1 - \kappa_1 e^{-ia_1 \omega_j} - \kappa_2 e^{-ia_2 \omega_j}} \right)$  so that that these eigenvectors are normalized with respect to the bilinear form (A.13), that is,

$$\langle p_j, q_k \rangle = \delta_{j,k}, \quad \text{and} \quad \langle p_j, \bar{q}_k \rangle = 0.$$

Therefore, if we let  $\Phi = (q_1, \bar{q}_1, q_2, \bar{q}_2)$  and  $\Psi = (p_1, \bar{p}_1, p_2, \bar{p}_2)^T$ . Then  $\langle \Psi, \Phi \rangle = Id_4$ . Hence,  $\Phi$  is a basis for  $P = E^c$  and  $\Psi$  is a basis for  $E^{c*} = P^*$  in  $C^*$  and we have that  $\frac{d}{d\theta} \Phi = \Phi B$ , where

$$B = \begin{pmatrix} i\omega_1 & 0 & 0 & 0 \\ 0 & -i\omega_1 & 0 & 0 \\ 0 & 0 & i\omega_2 & 0 \\ 0 & 0 & 0 & -i\omega_2 \end{pmatrix}.$$

It follows that  $BC = P \oplus \ker \Pi$  with  $E^s \oplus E^u \subset \ker \Pi$ , where for  $\varphi = \phi + X_0 \xi \in BC$  the projection  $\Pi : BC \rightarrow P$  is defined by

$$\Pi(\varphi) = \Pi(\phi + X_0 \xi) = \Phi \langle \Psi, \phi + X_0 \xi \rangle = \Phi [\langle \Psi, \phi \rangle + \bar{\Psi}(0) \xi]$$

for  $\phi \in C$  and  $\xi \in \mathbb{R}$ .

So the abstract ODE in  $BC$  associated with (A.1) can be rewritten in the form

$$\frac{d}{dt} u_t = \mathcal{A} u_t + X_0 \mathcal{F}(u_t). \quad (\text{A.15})$$

For the solution  $u_t$  of (A.15) we define  $z_j(t) = \langle p_j, u_t \rangle$  with  $j = 1, 2$  and

$$\begin{aligned} w(z) &= u_t - \left( z_1(t) e^{i\omega_1 \theta} + z_2(t) e^{i\omega_2 \theta} + \bar{z}_1(t) e^{-i\omega_1 \theta} + \bar{z}_2(t) e^{-i\omega_2 \theta} \right) \\ &= u_t - 2\text{Re} \left( z_1(t) e^{i\omega_1 \theta} + z_2(t) e^{i\omega_2 \theta} \right), \end{aligned} \quad (\text{A.16})$$

where  $z = (z_1, z_2) \in \mathbb{C}^2$ . In fact,  $z_j$  and  $\bar{z}_j$  are local coordinates for the center manifold  $\mathcal{M}_{\text{loc}}$  in the directions of  $D_j e^{i\omega_j s}$  and  $\bar{D}_j e^{-i\omega_j s}$ ,  $j = 1, 2$ . We notice that

$$\begin{aligned}\langle p_j, w(z) \rangle &= \langle D_j e^{i\omega_j s}, w(z) \rangle = \langle D_j e^{i\omega_j s}, u_t - 2\text{Re}(z_1(t)e^{i\omega_1\theta} + z_2(t)e^{i\omega_2\theta}) \rangle \\ &= z_j(t) - \langle D_j e^{i\omega_j s}, 2\text{Re}(z_1(t)e^{i\omega_1\theta} + z_2(t)e^{i\omega_2\theta}) \rangle = z_j(t) - z_j(t) = 0.\end{aligned}$$

Then for the solutions  $u_t$  of (A.15) that belong to  $\mathcal{M}_{\text{loc}}$ , we have that

$$\begin{aligned}\dot{z}_j(t) &= \langle D_j e^{i\omega_j s}, \dot{u}_t \rangle = \langle D_j e^{i\omega_j s}, \mathcal{A}u_t + X_0 \mathcal{F}(u_t) \rangle \\ &= \langle \mathcal{A}^* D_j e^{i\omega_j s}, u_t \rangle + \langle D_j e^{i\omega_j s}, X_0 \mathcal{F}(u_t) \rangle \\ &= i\omega_j z_j(t) + \langle D_j e^{i\omega_j s}, X_0 \mathcal{F}(u_t) \rangle = i\omega_j z_j(t) + \bar{D}_j \mathcal{F}(u_t) \\ &= i\omega_j z_j(t) + \bar{D}_j \mathcal{F}(w(z) + 2\text{Re}(z_1(t)e^{i\omega_1\theta} + z_2(t)e^{i\omega_2\theta})).\end{aligned}$$

Therefore, the flow on the center manifold satisfies

$$\dot{z}_j(t) = i\omega_j z_j(t) + g^j(z(t)), \quad (\text{A.17})$$

where

$$g^j(z(t)) = \bar{D}_j \mathcal{F}(w(z) + 2\text{Re}(z_1(t)e^{i\omega_1\theta} + z_2(t)e^{i\omega_2\theta})) \quad (\text{A.18})$$

and  $w(z)$  satisfies the ODE projected into the complement of  $P$ , that is,

$$\frac{d}{dt}w = \mathcal{A}w + (X_0 - \Phi\bar{\Psi}(0))\mathcal{F}(w(z) + 2\text{Re}(z_1(t)e^{i\omega_1\theta} + z_2(t)e^{i\omega_2\theta})). \quad (\text{A.19})$$

**A.3. Complex ODE.** To find the normal form we need explicit expressions of the flow (A.17) on the center manifold. We let

$$g^j(z) = \sum_{\ell+s+r+k \geq 2} \frac{1}{\ell!s!r!k!} g_{\ell s r k}^j z_1^\ell \bar{z}_1^r z_2^s \bar{z}_2^k \quad (\text{A.20})$$

and

$$w(z) = \sum_{\ell+s+r+k \geq 2} \frac{1}{\ell!s!r!k!} w_{\ell s r k} z_1^\ell \bar{z}_1^r z_2^s \bar{z}_2^k. \quad (\text{A.21})$$

Then we can compute the terms of order two and three of the flow (A.17) on the center manifold that we will require for the normal form computation.

The nonlinearity  $\mathcal{F} : C \rightarrow \mathbb{R}$  defined by (A.4) for the RFDE (A.1) contains only quadratic and cubic terms and, hence, for  $\varphi \in C$  (with  $\tau = 3a_2$ ) we can expand the nonlinearity as

$$\begin{aligned}\mathcal{F}(\varphi) &= \sum_{i=1}^2 \kappa_i (c\varphi(0)) L\varphi(-a_i) + \sum_{i,j=1}^2 \kappa_i \kappa_j c^2 \varphi(0) \varphi(-a_i) L\varphi(-a_i - a_j) \\ &\quad - \frac{1}{2} (c\varphi(0))^2 \sum_{i=1}^2 \kappa_i L^2 \varphi(-a_i) \\ &= \frac{1}{2} \mathcal{F}^2(\varphi, \varphi) + \frac{1}{6} \mathcal{F}^3(\varphi, \varphi, \varphi),\end{aligned} \quad (\text{A.22})$$

$$= \frac{1}{2} \mathcal{F}^2(\varphi, \varphi) + \frac{1}{6} \mathcal{F}^3(\varphi, \varphi, \varphi), \quad (\text{A.23})$$

where  $\mathcal{F}^j$  are the  $j$ -th order terms given by

$$\mathcal{F}^j(\nu_1, \dots, \nu_j) = \frac{\partial^j}{\partial t_1 \partial t_2 \dots \partial t_j} \mathcal{F} \left( \sum_{s=1}^j t_s \nu_s \right) \Big|_{t_1=t_2=\dots=t_j=0}$$

and  $L$  is the difference operator defined by (A.5). We obtain that, for  $\nu_1, \nu_2, \nu_3 \in C$ ,

$$\mathcal{F}^2(\nu_1, \nu_2) = \sum_{i=1}^2 \kappa_i c[\nu_1(0)\nu_2'(-a_i) + \nu_2(0)\nu_1'(-a_i)] \quad (\text{A.24})$$

and

$$\mathcal{F}^3(\nu_1, \nu_2, \nu_3) = - \sum_{\sigma \in S_3} c^2(\nu_{\sigma(1)}(0)\nu_{\sigma(2)}(0))[\kappa_1 \nu_{\sigma(3)}''(-a_1) + \kappa_2 \nu_{\sigma(3)}''(-a_2)], \quad (\text{A.25})$$

where the first sum is taken over the group  $S_3$  of permutations of three elements. Evaluating these expressions in the elements of the basis  $\Phi$ , using (A.18), we obtain the terms of the expansion.

The quadratic terms of the flow (A.17) for the our specific equation (A.1) are given by

$$\begin{aligned} g_{2000}^j &= \bar{p}_j(0) \mathcal{F}^2(q_1(\theta), q_1(\theta)) = \bar{D}_j 2c \sum_{i=1}^2 \kappa_i e^{-i\omega_1 a_1} (-\gamma - \kappa_1 e^{-i\omega_1 a_1} - \kappa_2 e^{-i\omega_1 a_2}) \\ &= \bar{D}_j 2ci\omega_1 \sum_{i=1}^2 \kappa_i e^{-i\omega_1 a_1} = \bar{D}_j 2ci\omega_1 (-\gamma - i\omega_1) \end{aligned}$$

and similarly

$$g_{0020}^j = \bar{p}_j(0) \mathcal{F}^2(q_1(\theta), q_1(\theta)) = \bar{D}_j 2ci\omega_2 \sum_{i=1}^2 \kappa_i e^{-i\omega_2 a_1} = \bar{D}_j 2ci\omega_2 (-\gamma - i\omega_2),$$

where we have used that  $i\omega_j = -\gamma - \kappa_1 e^{-ia_1\omega_j} - \kappa_2 e^{-ia_2\omega_j}$ . The remaining quadratic terms are obtained similarly as

$$\begin{aligned} g_{1100}^j &= 2\bar{D}_j c\omega_1^2, & g_{0011}^j &= 2\bar{D}_j c\omega_2^2, & g_{1010}^j &= \bar{D}_j c(\omega_1^2 + \omega_2^2 - i\gamma(\omega_1 + \omega_2)), \\ g_{0101}^j &= \bar{D}_j c(\omega_1^2 + \omega_2^2 + i\gamma(\omega_1 + \omega_2)), & g_{1001}^j &= \bar{D}_j c(\omega_1^2 + \omega_2^2 - i\gamma(\omega_1 - \omega_2)), \\ g_{0110}^j &= \bar{D}_j c(\omega_1^2 + \omega_2^2 + i\gamma(\omega_1 - \omega_2)), & g_{0200}^j &= -\bar{D}_j 2ci\omega_1(-\gamma - i\omega_1), \\ g_{0002}^j &= -\bar{D}_j 2ci\omega_2(-\gamma + i\omega_2). \end{aligned}$$

Finally, we need to determine a few terms of the expansion of the graph of the center manifold from (A.19), namely the terms  $w_{1100}, w_{2000}, w_{1010}, w_{1001}, w_{0002}$ , and  $w_{0011}$ . We will determine these by substituting the expansion (A.21) into (A.19). From the definition of  $\mathcal{A}$  in (A.11) this results in a differential equation and a boundary condition that each coefficient of (A.21) must satisfy.

For the coefficient  $w_{2000}$  we obtain the differential equation

$$\frac{d}{d\theta} w_{2000}(\theta) = 2i\omega_1 w_{2000}(\theta) + g_{2000}^1 e^{i\omega_1 \theta} + \bar{g}_{0200}^1 e^{-i\omega_1 \theta} + g_{2000}^2 e^{i\omega_2 \theta} + \bar{g}_{2000}^2 e^{-i\omega_2 \theta}, \quad (\text{A.26})$$

together with the boundary condition

$$\mathcal{L}w_{2000} = 2i\omega_1 w_{2000}(0) + g_{2000}^1 + \bar{g}_{0200}^1 + g_{2000}^2 + \bar{g}_{2000}^2 - \mathcal{F}^2(q_1, q_1). \quad (\text{A.27})$$



The ODE (A.26) can be solved by using an integrating factor to obtain

$$w_{2000}(\theta) = -\frac{g_{2000}^1 e^{i\omega_1 \theta}}{i\omega_1} - \frac{\bar{g}_{0200}^1 e^{-i\omega_1 \theta}}{3i\omega_1} + \frac{g_{2000}^2 e^{i\omega_2 \theta}}{i(\omega_2 - 2\omega_1)} - \frac{\bar{g}_{0200}^2 e^{-i\omega_2 \theta}}{i(\omega_2 + 2\omega_1)} + E_{2000} e^{2i\omega_1 \theta}. \quad (\text{A.28})$$

To determine the constant of integration  $E_{2000}$ , notice that (A.28) implies

$$\mathcal{L}w_{2000} = -\frac{g_{2000}^1(i\omega_1)}{i\omega_1} - \frac{\bar{g}_{0200}^1(-i\omega_1)}{3i\omega_1} + \frac{g_{2000}^2(i\omega_2)}{i(\omega_2 - 2\omega_1)} - \frac{\bar{g}_{0200}^2(-i\omega_2)}{i(\omega_2 + 2\omega_1)} + E_{2000}(-\Delta(2\omega_1) + 2i\omega_1)$$

and

$$2i\omega_1 w_{2000}(0) = -\frac{g_{2000}^1(2i\omega_1)}{i\omega_1} - \frac{\bar{g}_{0200}^1(2i\omega_1)}{3i\omega_1} + \frac{g_{2000}^2(2i\omega_1)}{i(\omega_2 - 2\omega_1)} - \frac{\bar{g}_{0200}^2(2i\omega_1)}{i(\omega_2 + 2\omega_1)} + E_{2000}(2i\omega_1).$$

Substituting these expressions into (A.27) we obtain

$$E_{2000} = \frac{\mathcal{F}^2(q_1, q_1)}{\Delta(2i\omega_1)}.$$

We determine  $w_{1100}$ ,  $w_{1010}$ ,  $w_{1001}$ ,  $w_{0020}$ , and  $w_{0011}$  similarly. The equations that they satisfy are given by

$$\left. \begin{aligned} \frac{d}{d\theta} w_{1100}(\theta) &= g_{1100}^1 e^{i\omega_1 \theta} + \bar{g}_{1100}^1 e^{-i\omega_1 \theta} + g_{1100}^2 e^{i\omega_2 \theta} + \bar{g}_{100}^2 e^{-i\omega_2 \theta}, \\ \mathcal{L}w_{1100} &= g_{1100}^1 + \bar{g}_{0011}^1 + g_{1100}^2 + \bar{g}_{0011}^2 - \mathcal{F}^2(q_2, \bar{q}_2), \end{aligned} \right\}$$

$$\left. \begin{aligned} \frac{d}{d\theta} w_{1010}(\theta) &= i(\omega_1 + \omega_2) w_{1010}(\theta) + g_{1010}^1 e^{i\omega_1 \theta} + \bar{g}_{0101}^1 e^{-i\omega_1 \theta} + g_{1010}^2 e^{i\omega_2 \theta} + \bar{g}_{0101}^2 e^{-i\omega_2 \theta}, \\ \mathcal{L}w_{1010} &= i(\omega_1 + \omega_2) w_{1010}(0) + g_{1010}^1 + \bar{g}_{0101}^1 + g_{1010}^2 + \bar{g}_{0101}^2 - \mathcal{F}^2(q_1, q_2), \end{aligned} \right\}$$

$$\left. \begin{aligned} \frac{d}{d\theta} w_{1001}(\theta) &= i(\omega_1 - \omega_2) w_{1001}(\theta) + g_{1001}^1 e^{i\omega_1 \theta} + \bar{g}_{0110}^1 e^{-i\omega_1 \theta} + g_{1001}^2 e^{i\omega_2 \theta} + \bar{g}_{0110}^2 e^{-i\omega_2 \theta}, \\ \mathcal{L}w_{1001} &= i(\omega_1 - \omega_2) w_{1001}(0) + g_{1001}^1 + \bar{g}_{0110}^1 + g_{1001}^2 + \bar{g}_{0110}^2 - \mathcal{F}^2(\bar{q}_1, q_2), \end{aligned} \right\}$$

$$\left. \begin{aligned} \frac{d}{d\theta} w_{0020}(\theta) &= 2i\omega_2 w_{0020}(\theta) + g_{0020}^1 e^{i\omega_1 \theta} + \bar{g}_{0002}^1 e^{-i\omega_1 \theta} + g_{0020}^2 e^{i\omega_2 \theta} + \bar{g}_{0002}^2 e^{-i\omega_2 \theta}, \\ \mathcal{L}w_{0020} &= 2i\omega_2 w_{0020}(0) + g_{0020}^1 + \bar{g}_{0002}^1 + g_{0020}^2 + \bar{g}_{0002}^2 - \mathcal{F}^2(q_2, q_2), \end{aligned} \right\}$$

$$\left. \begin{aligned} \frac{d}{d\theta} w_{0011}(\theta) &= g_{0011}^1 e^{i\omega_1 \theta} + \bar{g}_{0011}^1 e^{-i\omega_1 \theta} + g_{0011}^2 e^{i\omega_2 \theta} + \bar{g}_{0011}^2 e^{-i\omega_2 \theta}, \\ \mathcal{L}w_{0011} &= g_{0011}^1 + \bar{g}_{0011}^1 + g_{0011}^2 + \bar{g}_{0011}^2 - \mathcal{F}^2(q_2, \bar{q}_2). \end{aligned} \right\}$$

These equations are solved similarly to (A.26) and (A.27) to obtain expressions equivalent to those of [23] for all the quadratic coefficients of the graph of the center manifold  $w(z)$  as

$$\begin{aligned} w_{2000} &= -\frac{g_{2000}^1 e^{i\omega_1 \theta}}{i\omega_1} - \frac{\bar{g}_{0200}^1 e^{-i\omega_1 \theta}}{3i\omega_1} + \frac{g_{2000}^2 e^{i\omega_2 \theta}}{i(\omega_2 - 2\omega_1)} - \frac{\bar{g}_{0200}^2 e^{-i\omega_2 \theta}}{i(\omega_2 + 2\omega_1)} + E_{2000} e^{2i\omega_1 \theta}, \\ w_{1100} &= \frac{g_{1100}^1 e^{i\omega_1 \theta}}{i\omega_1} - \frac{\bar{g}_{1100}^1 e^{-i\omega_1 \theta}}{i\omega_1} + \frac{g_{1100}^2 e^{i\omega_2 \theta}}{i\omega_2} - \frac{\bar{g}_{1100}^2 e^{-i\omega_2 \theta}}{i\omega_2} + E_{1100}, \\ w_{1010} &= -\frac{g_{1010}^1 e^{i\omega_1 \theta}}{i\omega_2} - \frac{\bar{g}_{0101}^1 e^{-i\omega_1 \theta}}{i(2\omega_1 + \omega_2)} - \frac{g_{1010}^2 e^{i\omega_2 \theta}}{i\omega_1} - \frac{\bar{g}_{0101}^2 e^{-i\omega_2 \theta}}{i(\omega_1 + 2\omega_2)} + E_{1010} e^{i(\omega_1 + \omega_2)\theta}, \\ w_{1001} &= \frac{g_{1001}^1 e^{i\omega_1 \theta}}{i\omega_2} + \frac{\bar{g}_{0110}^1 e^{-i\omega_1 \theta}}{i(\omega_2 - 2\omega_1)} + \frac{g_{1001}^2 e^{i\omega_2 \theta}}{i(2\omega_2 - \omega_1)} - \frac{\bar{g}_{0110}^2 e^{-i\omega_2 \theta}}{i\omega_1} + E_{1001} e^{i(\omega_1 - \omega_2)\theta}, \\ w_{0020} &= \frac{g_{0020}^1 e^{i\omega_1 \theta}}{i(\omega_1 - 2\omega_2)} - \frac{\bar{g}_{0002}^1 e^{-i\omega_1 \theta}}{i(\omega_1 + 2\omega_2)} - \frac{g_{0020}^2 e^{i\omega_2 \theta}}{i\omega_2} - \frac{\bar{g}_{0002}^2 e^{-i\omega_2 \theta}}{3i\omega_2} + E_{0020} e^{2i\omega_2 \theta}, \\ w_{0011} &= \frac{g_{0011}^1 e^{i\omega_1 \theta}}{i\omega_1} - \frac{\bar{g}_{0011}^1 e^{-i\omega_1 \theta}}{i\omega_1} + \frac{g_{0011}^2 e^{i\omega_2 \theta}}{i\omega_2} - \frac{\bar{g}_{0011}^2 e^{-i\omega_2 \theta}}{i\omega_2} + E_{0011}, \end{aligned}$$

where the constants of integration are given by

$$\begin{aligned} E_{1100} &= \frac{\mathcal{F}^2(q_1, \bar{q}_1)}{\Delta(0)}, & E_{2000} &= \frac{\mathcal{F}^2(q_1, q_1)}{\Delta(2i\omega_1)}, & E_{1010} &= \frac{\mathcal{F}^2(q_1, q_2)}{\Delta(i(\omega_1 + \omega_2))}, \\ E_{1001} &= \frac{\mathcal{F}^2(q_1, \bar{q}_2)}{\Delta(i(\omega_1 - \omega_2))}, & E_{0020} &= \frac{\mathcal{F}^2(q_2, q_2)}{\Delta(2i\omega_2)}, & E_{0011} &= \frac{\mathcal{F}^2(q_2, \bar{q}_2)}{\Delta(0)}, \end{aligned}$$

and  $\Delta$  is the characteristic function defined in (A.12). Finally the cubic terms are given by the expressions

$$\begin{aligned} g_{2100}^j &= \bar{D}_j \mathcal{F}^3(q_1, q_1, \bar{q}_1) + 2\bar{D}_j \mathcal{F}^2(q_1, w_{1100}) + \bar{D}_j \mathcal{F}^2(\bar{q}_1, w_{2000}), \\ g_{1011}^j &= \bar{D}_j \mathcal{F}^3(q_1, q_2, \bar{q}_2) + \bar{D}_j \mathcal{F}^2(q_1, w_{0011}) + \bar{D}_j \mathcal{F}^2(q_2, w_{1001}) + \bar{D}_j \mathcal{F}^2(\bar{q}_2, w_{1010}), \\ g_{1110}^j &= \bar{D}_j \mathcal{F}^3(q_1, \bar{q}_1, q_2) + \bar{D}_j \mathcal{F}^2(q_1, \bar{w}_{1001}) + \bar{D}_j \mathcal{F}^2(q_2, w_{1100}) + \bar{D}_j \mathcal{F}^2(\bar{q}_1, w_{1010}), \\ g_{0021}^j &= \bar{D}_j \mathcal{F}^3(q_2, q_2, \bar{q}_2) + 2\bar{D}_j \mathcal{F}^2(q_2, w_{0011}) + \bar{D}_j \mathcal{F}^2(\bar{q}_2, w_{0020}), \end{aligned} \tag{A.29}$$

where, from formula (A.25),

$$\begin{aligned} \mathcal{F}^3(q_1, q_1, \bar{q}_1) &= -c^2 \omega_1^2 [3\gamma + i\omega_1], & \mathcal{F}^3(q_2, q_2, \bar{q}_2) &= -c^2 \omega_2^2 [3\gamma + i\omega_2], \\ \mathcal{F}^3(q_1, \bar{q}_1, q_2) &= -c^2 [\gamma(2\omega_1^2 + \omega_2^2) + i\omega_2^3], & \mathcal{F}^3(q_1, q_2, \bar{q}_2) &= -c^2 [\gamma(\omega_1^2 + 2\omega_2^2) + i\omega_1^3]. \end{aligned}$$

**A.4. Normal form.** To determine the bifurcation structure near a Hopf-Hopf point, we follow the the approach of Kuznetsov [51]. Kuznetsov considers the same ODE (A.17) ([51, Equation (8.88)]) on the generalized center eigenspace  $E^c$  with  $g^j(z(t))$  defined by (A.18), but he expands  $g^j(z)$  as

$$g^j(z) = \sum_{\ell+s+r+k \geq 2} \tilde{g}_{\ell s r k}^j z_1^\ell \bar{z}_1^r z_2^s \bar{z}_2^k. \tag{A.30}$$

Comparing (A.30) with (A.20) we see that we require

$$\tilde{g}_{\ell s r k}^j = \frac{1}{\ell! s! r! k!} g_{\ell s r k}^j. \tag{A.31}$$

Kuznetsov is inconsistent between papers on whether or not he includes the factorial terms in the expansion of  $w(z)$  in his version of (A.21), but that is irrelevant to our exposition in this section, because we only use  $w(z)$  in the previous section to project the center manifold onto the generalized center eigenspace. As such, terms from the expansion of  $w(z)$  appear in  $g_{\ell s r k}^j$ , but these were computed already in the previous section. We then have

LEMMA A.1 (Poincaré Normal Form (Lemma 8.13 in Kuznetsov [51])). *Assume the non-resonance condition*

(HH.0)  $k\omega_1 \neq \ell\omega_2$  for  $k, \ell \in \mathbb{N}_0$  with  $k + \ell \leq 5$ .

*Then there exists a locally defined smooth and smoothly parameter-dependent invertible transformation of the complex variables that for all sufficiently small  $\|\alpha\|$  (where  $\alpha = (\kappa_1 - \kappa_1^*, \kappa_2 - \kappa_2^*)$ ) reduces (A.17) to*

$$\begin{aligned} \dot{w}_1 &= \lambda_1(\alpha) w_1 + G_{2100}^1(\alpha) w_1 |w_1|^2 + G_{1011}^1(\alpha) w_1 |w_2|^2 + G_{3200}^1(\alpha) w_1 |w_1|^4 \\ &\quad + G_{2111}^1(\alpha) w_1 |w_1|^2 |w_2|^2 + G_{1022}^1(\alpha) w_1 |w_2|^4 + \mathcal{O}(\|(w_1, \bar{w}_1, w_2, \bar{w}_2)\|^6), \\ \dot{w}_2 &= \lambda_2(\alpha) w_2 + G_{0021}^2(\alpha) w_2 |w_2|^2 + G_{1110}^2(\alpha) w_2 |w_1|^2 + G_{0032}^2(\alpha) w_2 |w_2|^4 \\ &\quad + G_{1121}^2(\alpha) w_2 |w_1|^2 |w_2|^2 + G_{2210}^2(\alpha) w_2 |w_1|^4 + \mathcal{O}(\|(w_1, \bar{w}_1, w_2, \bar{w}_2)\|^6), \end{aligned} \tag{A.32}$$

where  $w_{1,2} \in \mathbb{C}$  and  $\|(w_1, \bar{w}_1, w_2, \bar{w}_2)\|^2 = |w_1|^2 + |w_2|^2$ . The complex-valued functions  $G_{\ell srk}^{1,2}(\alpha)$  are smooth and, moreover,

$$G_{2100}^1(0) = \tilde{g}_{2100}^1 + \frac{i}{\omega_1} \tilde{g}_{1100}^1 \tilde{g}_{2000}^1 + \frac{i}{\omega_2} (\tilde{g}_{1010}^1 \tilde{g}_{1100}^2 - \tilde{g}_{1001}^1 \tilde{g}_{1100}^2) - \frac{i}{2\omega_1 + \omega_2} \tilde{g}_{0101}^1 \tilde{g}_{0200}^2 \\ - \frac{i}{2\omega_1 - \omega_2} \tilde{g}_{0110}^1 \tilde{g}_{2000}^2 - \frac{i}{\omega_1} |\tilde{g}_{1100}^1|^2 - \frac{2i}{3\omega_1} |\tilde{g}_{0200}^1|^2, \quad (\text{A.33})$$

$$G_{1011}^1(0) = \tilde{g}_{1011}^1 + \frac{i}{\omega_2} (\tilde{g}_{1010}^1 \tilde{g}_{0011}^2 - \tilde{g}_{1001}^1 \tilde{g}_{0011}^2) \\ + \frac{i}{\omega_1} (2\tilde{g}_{2000}^1 \tilde{g}_{0011}^1 - \tilde{g}_{1100}^1 \tilde{g}_{0011}^1 - \tilde{g}_{1010}^1 \tilde{g}_{0011}^1 - \tilde{g}_{0011}^1 \tilde{g}_{0110}^2) - \frac{2i}{\omega_1 + 2\omega_2} \tilde{g}_{0002}^1 \tilde{g}_{0101}^2 \\ - \frac{2i}{\omega_1 - 2\omega_2} \tilde{g}_{0020}^1 \tilde{g}_{1001}^2 - \frac{i}{2\omega_1 - \omega_2} |\tilde{g}_{0110}^1|^2 - \frac{i}{2\omega_1 + \omega_2} |\tilde{g}_{0101}^1|^2, \quad (\text{A.34})$$

$$G_{1110}^2(0) = \tilde{g}_{1110}^2 + \frac{i}{\omega_1} (\tilde{g}_{1100}^1 \tilde{g}_{1010}^2 - \tilde{g}_{0110}^2 \tilde{g}_{1100}^1) \\ + \frac{i}{\omega_2} (2\tilde{g}_{0020}^2 \tilde{g}_{1100}^2 - \tilde{g}_{0011}^2 \tilde{g}_{1100}^2 - \tilde{g}_{1010}^1 \tilde{g}_{1100}^2 - \tilde{g}_{1100}^2 \tilde{g}_{1001}^1) - \frac{2i}{2\omega_1 + \omega_2} \tilde{g}_{0200}^2 \tilde{g}_{0101}^1 \\ + \frac{2i}{2\omega_1 - \omega_2} \tilde{g}_{2000}^2 \tilde{g}_{0110}^1 + \frac{i}{\omega_1 - 2\omega_2} |\tilde{g}_{1001}^2|^2 - \frac{i}{\omega_1 + 2\omega_2} |\tilde{g}_{0101}^2|^2, \quad (\text{A.35})$$

$$G_{0021}^2(0) = \tilde{g}_{0021}^2 + \frac{i}{\omega_2} \tilde{g}_{0011}^1 \tilde{g}_{0020}^2 + \frac{i}{\omega_1} (\tilde{g}_{1010}^1 \tilde{g}_{0011}^2 - \tilde{g}_{0110}^2 \tilde{g}_{0011}^2) - \frac{i}{2\omega_2 + \omega_1} \tilde{g}_{0101}^2 \tilde{g}_{0002}^1 \\ - \frac{i}{2\omega_2 - \omega_1} \tilde{g}_{1001}^2 \tilde{g}_{0020}^1 - \frac{i}{\omega_2} |\tilde{g}_{0011}^2|^2 - \frac{2i}{3\omega_2} |\tilde{g}_{0002}^2|^2, \quad (\text{A.36})$$

where all the  $\tilde{g}_{\ell srk}^j$  are evaluated at  $\alpha = 0$ .

Note that the last two terms in each of the expressions (A.33)–(A.36) are purely imaginary; these terms will vanish when we take real parts later.

We next make a near identity transformation

$$v_1 = w_1 + K_1 w_1 |w_1|^2, \quad v_2 = w_2 + K_2 w_2 |w_2|^2,$$

and introduce a new time  $\tau$  with

$$dt = (1 + e_1 |w_1|^2 + e_2 |w_2|^2) d\tau,$$

where  $K_{1,2}(\alpha)$  and  $e_{1,2}(\alpha)$  are chosen judiciously, to give the following result, where  $\dot{v}_{1,2}$  indicates the derivative with respect to  $\tau$ .

LEMMA A.2 (Lemma 8.14 in Kuznetsov [51]). Assume that

- (HH.1)  $\text{Re } G_{2100}^1(0) \neq 0$  ;
- (HH.2)  $\text{Re } G_{1011}^1(0) \neq 0$  ;
- (HH.3)  $\text{Re } G_{1110}^2(0) \neq 0$  ;
- (HH.4)  $\text{Re } G_{0021}^2(0) \neq 0$  ;

then the system (A.32) is locally smoothly orbitally equivalent to

$$\left. \begin{aligned} \dot{v}_1 &= \lambda_1(\alpha) v_1 + P_{11}(\alpha) v_1 |v_1|^2 + P_{12}(\alpha) v_1 |v_2|^2 + iR_1(\alpha) v_1 |v_1|^4 + S_1(\alpha) v_1 |v_2|^4 \\ &\quad + \mathcal{O}(\|(v_1, \bar{v}_1, v_2, \bar{v}_2)\|^6), \\ \dot{v}_2 &= \lambda_2(\alpha) v_2 + P_{21}(\alpha) v_2 |v_1|^2 + P_{22}(\alpha) v_2 |v_2|^2 + S_2^2(\alpha) v_2 |v_2|^4 + iR_2(\alpha) v_2 |v_2|^4 \\ &\quad + \mathcal{O}(\|(v_1, \bar{v}_1, v_2, \bar{v}_2)\|^6), \end{aligned} \right\} \quad (\text{A.37})$$

where  $v_{1,2}$  are new complex variables,  $P_{jk}(\alpha)$  and  $S_k(\alpha)$  are complex-valued smooth functions, and  $R_k(\alpha)$  are real-valued smooth functions.

From the proof of Lemma A.2 we obtain

$$\begin{aligned} \operatorname{Re} P_{11}(0) &= \operatorname{Re} G_{2100}^1(0), & \operatorname{Re} P_{12}(0) &= \operatorname{Re} G_{1011}^1(0), \\ \operatorname{Re} P_{21}(0) &= \operatorname{Re} G_{1110}^2(0), & \operatorname{Re} P_{22}(0) &= \operatorname{Re} G_{0021}^2(0). \end{aligned} \quad (\text{A.38})$$

This follows because  $P_{11}(\alpha) = \hat{G}_{2100}^1 = G_{2100}^1 + \lambda_1 e_1 + (\lambda_1 + \bar{\lambda}_1)K_1$  and  $\lambda_1(0) = i\omega_1$ , while  $e_1(0) = -\operatorname{Re} G_{3200}^1(0)/\operatorname{Re} G_{2100}^1(0)$ , so

$$P_{11}(0) = G_{2100}^1(0) - i\omega_1 \frac{\operatorname{Re} G_{3200}^1(0)}{\operatorname{Re} G_{2100}^1(0)},$$

which implies that  $\operatorname{Re} P_{11}(0) = \operatorname{Re} G_{2100}^1(0)$ . The other identities in (A.38) follow similarly.

Next we rewrite the system (A.37) in polar coordinates  $(r_1, r_2, \phi_1, \phi_2)$  by letting

$$v_1 = r_1 e^{i\phi_1}, \quad v_2 = r_2 e^{i\phi_2}.$$

Writing  $v_i = x_i + y_i$  and ignoring the higher-order terms for a moment, we have  $r_i^2 = x_i^2 + y_i^2$  and

$$\begin{aligned} r_i \dot{r}_i &= x_i \dot{x}_i + y_i \dot{y}_i = x_i \operatorname{Re} \dot{v}_i + y_i \operatorname{Im} \dot{v}_i \\ &= x_i (\operatorname{Re} (\lambda_i v_i) + \operatorname{Re} (P_{i1} v_i) r_1^2 + \operatorname{Re} (P_{i2} v_i) r_2^2 - R_i y_i r_i^4 + \operatorname{Re} (S_i v_i) r_{3-i}^4) \\ &\quad + y_i (\operatorname{Im} (\lambda_i v_i) + \operatorname{Im} (P_{i1} v_i) r_1^2 + \operatorname{Im} (P_{i2} v_i) r_2^2 + R_i x_i r_i^4 + \operatorname{Im} (S_i v_i) r_{3-i}^4) \\ &= x_i (\mu_i x_i - \omega_i y_i + (\operatorname{Re} (P_{i1}) x_i - \operatorname{Im} (P_{i1}) y_i) r_1^2 + (\operatorname{Re} (P_{i2}) x_i - \operatorname{Im} (P_{i2}) y_i) r_2^2 - R_i y_i r_i^4 \\ &\quad + (\operatorname{Re} (S_i) x_i - \operatorname{Im} (S_i) y_i) r_{3-i}^4) + y_i (\mu_i y_i + \omega_i x_i + (\operatorname{Im} (P_{i1}) x_i + \operatorname{Re} (P_{i1}) y_i) r_1^2 \\ &\quad + (\operatorname{Im} (P_{i2}) x_i + \operatorname{Re} (P_{i2}) y_i) r_2^2 + R_i x_i r_i^4 + (\operatorname{Im} (S_i) x_i + \operatorname{Re} (S_i) y_i) r_{3-i}^4) \\ &= \mu_i (x_i^2 + y_i^2) + \operatorname{Re} (P_{i1}) (x_i^2 + y_i^2) r_1^2 + \operatorname{Re} (P_{i2}) (x_i^2 + y_i^2) r_2^2 + \operatorname{Re} (S_i) (x_i^2 + y_i^2) r_{3-i}^4 \\ &= \mu_i r_i^2 + \operatorname{Re} (P_{i1}) r_i^2 r_1^2 + \operatorname{Re} (P_{i2}) r_i^2 r_2^2 + \operatorname{Re} (S_i) r_i^2 r_{3-i}^4, \end{aligned}$$

where  $3-i=1$  when  $i=2$  and  $3-i=2$  when  $i=1$ , and so denotes the other index.

Then (A.37) can be written as

$$\begin{aligned} \dot{r}_1 &= r_1 (\mu_1(\alpha) + p_{11}(\alpha) r_1^2 + p_{12}(\alpha) r_2^2 + s_1(\alpha) r_2^4) + \Phi_1(r_1, r_2, \phi_1, \phi_2, \alpha), \\ \dot{r}_2 &= r_2 (\mu_2(\alpha) + p_{21}(\alpha) r_1^2 + p_{22}(\alpha) r_2^2 + s_2(\alpha) r_1^4) + \Phi_2(r_1, r_2, \phi_1, \phi_2, \alpha), \\ \dot{\phi}_1 &= \omega_1(\alpha) + \Psi_1(r_1, r_2, \phi_1, \phi_2, \alpha), \\ \dot{\phi}_2 &= \omega_2(\alpha) + \Psi_2(r_1, r_2, \phi_1, \phi_2, \alpha), \end{aligned} \quad (\text{A.39})$$

where

$$p_{jk} = \operatorname{Re} P_{jk}, \quad s_j = \operatorname{Re} S_j, \quad j, k = 1, 2. \quad (\text{A.40})$$

If the map  $(\kappa_1, \kappa_2) \mapsto (\mu_1(\kappa_1, \kappa_2), \mu_2(\kappa_1, \kappa_2))$  is regular at  $(\kappa_1^*, \kappa_2^*)$  or, equivalently, the map  $\alpha \mapsto (\mu_1(\alpha), \mu_2(\alpha))$  is regular at  $\alpha = 0$ , that is,  $\det \left( \frac{\partial(\mu_1, \mu_2)}{\partial(\alpha_1, \alpha_2)} \right) \Big|_{\alpha=0} \neq 0$ , then one can use  $(\mu_1, \mu_2)$  to parameterize a small neighbourhood of  $(\kappa_1^*, \kappa_2^*)$  in the parameter plane and, hence, regard the

functions of  $\alpha$  in the theory above as functions of  $(\mu_1, \mu_2)$ , which are the real parts of the eigenvalues, which vanish at the Hopf-Hopf bifurcation. This condition is easy to verify since

$$\left. \frac{\partial \mu_i}{\partial \kappa_j} \right|_{\alpha=0} = \operatorname{Re} \left( \left. \frac{\partial \lambda}{\partial \kappa_j} \right|_{\lambda=i\omega_i} \right), \quad \text{and} \quad \frac{\partial \lambda}{\partial \kappa_j} = \frac{-e^{-a_j \lambda}}{1 - a_j \kappa_j e^{-a_j \lambda} - a_{3-j} \kappa_{3-j} e^{-a_{3-j} \lambda}}, \quad (\text{A.41})$$

where the last expression follows from differentiating (1.12). We obtain the following theorem, adapted from Theorem 8.8 in Kuznetsov [51].

**THEOREM A.3.** *Consider the constant delay DDE (A.1), where the linear operator  $\mathcal{L}u_t$  is defined by (A.2) and nonlinear operator  $\mathcal{F}(u_t)$  is given by (A.4), with parameters  $(\kappa_1, \kappa_2)$  which has eigenvalues*

$$\lambda_j(\kappa_1, \kappa_2) = \mu_j(\kappa_1, \kappa_2) \pm i\omega_j(\kappa_1, \kappa_2), \quad j = 1, 2$$

with

$$\mu_j(\kappa_1^*, \kappa_2^*) = 0, \quad \omega_j(\kappa_1^*, \kappa_2^*) = \omega_j, \quad j = 1, 2.$$

If the nondegeneracy conditions

(HH.0)  $k\omega_1 \neq \ell\omega_2$  for  $k, \ell \in \mathbb{N}_0$  with  $k + \ell \leq 5$ ,

(HH.1)  $p_{11}(\kappa_1^*, \kappa_2^*) = \operatorname{Re} G_{2100}^1(0) \neq 0$ ;

(HH.2)  $p_{12}(\kappa_1^*, \kappa_2^*) = \operatorname{Re} G_{1011}^1(0) \neq 0$ ;

(HH.3)  $p_{21}(\kappa_1^*, \kappa_2^*) = \operatorname{Re} G_{1110}^2(0) \neq 0$ ;

(HH.4)  $p_{22}(\kappa_1^*, \kappa_2^*) = \operatorname{Re} G_{0021}^2(0) \neq 0$ ;

hold, where the  $G_{\ell srk}^{1,2}(0)$  are defined by (A.33)-(A.36), and

(HH.5) the map  $(\kappa_1, \kappa_2) \mapsto (\mu_1(\kappa_1, \kappa_2), \mu_2(\kappa_1, \kappa_2))$  is regular at  $(\kappa_1^*, \kappa_2^*)$ , then the system is locally orbitally equivalent near the origin to

$$\left. \begin{aligned} \dot{r}_1 &= r_1(\mu_1 + p_{11}(\mu)r_1^2 + p_{12}(\mu)r_2^2 + s_1(\mu)r_2^4) + \mathcal{O}((r_1^2 + r_2^2)^3), \\ \dot{r}_2 &= r_2(\mu_2 + p_{21}(\mu)r_1^2 + p_{22}(\mu)r_2^2 + s_2(\mu)r_1^4) + \mathcal{O}((r_1^2 + r_2^2)^3), \\ \dot{\phi}_1 &= \omega_1(\mu) + \Psi_1(r_1, r_2, \phi_1, \phi_2, \mu), \\ \dot{\phi}_2 &= \omega_2(\mu) + \Psi_2(r_1, r_2, \phi_1, \phi_2, \mu), \end{aligned} \right\} \quad (\text{A.42})$$

where  $\Psi_j(0, 0, \phi_1, \phi_2, \mu) = 0$ .

We remark that Kuznetsov [51] also gives a formula for the  $s_j(0)$ , but we will not need this and, anyway, it requires terms  $G_{\ell srk}^{1,2}(0)$  that he does not state.

**A.5. Determining the normal form bifurcation diagram.** To determine the dynamics and bifurcation near a Hopf-Hopf point we will apply Theorem A.3 to the constant delay DDE (2.14), which was written as an RFDE of the form (A.1). We do not need to consider the angle equations for  $\varphi_{1,2}$  from (A.42) because  $\omega_{1,2}(0) > 0$  and  $\Psi_{1,2}(0, 0, \phi_1, \phi_2, \mu) = 0$ , so close to a Hopf-Hopf bifurcation these equations just describe rotations. Nearly nobody also computes the functions  $p_{ij}(\mu)$  appearing in Theorem A.3. To determine the qualitative bifurcation diagram it is sufficient to consider the truncated amplitude system

$$\begin{aligned} \dot{r}_1 &= r_1(\mu_1 + p_{11}r_1^2 + p_{12}r_2^2 + s_1r_2^4), \\ \dot{r}_2 &= r_2(\mu_2 + p_{21}r_1^2 + p_{22}r_2^2 + s_2r_1^4). \end{aligned} \quad (\text{A.43})$$

Here  $p_{ij}$  and  $s_i$  are formally functions of  $\mu$ , but it is sufficient to calculate  $p_{ij}(0)$  and  $s_i(0)$  to determine the bifurcation diagram. We only need to consider positive amplitudes and, following

Kuznetsov [51], we let  $\rho_j = r_j^2 \geq 0$  and rewrite the amplitude equations (A.43) as

$$\begin{aligned}\dot{\rho}_1 &= 2\rho_1(\mu_1 + p_{11}\rho_1 + p_{12}\rho_2 + s_1\rho_2^2), \\ \dot{\rho}_2 &= 2\rho_2(\mu_2 + p_{21}\rho_1 + p_{22}\rho_2 + s_2\rho_1^2).\end{aligned}\tag{A.44}$$

Notice that an equilibrium of these equations with  $\rho_1 = \rho_2 = 0$  corresponds to the trivial steady state of (2.14). An equilibrium of the amplitude equations with exactly one of  $\rho_i$  non-zero corresponds to a periodic orbit of (2.14) (because of rotation from the angle equations), while an equilibrium of the amplitude equations with both  $\rho_i$  non-zero corresponds to a two-dimensional torus for (2.14). A periodic orbit of (A.44) corresponds to a three-dimensional torus for (A.42) and (2.14).

There are several possible cases, but we focus on the case where  $p_{11} < 0$  and  $p_{22} < 0$ , since it arises at  $HH_j$  for  $j = 1, 2$  and  $3$ . We make the change of coordinates

$$\xi_1 = -p_{11}\rho_1, \quad \xi_2 = -p_{22}\rho_2, \quad \tau = 2t\tag{A.45}$$

in (A.44), yielding

$$\begin{aligned}\xi_1' &= \xi_1(\mu_1 - \xi_1 - \vartheta\xi_2 + \Theta\xi_2^2), \\ \xi_2' &= \xi_2(\mu_2 - \xi_2 - \delta\xi_1 + \Delta\xi_1^2),\end{aligned}\tag{A.46}$$

where

$$\vartheta = \frac{p_{12}}{p_{22}}, \quad \delta = \frac{p_{21}}{p_{11}}, \quad \Theta = \frac{s_1}{p_{22}^2}, \quad \Delta = \frac{s_2}{p_{11}^2}.$$

Recalling that  $\rho_i \geq 0$ , with  $p_{11} < 0$  and  $p_{22} < 0$  the minus signs are incorporated into the change of coordinates (A.45) so that only solutions of (A.46) with  $\xi_i \geq 0$  for each  $i$  correspond to solutions of (A.43).

Kuznetsov [51] only analyses the case  $\vartheta \geq \delta$  and suggests to make a change of coordinates otherwise, but actually it is easy to deal directly with all the cases where  $\vartheta \neq \delta$ .

Equation (A.46) has a steady state at  $(\xi_1, \xi_2) = (0, 0)$  for all values of the parameters, corresponding to the steady state of (A.42) and (2.14). For  $\mu_1 > 0$  there is another steady state of (A.46) with  $(\xi_1, \xi_2) = (\mu_1, 0)$ . This corresponds to a periodic orbit for (A.42) that bifurcates from the steady state along the Hopf bifurcation curve

$$H_1 = \{(\mu_1, \mu_2) : \mu_1 = 0\}.$$

Similarly, for  $\mu_2 > 0$  there is a third steady state of (A.46) with  $(\xi_1, \xi_2) = (0, \mu_2)$  corresponding to another periodic orbit for (A.42) that bifurcates from the steady state along the Hopf bifurcation curve

$$H_2 = \{(\mu_1, \mu_2) : \mu_2 = 0\}.$$

Finally, let us look for the torus and torus bifurcations. We seek a steady state of (A.46) not on the coordinate axes, so we require

$$0 = \mu_1 - \xi_1 - \vartheta\xi_2 + \Theta\xi_2^2 = \mu_2 - \xi_2 - \delta\xi_1 + \Delta\xi_1^2.\tag{A.47}$$

Applying the implicit function theorem, we can find a function  $(\xi_1, \xi_2) = g(\mu_1, \mu_2)$  such that  $(\mu_1, \mu_2, \xi_1, \xi_2)$  satisfy (A.47) provided the appropriate Jacobian matrix is nonzero, for which we require  $\vartheta\delta - 1 \neq 0$  or, equivalently,

$$(HH.6) \quad \det \begin{pmatrix} p_{11}(0) & p_{12}(0) \\ p_{21}(0) & p_{22}(0) \end{pmatrix} \neq 0.$$

Then the implicit function theorem gives a steady-state solution of (A.46) with

$$\xi_1 = \frac{\vartheta\mu_2 - \mu_1}{\vartheta\delta - 1} + \mathcal{O}(\mu_1^2 + \mu_2^2), \quad \xi_2 = \frac{\delta\mu_1 - \mu_2}{\vartheta\delta - 1} + \mathcal{O}(\mu_1^2 + \mu_2^2). \quad (\text{A.48})$$

(This can also be seen by letting  $\Theta = \Delta = 0$  in (A.46) and solving directly for  $\xi_{1,2}$ .) Recall that we need  $\xi_{1,2} > 0$  for the solution (A.48) to correspond to a torus of (A.42) and (2.14). If  $\delta\vartheta - 1 < 0$  we then require

$$\delta\mu_1 < \mu_2, \quad \vartheta\mu_2 < \mu_1 \quad (\text{A.49})$$

to satisfy this condition close to the bifurcation point; or with the inequalities reversed, if  $\delta\vartheta - 1 > 0$ . This defines the torus bifurcation curves  $T_1$  and  $T_2$  which both start at  $(\mu_1, \mu_2) = (0, 0)$ . To leading order, these satisfy one strict inequality in (A.49) with equality in the other expression; and the torus exists in the cone for which both equalities hold.

If  $\vartheta > 0 > \delta$  we obtain

$$T_1 = \{(\mu_1, \mu_2) : \mu_2 = \delta\mu_1 + \mathcal{O}(\mu_1^2), \mu_1 > 0\}, \quad (\text{A.50})$$

$$T_2 = \{(\mu_1, \mu_2) : \mu_1 = \vartheta\mu_2 + \mathcal{O}(\mu_2^2), \mu_2 > 0\}, \quad (\text{A.51})$$

with the torus existing between them with  $\mu_1 > 0$ . Notice that, as  $(\mu_1, \mu_2) \rightarrow T_1$ , we have  $(\xi_1, \xi_2) \rightarrow (\mu_1, 0)$ , which is the fixed point corresponding to the periodic orbit created in the  $H_1$  Hopf bifurcation. Similarly, as  $(\mu_1, \mu_2) \rightarrow T_2$ , we have  $(\xi_1, \xi_2) \rightarrow (0, \mu_2)$ . Kuznetsov identifies this as Case III of five cases depending on the signs of  $\vartheta$ ,  $\delta$  and  $\delta\vartheta - 1$ , which result in topologically different bifurcation diagrams.

Once the normal form is calculated it is actually straightforward to transform back to the original parameters  $(\kappa_1, \kappa_2)$ . The linear part of the mapping  $(\kappa_1, \kappa_2) \mapsto (\mu_1(\kappa_1, \kappa_2), \mu_2(\kappa_1, \kappa_2))$  is defined by

$$\begin{pmatrix} \mu_1 \\ \mu_2 \end{pmatrix} = \begin{pmatrix} \text{Re } \lambda_1 \\ \text{Re } \lambda_2 \end{pmatrix} = \begin{pmatrix} \text{Re} \left( \frac{\partial \lambda}{\partial \kappa_1} \right) \Big|_{\lambda=i\omega_1} & \text{Re} \left( \frac{\partial \lambda}{\partial \kappa_2} \right) \Big|_{\lambda=i\omega_1} \\ \text{Re} \left( \frac{\partial \lambda}{\partial \kappa_1} \right) \Big|_{\lambda=i\omega_2} & \text{Re} \left( \frac{\partial \lambda}{\partial \kappa_2} \right) \Big|_{\lambda=i\omega_2} \end{pmatrix} \begin{pmatrix} \kappa_1 - \kappa_1^* \\ \kappa_2 - \kappa_2^* \end{pmatrix} = J \begin{pmatrix} \kappa_1 - \kappa_1^* \\ \kappa_2 - \kappa_2^* \end{pmatrix},$$

where the entries in the Jacobian matrix  $J$  are calculated from (A.41). By (HH.5) the Jacobian is invertible and, hence, to leading order

$$\begin{pmatrix} \kappa_1 \\ \kappa_2 \end{pmatrix} = \begin{pmatrix} \kappa_1^* \\ \kappa_2^* \end{pmatrix} + J^{-1} \begin{pmatrix} \mu_1 \\ \mu_2 \end{pmatrix}. \quad (\text{A.52})$$

The calculation of the normal form coefficients for the state-dependent DDE (1.3) is implemented in the accompanying Matlab [63] code `HHnfDDE`. This code first uses symbolic differentiation to compute the constant delay expansion of the DDE described Sec. 2.1. The exact locations of the Hopf-Hopf points are computed, as described in Sec. 2.2, with the auxiliary routine `findHH`. Finally, the coefficients of the Hopf-Hopf normal form are computed as described in Appendix A. At any of the points  $HH_1$ ,  $HH_2$  and  $HH_3$ , the code `HHnfDDE` identifies the Hopf-Hopf bifurcation and computes its respective normal form in about 3.7 seconds on a Lenovo Thinkpad X230.

The results of these calculations are summarized in Tables 1 and 2.

Although applied only to the state-dependent DDE (1.3) here, the code `HHnfDDE` is nevertheless general purpose. To compute Hopf-Hopf normal forms for a different state-dependent DDE it would be necessary only to:

1. change the definition of the nonlinearity and the characteristic function,
2. supply approximate Hopf-Hopf points, and
3. compute the basis for the adjoint problem (which amounts to computing an integral that depends on the linear operator of the problem).